New Jersey Institute of Technology
Digital Commons @ NJIT

Dissertations | Electronic Theses and Dissertations

Fall 1-31-2013

Modeling cell proliferation in a perfusion tissue engineering bioreactor

Jeffrey Vincent Pohlmeyer
New Jersey Institute of Technology

Follow this and additional works at: https://digitalcommons.njit.edu/dissertations

 Part of the Mathematics Commons

Recommended Citation

Pohlmeyer, Jeffrey Vincent, "Modeling cell proliferation in a perfusion tissue engineering bioreactor" (2013). *Dissertations*. 351.
https://digitalcommons.njit.edu/dissertations/351

This Dissertation is brought to you for free and open access by the Electronic Theses and Dissertations at Digital Commons @ NJIT. It has been accepted for inclusion in Dissertations by an authorized administrator of Digital Commons @ NJIT. For more information, please contact digitalcommons@njit.edu.

Copyright Warning & Restrictions

The copyright law of the United States (Title 17, United States Code) governs the making of photocopies or other reproductions of copyrighted material.

Under certain conditions specified in the law, libraries and archives are authorized to furnish a photocopy or other reproduction. One of these specified conditions is that the photocopy or reproduction is not to be "used for any purpose other than private study, scholarship, or research." If a, user makes a request for, or later uses, a photocopy or reproduction for purposes in excess of "fair use" that user may be liable for copyright infringement,

This institution reserves the right to refuse to accept a copying order if, in its judgment, fulfillment of the order would involve violation of copyright law.

Please Note: The author retains the copyright while the New Jersey Institute of Technology reserves the right to distribute this thesis or dissertation

Printing note: If you do not wish to print this page, then select "Pages from: first page # to: last page #" on the print dialog screen

NJIT New Jersey's Science & Technology University

The Van Houten library has removed some of the personal information and all signatures from the approval page and biographical sketches of theses and dissertations in order to protect the identity of NJIT graduates and faculty.

ABSTRACT

MODELING CELL PROLIFERATION IN A PERFUSION TISSUE ENGINEERING BIOREACTOR

by
Jeffrey Vincent Pohlmeyer

In this dissertation we develop a comprehensive model to simulate a tissue engineering experiment. The experiment takes place in a bioreactor in which a cell seeded porous scaffold is placed, and the scaffold experiences a perfused flow of a nutrient-rich culture medium. The goal of the model is to assist experimentalists in evaluation of different parameter scenarios as the time needed to simulate an experiment is significantly less than the time needed for the experiment itself. We provide the full two-dimensional model development, as well as investigation into possible variations of specific model choices, and we demonstrate the robustness and versatility of the model.

Simulation results are presented with different initial cell seeding scenarios which increase in complexity with each simulation. We next model the effect of printing a growth factor onto the scaffold in an attempt to direct cell motility and enhance proliferation via a process known as haptotaxis. While a quantitative representation of these phenomena requires more experimental data than are yet available, qualitative agreement with preliminary experimental studies is obtained, and appears promising. The ultimate goal of such modeling is to ascertain initial conditions (growth factor distribution, initial cell seeding, etc.) that will lead to a final desired outcome.

A simplified 2D mathematical model for tissue growth within a cyclically-loaded tissue engineering scaffold is then analyzed. Such cyclic loading has the potential to improve yield and functionality of tissue such as bone and cartilage when grown on a scaffold within a perfusion bioreactor. The cyclic compression affects the flow of the perfused nutrient, leading to flow properties that are inherently unsteady,

though periodic, on a timescale short compared with that of tissue proliferation. A two-timescale analysis based on these two well-separated timescales is exploited to derive a closed model for the tissue growth on the long timescale. Some sample numerical results are given for the final model, and the comparison with the unloaded case is discussed.

Finally, we simulate to hypothetical extensions to the basic model. We first test the hypothesis of a death rate which varies as a function of the local fluid flow and compare the results to the original model. The second test is the introduction of a channel through the center of the porous scaffold thought to aid in nutrient delivery to the cells in the interior of the scaffold. The last two simulations are presented to illustrate the ability that the model has to incorporate many different supplemental experimental situations, whether they have yet been experimentally considered or not.

MODELING CELL PROLIFERATION IN A PERFUSION TISSUE ENGINEERING BIOREACTOR

by
Jeffrey Vincent Pohlmeyer

A Dissertation
Submitted to the Faculty of
New Jersey Institute of Technology and
Rutgers, The State University of New Jersey – Newark
in Partial Fulfillment of the Requirements for the Degree of
Doctor of Philosophy in Mathematical Sciences

Department of Mathematical Sciences
Department of Mathematics and Computer Science, Rutgers-Newark

January 2013

Copyright © 2013 by Jeffrey Vincent Pohlmeyer
ALL RIGHTS RESERVED

APPROVAL PAGE

MODELING CELL PROLIFERATION IN A PERFUSION TISSUE ENGINEERING BIOREACTOR

Jeffrey Vincent Pohlmeyer

Linda J. Cummings, PhD, Dissertation Advisor — Date
Associate Professor, Department of Mathematical Sciences, NJIT

Lou Kondic, PhD, Committee Member — Date
Professor, Department of Mathematical Sciences, NJIT

Michael S. Siegel, PhD, Committee Member — Date
Professor, Department of Mathematical Sciences, NJIT

Shahriar Afkhami, PhD, Committee Member — Date
Assistant Professor, Department of Mathematical Sciences, NJIT

Treena L. Arinzeh, PhD, Committee Member — Date
Professor, Department of Biomedical Engineering, NJIT

BIOGRAPHICAL SKETCH

Author: Jeffrey Vincent Pohlmeyer

Degree: Doctor of Philosophy

Date: January 2013

Undergraduate and Graduate Education:

- Doctor of Philosophy in Mathematical Sciences
  New Jersey Institute of Technology, Newark, NJ, 2013
- Master of Science in Pure and Applied Mathematics
  Montclair State University, Montclair, NJ, 2008
- Bachelor of Science in Mathematics and French
  Loyola College in Maryland, Baltimore, MD, 2004

Major: Mathematical Sciences

Presentations and Publications:

J.V. Pohlmeyer, S.L. Waters, L.J. Cummings, "Mathematical model of growth factor driven haptotaxis and proliferation in a tissue engineering scaffold," *Bulletin of Mathematical Biology, Submitted*

J.V. Pohlmeyer, L.J. Cummings, "Cyclic loading of growing tissue in a bioreactor: Mathematical model and asymptotic analysis," *In preparation*

J. Pohlmeyer, S. Waters, L. Cummings, "Mathematical model of growth factor driven haptotaxis and proliferation in a tissue engineering scaffold," *Poster Presentation*, GSA Graduate Student Research Day, NJIT, October, 2012.

J. Pohlmeyer, S. Waters, L. Cummings, "Mathematical model of growth factor driven haptotaxis and proliferation in a tissue engineering scaffold," *Contributed Talk*, Frontiers in Applied and Computational Mathematics, NJIT, May, 2012.

J. Pohlmeyer, S. Waters, L. Cummings, "The Role of Haptotaxis in Tissue Engineering," *Poster Presentation*, 5th Oxford University SIAM Student Chapter Conference, Oxford University, January, 2012.

For my wife, who has been by my side supporting, pushing, and dealing with me while I embarked on the arduous task that is a PhD.

For my father, who has never stopped believing in me, even when I didn't believe in myself.

ACKNOWLEDGMENT

I would like to express my deepest gratitude to my advisor, Linda J. Cummings, for everything she has done for me for the last few years. Her endless patience with me when I would have a week in which I didn't get much work done, when I have had stupid moments and asked questions to which an undergrad would know the answers, and the countless times when I wanted to assume my computer code was not wrong, but instead the method of solving our problem was wrong. She has always been available to talk about my future plans, and she is the only reason I was able to study at one of the most prestigious universities in the world. It is for these reasons and countless others that I owe her my endless thanks.

I would also like to thank my committee members, Professor Shahriar Afkhami, Professor Treena Arinzeh, Professor Lou Kondic, and Professor Michael Siegel for their time taken to participate on my committee, but also for helping me with the many questions I've brought to them in working on my dissertation.

I want to thank all of those who have taught me in my classes at NJIT, especially Professor Michael Booty, Professor Yassine Boubendir, Professor David Horntrop, Professor Jonathan Luke, Professor Robert Miura, and Professor Richard Moore.

I owe a great debt of gratitude to the mathematics department as a whole, including Professor Daljit Ahluwalia and Professor Jonathan Luke who have been very open to suggestion and questions and very helpful as chairmen of the department. I would also like to thank Eileen Michie and Padma Gulati for being extraordinarily understanding when I had departmental difficulties and for making my life in the department infinitely easier than it could have been.

I would like to express my thanks to Dr. Sarah Waters for being a friendly face while I was in the United Kingdom and a helpful co-advisor for my time across the pond and OCCAM for hosting me for a very productive month and a half in

early 2012. To that end, portions of this dissertation were supported by Award No. KUK-C1-013-04 made by King Abdullah University of Science and Technology (KAUST).

Thanks go to my fellow graduate students who I have come to know over the last four and a half years in the department. Especially thanks to Nattapol Aunsri, Daniel Cargill, Matt Causley, Daniel Fong, Zhi Liang, Te-Sheng Lin, Tao Lin, Manman Ma, Kyle Mahady, Matt Malej, Dawid Midura, Herve Nganguia, Aminur Rahman, Ivana Seric, Oleksiy Varfolomiyev, and Jacek Wrobel for many productive discussions and spirited debates.

Finally, special thanks go to my family: my wife Katie, my parents Philip, Jane, Lynda, and Mario, my brother Chris, my sister Allyson, brother-in-law Frank, and nephew Zach. My cousins and significant others Karen, Susie, Laurie, Alan, Nicole, Pat, Mitch, Alyssa, and Colin, Aunt Mary, Ann, Rocky, Uncle Al, and Lisa, my grandparents Phyllis and Ray, my mother-in-law Nancy, sister-in-law Kim, grandmother-in-law Maryann, and last but certainly not least my great friends Jeff, Sarah, Zoë, and Abigail. You have all tolerated me for the past four and a half years and not once did anyone ask me why I'm wasting my time going to school for so much longer. Nor did anyone ask why I hadn't graduated yet and everyone has always at least feigned an interest in what I do.

TABLE OF CONTENTS

TABLE OF CONTENTS
(Continued)

Chapter **Page**

TABLE OF CONTENTS
(Continued)

Chapter **Page**

TABLE OF CONTENTS
(Continued)

Chapter **Page**

LIST OF TABLES

LIST OF FIGURES

LIST OF FIGURES
(Continued)

Figure **Page**

LIST OF FIGURES
(Continued)

Figure **Page**

LIST OF FIGURES
(Continued)

Figure **Page**

LIST OF FIGURES
(Continued)

Figure **Page**

LIST OF FIGURES
(Continued)

Figure **Page**

LIST OF FIGURES
(Continued)

Figure **Page**

LIST OF FIGURES
(Continued)

Figure **Page**

LIST OF FIGURES
(Continued)

Figure **Page**

CHAPTER 1

INTRODUCTION

Tissue engineering is a relatively young field, yet one whose importance cannot be overstated. There is a shortage of available organs for those in need of transplants [13], and the situation will worsen as the world's population continues to increase and age. Many different tissue engineering protocols have been and continue to be researched to determine if it is possible to grow tissue to implant into a patient. One methodology that receives significant attention [15–17] involves harvesting an individual's own cells, growing the specific type of tissue needed outside the body, and then re-implanting when the tissue is viable. This method of *in vitro* tissue engineering using the patient's own tissue greatly reduces the risk of tissue rejection. Conducting a large suite of experiments in which tissue is grown within the laboratory undoubtedly provides the best indicator of likely success; however, the time taken for tissue to grow, the "trial and error" nature of optimizing the outcome, and the costly possibility of human or mechanical error in running the experiments makes this approach inefficient for testing purposes. Mathematically modeling the growing tissue can be a useful way to augment such experimental programs as case studies can be simulated in only a fraction of the time that it takes actual tissue to grow and, once calibrated against experiments, models can be used to make predictions of optimal conditions for successful tissue growth.

A commonly-used tissue engineering protocol is to place a porous scaffold that has been seeded with cells into a bioreactor filled with a nutrient-rich culture medium. Scaffolds can have widely-varying properties, such as differing pore sizes and pore architectures, but they all serve the purpose of providing an apparatus on which cells can attach and proliferate over time. One of the many possible types of architectures

which can be used for the scaffold is seen in Figure 1.1. The scaffold plus cells are

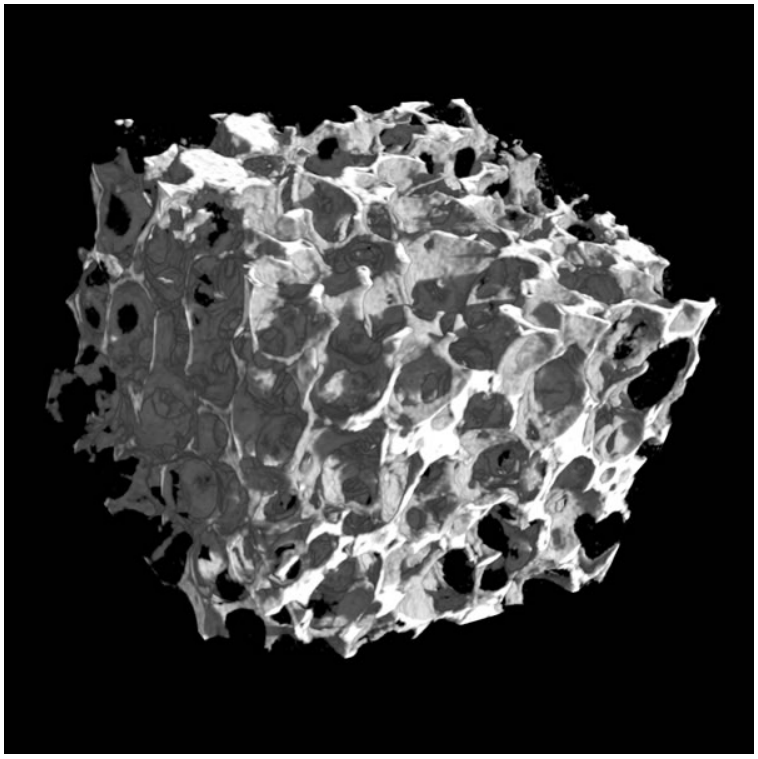

Figure 1.1 An example of a scaffold.

collectively referred to as a tissue engineering construct. Early mathematical models of tissue engineering saw the nutrient within the culture medium delivered to the cell-seeded scaffold via diffusion alone. Malda *et al.* [26] measured (via experiments and modeling) the development of oxygen gradients in chondrogenesis due to oxygen consumption by the cells. The goal was to predict oxygen levels within the construct to obtain an understanding of the relationship between local oxygen concentration and the oxygen demand by the cells. In an extension of this work, Lewis *et al.* [23] analyzed the relationship between nutrient concentration and cell density in one spatial dimension, while assuming no cellular movement within the scaffold. They compared their model to experimental results, and showed that with proliferation, a diffusion dominated model will see growth in the outer region of the scaffold where

oxygen concentrations are highest, but less proliferation near the scaffold center where the limitations of diffusive transport means oxygen levels are low.

One way in which nutrient may be better provided to the entire scaffold is via perfusion; that is, forced flow of nutrient-rich culture medium through the seeded scaffold. As well as the enhanced nutrient delivery due to advection, the forced flow generates fluid shear stress within the scaffold, which can stimulate enhanced cell proliferation. Certain cell types (e.g., osteoblasts) undergo enhanced proliferation when exposed to shear stress [20, 48](this is an example of *mechanotransduction*, in which mechanical stimulus triggers a cellular response). Raimondi *et al.* [43] experimentally compared a static culture system, a surface perfused culture system (where nutrient-rich culture medium is driven only along surfaces of the scaffold), and a culture system in which nutrient-rich culture medium is forced through the whole construct. They found that there is a two-fold improvement in cell viability from forced perfusion when compared to the other methods of nutrient delivery. They were also able to obtain details of the microarchitecture of the pores within the scaffold via light microscopy, and developed a computational fluid dynamics model to examine the modulating effect of fluid shear stress on growth. Porter *et al.* [41] attempted to more accurately calculate the fluid stress in three dimensions by constructing pore microarchitecture using microcomputed tomography and using the Lattice-Boltzmann method to simulate fluid flow within the structure. They found that shear stress levels leading to increased cell proliferation were lower than previously determined by Raimondi *et al.* [43].

These early studies tended to focus on isolated aspects of the problem. While these analyses are very useful in improving knowledge about specific aspects of tissue growth, more recent models have moved closer to the goal of describing a tissue engineering construct in its entirety. A typical method for modeling full systems involves examining the different constituent parts as separate domains, or phases. For

example, a two-phase model might consider the cell population as one phase and the nutrient-rich culture medium as another phase, and model the interactions between the two on a macroscopic level. Furthermore, there are many ways that the phases can be modeled. A simple example of this is how cell population can be considered via direct cell density or a change in scaffold permeability. Coletti *et al.* [10] considered changes in both scaffold properties (due to cell proliferation) and nutrient transport (via fluid flow) in a three-dimensional perfusion bioreactor in their multi-phase model. In this model, the flow external to the scaffold was governed by the Navier-Stokes equations, coupled with the Brinkman equations within the porous scaffold. Oxygen uptake was modeled by Michaelis-Menton kinetics, and cell growth as a function of nutrient concentration by the Contois equation [11]. Shakeel *et al.* [46] examined the effects of initial cell seeding density and scaffold pore structure on the resulting structure of the engineered tissue construct. Chung *et al.* [8], developed a three-layer model of cell proliferation, nutrient uptake, and culture medium circulation within a porous scaffold under perfusion, the scaffold itself being held between two fluid layers. In subsequent work, Chung *et al.* [9] modeled only the scaffold layer, neglecting the two fluid layers, and were able to obtain the same results when compared to their earlier work.

While the above models all deal with multiple phases, the cell phase was not explicitly modeled. Instead, cells were considered as nutrient sinks and proliferation was modeled as a change of scaffold permeability and porosity. In explicitly considering a cell phase, O'Dea *et al.* [34] were able to incorporate mechanotransductive effects, in particular considering the mechanical response of an imposed flow on the cell phase and predicting the resulting cell distribution. This work was expanded in [35] to take explicit account of the scaffold and its interactions with the growing cells. The authors derived a simplified model based on an assumption of

slender bioreactor geometry (i.e. a long wavelength analysis), while in a related work Osborne *et al.* [37] considered a finite element solution of the full system.

A specific mechanotransductive effect that has been investigated is that of a cartilage or bone bioreactor within which the construct undergoes cyclic compression. The rationale behind such mechanical loading is that it mimics the experience of cartilage or bone within a joint *in vivo* and should thus provide an ideal environment. As cartilage is a relatively avascular tissue it poses a unique challenge to tissue engineers because without a defined vasculature delivery of nutrient to the entire scaffold is much more difficult. To deal with this difficulty, significant experimental and modeling work has been carried out over the last two decades to attempt to determine the best way to engineer cartilage. The cyclic loading appears to affect a very wide range of experimental outcomes, in ways that are not yet fully understood. For example, Mauck *et al.* [27] discovered that different types of scaffolds with differing stiffness and modulus can greatly affect the end result of an experiment. The details of the "loading protocol" can also demonstrably affect experimental outcomes. For example, Schätti *et al.* [44] compared different types of loading and found that only samples which had both shear and strain stresses applied showed a significant up-regulation of chondrogenic genetic markers. Buschmann *et al.* [4] observed that chondrocytes responded biosynthetically to static and dynamic loading in a manner similar to that of intact organ culture. They saw a response to compression more pronounced at later times in the experiments, and concluded that application of a mechanical load may significantly alter the long-term development of the tissue.

Modeling and simulation of loading on the tissue engineering construct can provide significant insight into the effects that stress and/or strain plays in chondrocyte proliferation. For example, Babalola and Bonassar [2] simulated results using a 2D finite element method to determine which types of scaffolds work best in cartilage tissue growth; while Moo *et al.* [30] used a multi-scale model (accounting for

chondrocytes and cartilage tissue) to examine the effect of impact loading on cell death in an attempt to determine the cause of higher cell death at higher strain. Other aspects of chondrocyte growth have been modeled. Catt *et al.* [7] examined the effects of extra-cellular matrix (ECM) production on chondrocyte growth and compared their results to experimental data. They noted that cellular differentiation rates played a more significant role than did nutrient transport on chondrocyte levels. Lutianov *et al.* [24] developed a model which indicated that a combination of chondrocytes and stem cells (which can differentiate into chondrocytes) produces the best results when compared to seeding with strictly stem cells or chondrocytes. As there are many different aspects which can be and have been modeled, Sengers *et al.* [45] compiled a review of the multitude of mathematical models used in tissue engineering, and the reader is directed there for a more comprehensive list.

A challenge still facing tissue engineers is how to initially seed the porous scaffold with the appropriate distribution of cells to obtain a desired end result. Even if the appropriate initial seeding distribution is known, it is not always possible to achieve this in the laboratory. One way around this difficulty is to exploit haptotaxis, in which cells move up gradients of a chemical that is bound to the scaffold. Significant research has investigated the effects of scaffold surface modification, particularly as it relates to cell adhesion. For example, Zelzer *et al.* [49] examined how adhesion protein adsorption combined with plasma polymerised surfaces affect cell adhesion (this paper also contains a useful overview of selected earlier work on scaffold surface modification). As an alternative to adhesion proteins, great progress is being made with printing growth factors (or other biochemical signals) onto scaffolds [6, 12, 21, 28, 29]. Printing growth factors onto biomaterial scaffolds offers significant advantages over allowing the growth factor to diffuse in the culture medium [5] since its spatial patterning is highly controllable. Cells seeded on the scaffold respond haptotactically to gradients of the growth factor, and undergo enhanced proliferation

where growth factor is present. Campbell *et al.* [6] and Miller *et al.* [28] examined the cellular response to patterned growth factor: both studies saw significantly higher cell densities in regions on which growth factor was bioprinted but, due to the growth-factor patterns used (in which concentration gradients were almost everywhere small), were unable to conclude with certainty whether haptotaxis might play a significant role (though they suspect it does not). While much work has been done modeling cell motility and cell proliferation as it relates to tumor growth [47], morphogenesis [25,38,39], and tumor-related angiogenesis [36], these phenomena have yet to be fully considered from a tissue engineering perspective.

In this dissertation a very versatile model of a two-dimensional perfusion bioreactor is derived, with one phase the cells and the other the culture medium, describing cell proliferation and transport in a porous scaffold perfused with nutrient-rich culture medium (see the schematic in Figure 2.1). The model domain consists of the rigid scaffold, with perfusion driven by upstream and downstream boundary conditions. The fluid flow through the scaffold is governed by Darcy's law. Cell density is monitored as proliferation occurs, and the effect of this on the flow is captured via a change in the scaffold permeability, which also changes the pore volume fraction. Cells proliferate due to nutrient uptake, and increased cell proliferation at moderate levels of fluid shear stress is also taken into account while allowing for the possibility that excessive shear stress can reduce cell proliferation. The model permits different nutrient basic types to be considered; for example, nutrients that become toxic in excess, and those that do not. Nutrient is transported by advection and diffusion (advective transport is shown to dominate in all relevant parameter regimes). Cell proliferation due to nutrient uptake, and the nutrient uptake itself, are modeled by the same basic functional form, reflecting the assumption that the new cell mass created is proportional to the amount of nutrient consumed. The cells move within the scaffold via cellular diffusion in response to overcrowding and a

small advective velocity (proportional to the speed of the fluid flow; essentially, a fluid drag). The model is then extended in three ways: a haptotactic component is added to the cellular flux to model the effect of a non-diffusible growth factor bound to the scaffold (growth factor enhanced proliferation [28] is addressed by a supplemental growth term in the same equation); the effects of (relatively rapid) cyclic compression of the seeded scaffold are examined by exploiting a two-timescale analysis; and the natural cellular death rate, assumed constant at first, is modified to be a function of local fluid flow (the reasons for which are discussed later).

This dissertation is laid out as follows. In Chapter 2 the model is developed in full, and nondimensionalized. Chapter 3 summarizes the nondimensional model as well as relevant dimensional and dimensionless parameters used in the simulations. Simulations are run using the basic model in Chapter 4 with numerous different initial cell seedings. In this chapter, we also test the effect of varying parameter values and demonstrate the versatility of the model to large changes in constituent functional forms as well as the robustness to small differences in these forms. The basic model is an introductory attempt to simulate a real tissue engineering experiment within a perfusion bioreactor. Since such experiments are highly complex it is difficult to properly account for every aspect, hence there are factors (such as specific pore architecture) that this dissertation does not address. The basic results as presented, and the extensions which follow are simply intended to provide an introduction to the breadth and capabilities of the model.

The effect of bioprinting a growth factor onto the scaffold is investigated in Chapter 5 as we attempt to direct and predict the final cell density based on initial seedings. Cyclic compression of the scaffold is modeled in Chapter 6 to show that the model can not only capture effects on the long time scale of cell proliferation but it can also capture effects on the short timescale of fluid flow. Chapter 7 presents a brief investigation of two further scenarios that could be modeled: a higher

death rate in stagnant flow zones (modeling the fact that toxins can build up where flow is insufficient to flush them out); and proliferation on a scaffold of nonuniform permeability (this is one possible means of controlling the final distribution of tissue). We conclude with a short discussion of our results, and of possible future directions in Chapter 8.

CHAPTER 2

MODEL FORMULATION

2.1 Dimensional Formulation

We begin by formulating a fully dimensional model, in which asterisks denote dimensional quantities. The experimental set-up is sketched in Figure 2.1 where the scaffold domain is a square two-dimensional Cartesian grid with $\boldsymbol{x}^* = (x^*, y^*)$ in which culture medium flows from $x^* = 0$ to $x^* = L^*$ with fixed impenetrable walls at $y^* = 0,\ y^* = L^*$. Time is denoted by t^*. Dependent variables in general depend

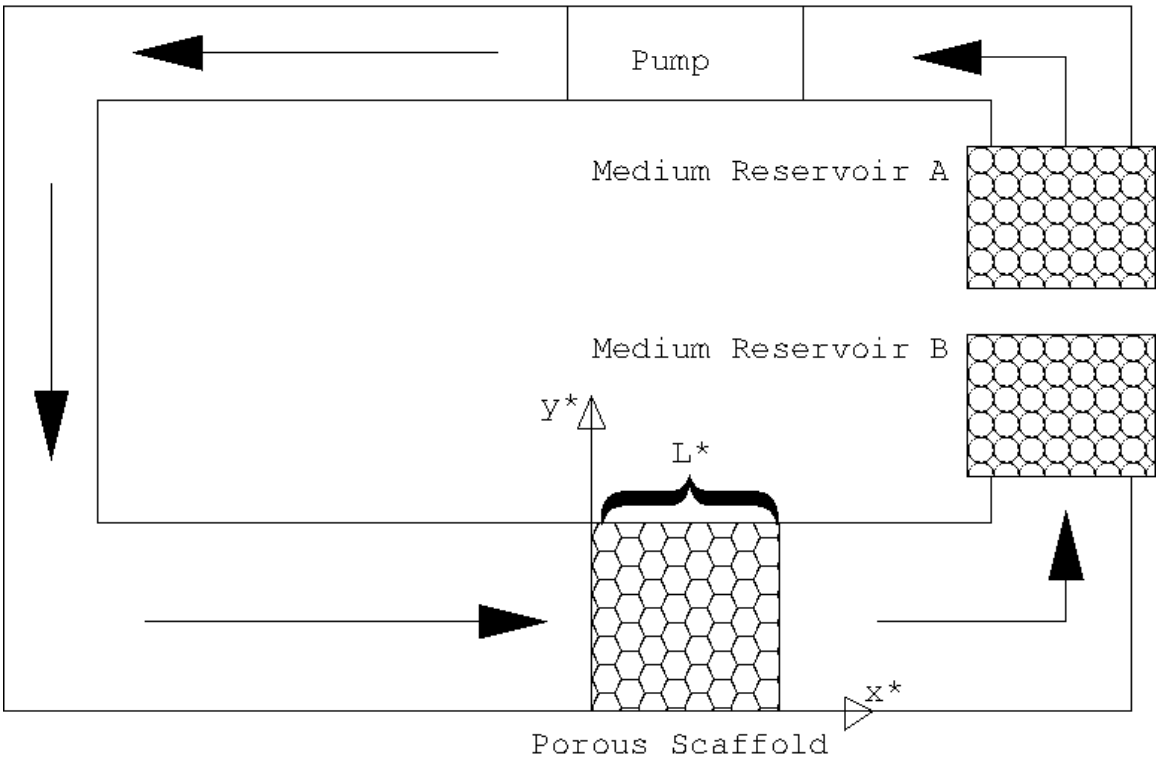

Figure 2.1 Experimental set-up.

on both space and time: but except where we wish to emphasize this dependence we will suppress it, for brevity. The culture medium flows at velocity $\boldsymbol{u}^*$ and pressure p^* according to Darcy's law, where the scaffold permeability is a function of c^*, the

local cell density. The culture medium contains nutrient at a concentration n^*. The nutrient concentration is governed by an advection-diffusion-reaction equation with advective velocity $\boldsymbol{u}^*$ and an uptake term (sink) due to nutrient consumption by the cells. We model the cell density c^* by considering basic mass conservation principles, incorporating proliferation (source) terms due to the nutrient consumption (with shear stress dependent growth rate) and local growth factor concentration. We also account for cell death, which may in practice be due to several factors (natural death, death due to locally low nutrient concentration, death due to excessively high local shear, etc). We discuss each of the model components in more detail below.

2.1.1 Fluid Flow

The culture medium forced through the seeded porous scaffold is assumed to be a Newtonian fluid with (constant) viscosity μ^*. The scaffold permeability, k^*, will change as cells proliferate and fill the pores, thus we take k^* to be a function of local cell density: $k^*(c^*)$. We assume Darcy's Law

$$\boldsymbol{u}^* = -\frac{k^*(c^*)}{\mu^*}\nabla^* p^*, \tag{2.1}$$

where $\boldsymbol{u}^*$ is the flow velocity and p^* is the pressure. The continuity (incompressibility) equation is

$$\nabla^* \cdot \boldsymbol{u}^* = 0, \tag{2.2}$$

which gives

$$\nabla^* \cdot (k^*(c^*)\nabla^* p^*) = 0. \tag{2.3}$$

This equation must be coupled to a model for c^*, and suitable boundary conditions imposed on the pressure (or the velocity).

2.1.2 Nutrient Concentration

The culture medium transfers nutrient to the cells within the scaffold; and also (via the local fluid dynamics) exposes the cells to shear stress, which we assume affects the local proliferation rate and hence the nutrient uptake rate. The concentration of nutrient in the culture medium, n^*, satisfies an advection-diffusion-reaction equation,

$$n^*_{t^*} + \boldsymbol{u}^* \cdot \nabla^* n^* = D^* \nabla^{*2} n^* - \theta^* g^*(n^*, c^*, \tau_s^*), \tag{2.4}$$

where subscripts t^* denote partial differentiation with respect to t^*. The nutrient is convected with the local flow velocity; it simultaneously diffuses (with diffusion coefficient D^*) and is consumed (by the cells) at a rate (θ^*) that is modulated according to the consumption function $g(n^*, c^*, \tau_s^*)$ by both n^* and c^*, as well as by shear stress τ_s^* due to the local fluid dynamics.

2.1.3 Cell Density

The cells satisfy a basic conservation of mass principle in which, within any fixed control volume V^* (bounded by surface S^*, with outward normal $\boldsymbol{n}$), their rate of increase is equal to their rate of creation, minus their rate of death. If their local flux at any point within the domain is $\boldsymbol{J}_c^*$ then the principle of mass conservation gives

$$\begin{aligned} \frac{d}{dt^*} \int_{V^*} c^* \, dV^* &= -\int_{S^*} \boldsymbol{J}_c^* \cdot \boldsymbol{n} \, dS^* + \int_{V^*} (\text{sources}) \, dV^* - \int_{V^*} (\text{sinks}) \, dV^* \\ &= -\int_{V^*} \nabla^* \cdot \boldsymbol{J_c}^* \, dV^* + \int_{V^*} (\text{sources}) \, dV^* - \int_{V^*} (\text{sinks}) \, dV^* \end{aligned} \tag{2.5}$$

using the Divergence theorem.

This principle of mass conservation yields a PDE for the evolution of the cell density $c^*(\boldsymbol{x}^*, t^*)$, the exact form of which depends on what we assume about the flux $\boldsymbol{J}_c^*$ and the sources/sinks. The flux may consist of several contributions. The first follows from Fick's first law [14], that cells will move down a gradient from a higher concentration to

a lower concentration to avoid overcrowding and competition for resources. Another possibility is that the cells will be dragged through the scaffold by the fluid, and we will assume that this local advective velocity, $\boldsymbol{u}_c^*$, is proportional to the fluid pore velocity itself. As we will argue later, $\boldsymbol{u}_c^*$ will generally be considered to be small relative to the flow velocity, as cell proliferation is highest when cells adhere to the scaffold. The combination of these two contributions constitutes the standard total flux term,

$$\boldsymbol{J}_c^* = \boldsymbol{u}_c^* c - D_c^* \nabla^* c^*, \tag{2.6}$$

where $\boldsymbol{u}_c^* = \delta \boldsymbol{u}_p^*$ is the drag proportional to the fluid drag, assumed proportional to the fluid pore velocity, u_p^* (discussed in §2.3.1 later), with $\delta \ll 1$; and D_c^* is the cellular diffusion coefficient. This leads to the advection-diffusion equation for c^*,

$$\frac{\partial c^*}{\partial t^*} + \boldsymbol{u}_c^* \cdot \nabla^* c^* = D_c^* \nabla^{*2} c^* + \textit{sources} - \textit{sinks}. \tag{2.7}$$

There are many possible functional forms that one could use for the source/sink terms representing proliferation and cell death, respectively, but a simple and reasonable possibility is to assume that the source term is proportional to the nutrient consumption function introduced above, while death is proportional to how many live cells are present. These assumptions give the advection-diffusion equation

$$\frac{\partial c^*}{\partial t^*} + \boldsymbol{u}_c^* \cdot \nabla^* c^* = D_c^* \nabla^{*2} c^* + \lambda^* g^*(n^*, c^*, \tau_s^*) - \nu^* c^*, \tag{2.8}$$

where $g^*(n^*, c^*, \tau_s^*)$, represents cell proliferation due to nutrient uptake, with constant rate λ^*, and ν^* is the per-capita death rate (at first assumed constant).

2.2 Nondimensionalization

Before we propose specific functional forms for $g^*(n^*, c^*, \tau_s^*)$, $k^*(c^*)$, etc, we nondimensionalize the system (2.1)-(2.8). This process leads to the identification

of several dimensionless parameters; in some cases, these parameters will be small, enabling us to simplify the model by neglecting certain terms. We non-dimensionalize as follows,

$$\boldsymbol{x}^* = L^*\boldsymbol{x},\ t^* = t/\lambda^*,\ k^*(c^*) = k_s^* k(c), \tag{2.9}$$

$$\boldsymbol{u}^* = u_0^*\boldsymbol{u},\ p^* = \frac{\mu^* L^* u_0^*}{k_s^*} p,\ n^* = n_0^* n,\ c^* = c_0^* c, \tag{2.10}$$

$$g^*(n^*, c^*, \tau_s^*) = c_0^* g(n, c, \tau_s). \tag{2.11}$$

Lengths are non-dimensionalized with respect to the length of the scaffold domain, L^*. We have chosen $(1/\lambda^*)$, the rate of cell proliferation, as the representative timescale, appropriate for analyzing the long times over which cells proliferate. The velocity scale, u_0^*, is defined as the pump flow rate, U_0^*, divided by the length scale $(u_0^* = U_0^*/L^*)$, and is discussed further in Chapter 3. The pressure scale comes from balancing the terms in Darcy's Law (2.1), where k_s^* is the permeability of the unseeded scaffold (assumed constant). We non-dimensionalize the nutrient concentration with the nutrient concentration at the inlet, n_0^* (also assumed constant), and the cell density with a representative cell density, c_0^*. The growth/uptake function g^* is also non-dimensionalized via c_0^*, and the growth factor concentration by a representative value, ρ_0^* (determined in practice by an experimentalist). The resulting dimensionless model is summarized below.

2.2.1 Fluid Flow

Darcy's law (2.1) and the continuity equation (2.2) are

$$\boldsymbol{u} = -k(c)\nabla p \text{ and } \nabla \cdot \boldsymbol{u} = 0. \tag{2.12}$$

2.2.2 Nutrient Concentration

The dimensionless form of equation (2.4) is

$$\epsilon n_t + \boldsymbol{u} \cdot \nabla n = D\nabla^2 n - \theta g(n, c, \tau_s), \tag{2.13}$$

where $\epsilon = (L^*\lambda^*)/u_0^*$, $D = D^*/(u_0^* L^*)$, and $\theta = (\theta^* L^* c_0^*)/(u_0^* n_0^*)$. From typical experimental data, [32], we have significant cell proliferation over the first five to seven days, and we choose a characteristic fluid velocity of 5 cm/s (see Table 3.3 in Chapter 3) and a characteristic length of 1cm. Working with $1/\lambda^* = 5$ days $= 4.32 \times 10^5$s, we have

$$\epsilon = \frac{L^*\lambda^*}{u_0^*} = \frac{1\text{cm}}{5\text{cm/s} \cdot 4.32 \times 10^5\text{s}} = \frac{1}{2.16 \times 10^6} \ll 1. \tag{2.14}$$

We assume that θ is $O(1)$ with respect to ϵ and neglect the term of $O(\epsilon)$ in equation (2.13) (this assumption on θ will be relaxed later in Chapter 6 in order to make analytical progress with the cyclic loading problem). As will later be seen in Table 3.3, the dimensionless coefficient of nutrient diffusion, D, is comparable to ϵ, hence we also neglect nutrient diffusion in the scaffold. The leading-order (quasi-steady) nutrient concentration equation is then

$$\boldsymbol{u} \cdot \nabla n = -\theta g(n, c, \tau_s). \tag{2.15}$$

2.2.3 Cell Density

The dimensionless form of (2.8) is

$$c_t + \frac{\delta}{\epsilon}\boldsymbol{u}_p \cdot \nabla c = D_c \nabla^2 c + g(n, c, \tau_s) - \nu c, \tag{2.16}$$

where $D_c = D_c^*/(\lambda^* L^{*2})$ and $\nu = \nu^*/\lambda^*$. The parameters δ (introduced just after equation (2.6)) and ϵ (defined in equation (2.14) above) are both small, but the size of the ratio δ/ϵ depends on how strongly the cells are adhered to the scaffold. We assume $\delta/\epsilon \leq O(1)$.

2.3 Specification of Functional Forms

There are two functions whose forms are still unspecified: the cell proliferation/nutrient uptake function $g(n, c, \tau_s)$ in equations (2.15) and (2.16), and the permeability function $k(c)$ in equation (2.12). In the following sections, specific functional forms will be proposed, but these are easily modified within the model framework. The model is very versatile, and as will be demonstrated in §4.3 the specific functional forms are relatively unimportant provided the correct qualitative behavior is captured (e.g., the same limit approaching infinity).

2.3.1 Shear Stress

In addition to the obvious dependence on local nutrient concentration and cell density, we assume the cell proliferation rate to depend on the local shear stress experienced by the cells within the scaffold [22]. Since Darcy's Law does not allow for explicit computation of shear stresses, we need to find some way to estimate these. If we suppose, for example, that the scaffold itself is made up of an assemblage of hollow circular tubes, then this leads to a Poiseuille velocity profile within each tube itself. If we know the flow within the tube, we can then calculate the shear stress [1]. With Poiseuille velocity in the empty tube $\boldsymbol{u}^*_{Pois}$, the shear stress at the channel wall is

$$\tau_s^* = \mu^* \frac{\partial \boldsymbol{u}^*_{Pois}}{\partial r^*}, \tag{2.17}$$

where here μ^* is the fluid viscosity, and r^* is the radial coordinate measured from the tube's center. If we were solving the fully three-dimensional fluid flow problem within each pore, then we would have a no-slip boundary condition on the pore interior and we would be able to calculate the shear stress directly via an equation similar to that above.

In our model, though, we are not calculating the fluid flow within each pore, but we are instead using Darcy's Law to calculate the fluid velocity, averaged over

many pores. Here, Darcy's Law predicts the local average fluid flow on a lengthscale that is long compared with an individual pore size, but small compared with the structure as a whole. This empirical averaging reduces the order of the model, and as such only allows for a non-penetrative boundary condition at the wall, removing the no-slip condition. Once we have the local average fluid velocity, we can calculate the mean pore velocity, $\boldsymbol{u}_p^* = |\boldsymbol{u}^*|/\phi$, where ϕ is the void fraction of the porous medium (the portion through which fluid may flow; a dimensionless number between zero and 1). From this we can estimate the size of the shear stress from (2.17) as

$$\tau_s^* \sim \mu^* \frac{|\boldsymbol{u}_p^*|}{d^*} = \mu^* \frac{|\boldsymbol{u}^*|}{\phi d^*}, \tag{2.18}$$

where d^* is the average pore size.

2.3.2 Permeability and Void Fraction

Over a given control volume, which is large compared with an individual pore yet small when compared to the whole scaffold, we have the void fraction (also known as porosity), ϕ defined (in [42] among other places) as

$$\phi = \frac{\text{total pore volume}}{\text{control volume}}. \tag{2.19}$$

The permeability $k^*(c^*)$, which appears in Darcy's Law, depends to some extent on the shape and connectivity of the pores, but ϕ and $k^*(c^*)$ are related for a given 'type' of porous medium. Permeability is a measure of the ease of flow through a porous medium, and for a given pore type, $k^*(c^*)$ is a monotone increasing function of ϕ. A porous medium with no pores, $\phi = 0$, is impermeable, $k^*(c^*) = 0$, and one that is entirely made up of empty pores, $\phi = 1$, is infinitely permeable, $k^* \to \infty$. A function which immediately satisfies this is of the form

$$k^*(c^*) = k_s^* \frac{A\phi^\sigma}{1 - \phi^\sigma}, \tag{2.20}$$

where A is a dimensionless constant, k_s^* is the characteristic permeability scale chosen as the permeability of the unseeded scaffold, and $\sigma \geq 1$ is an exponent. As the mean pore velocity takes into account the void fraction itself, it is helpful to rearrange this equation into one where ϕ depends on the permeability. Since $k^*(c^*) = k_s^* k = k_s^* A\phi^\sigma/(1-\phi^\sigma)$, we have

$$\phi = \left(\frac{k/A}{1+k/A}\right)^{1/\sigma}. \tag{2.21}$$

We can see in Figure 2.2 that this functional form satisfies the conditions that we want. Since $|\boldsymbol{u}_p^*| = |\boldsymbol{u}^*|/\phi$ (equation (2.18)), and we now have a functional form for

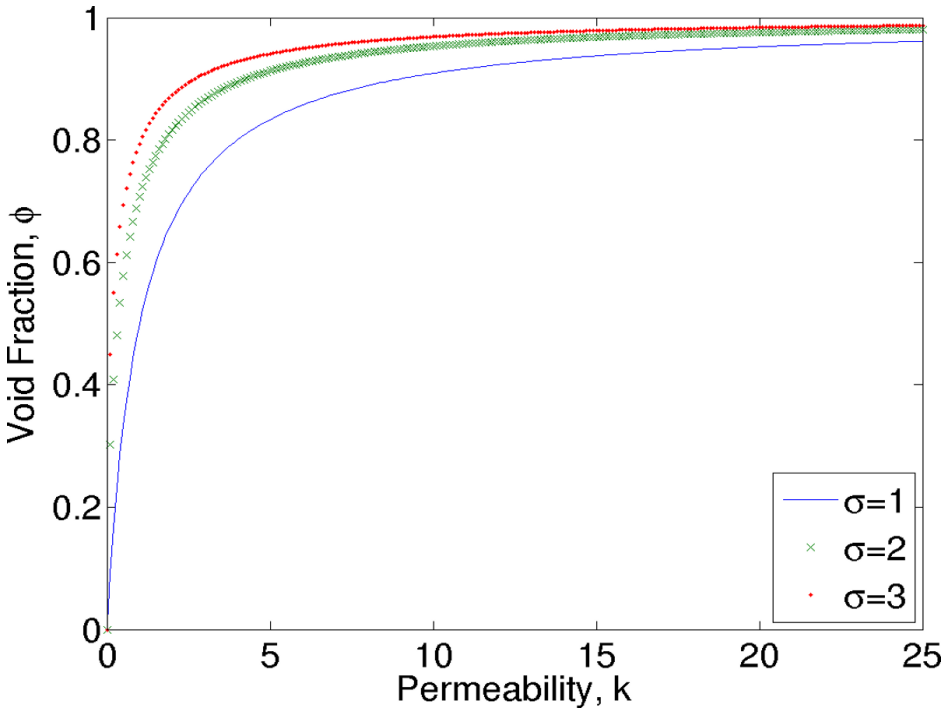

Figure 2.2 Plot of $\phi = \left(\frac{k/A}{1+k/A}\right)^{1/\sigma}$ with $A = 1$ and $\sigma = 1, 2, 3$.

the void fraction, we can insert equation (2.21) into equation (2.18) to get

$$\tau_s^* \sim \frac{\mu^*|\boldsymbol{u}^*|}{d^*}\left(\frac{A+k}{k}\right)^{1/\sigma}. \tag{2.22}$$

2.3.3 Permeability and Pore Size

We want to incorporate the shear stress (2.22) into the model without having to explicitly estimate mean pore size. O'Brien *et al.* [33] derived an equation relating permeability of a scaffold to mean pore size (and other quantities): for our model this relation reduces to $k^*(c^*) \propto d^{*2}$ (see also [42]). This is the relation we will use in the first approximation, which when included in equation (2.22) gives

$$\tau_s^* \sim \frac{\mu^* |\boldsymbol{u}^*| (1+k)^{1/\sigma}}{\sqrt{k_s^*} k^{(\frac{1}{2}+\frac{1}{\sigma})}}. \tag{2.23}$$

We see that a choice for the exponent, σ, in (2.21) which simplifies the model is $\sigma = 2$, and (2.23) then becomes

$$\tau_s^* \sim \frac{\mu^* |\boldsymbol{u}^*| \sqrt{1+k(c)}}{\sqrt{k_s^*} k(c)}. \tag{2.24}$$

If we then recall that this model includes flow which is governed by Darcy's Law, $u^* = -(k^*(c^*)/\mu^*)\nabla^* p^*$, equation (2.24) then becomes

$$\tau_s^* \sim \left| -\frac{\sqrt{k_s^*} p_0^* k(c) \nabla p}{L^* \mu^*} \right| \mu^* \frac{\sqrt{1+k(c)}}{k(c)}, \tag{2.25}$$

and if we set the representative shear stress scaling as $\tau_{s0}^* \sim (|p_0^*|\sqrt{k_s^*})/L^*$ (with the representative pressure scale p_0^* implicitly defined in equation (2.10) as $p_0^* = \mu^* L^* u_0^*/k_s^*$) we obtain

$$\tau_s^* = \tau_{s0}^* \tau_s \sim |p_0^* \nabla p| \frac{\sqrt{k_s^*}}{L^*} \sqrt{1+k(c)} = \tau_{s0}^* |\nabla p| \sqrt{1+k(c)}. \tag{2.26}$$

Thus, our dimensionless shear stress estimate is

$$\tau_s \sim \sqrt{1+k(c)} |\nabla p|. \tag{2.27}$$

2.3.4 Permeability as a Function of Cell Density

The permeability should be a function of the local cell density. We also want the permeability to satisfy the property that as $c^* \to 0,\ k^*(c^*) \to k_s^*$ (recall that k_s^* is the

permeability of the unseeded scaffold), and as $c^* \to \infty,\ k^*(c^*) \to 0$. A simple general form which satisfies these properties is

$$k^*(c^*) = \frac{k_s^* a^{*\beta}}{a^{*\beta} + c^{*\beta}},$$

where a^* has dimensions of concentration and thus we can scale it with c_0^*, and $\beta > 1$ is dimensionless. Then we have

$$k^*(c^*) = k_s^* k(c) = \frac{k_s^* a^{\beta}}{a^{\beta} + c^{\beta}},$$

and we set $a = 1$ and choose $\beta = 2$ to get

$$k^*(c^*) = k_s^* k(c) = k_s^* \frac{1}{1 + c^2}, \tag{2.28}$$

as our permeability in terms of the local cell density. We see in Figure 2.3 that the choice of $\beta = 2$ is reasonable as it allows for a relatively gradual decrease in permeability as opposed to the steeper decreases incurred by the choice of $\beta > 2$.

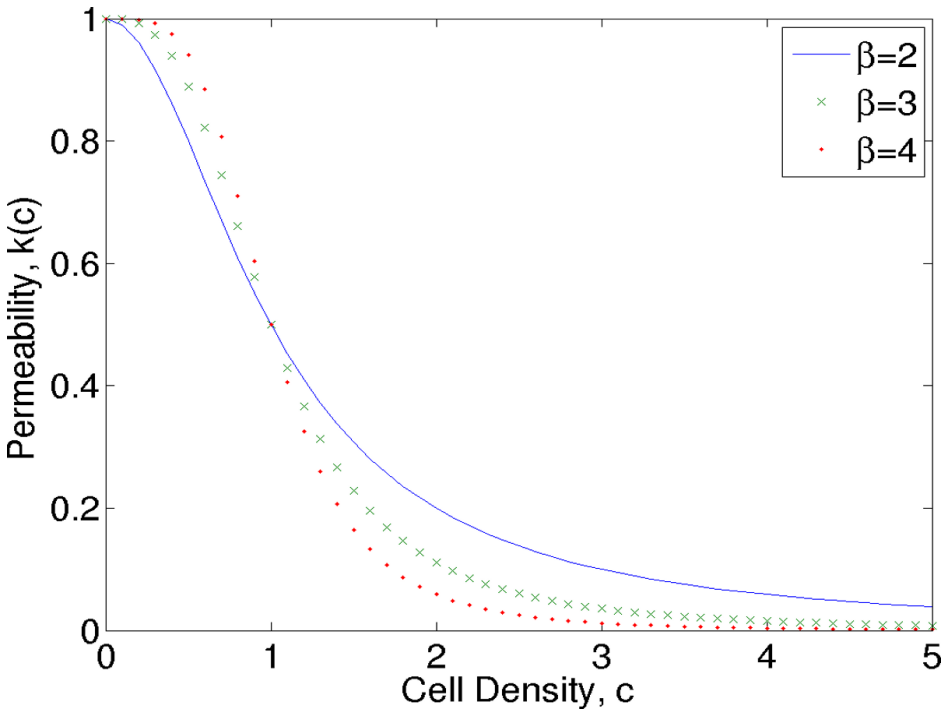

Figure 2.3 Plot of $k(c) = \frac{a^\beta}{a^\beta + c^\beta}$ with $a = 1$ and $\beta = 2, 3, 4$.

2.3.5 Nutrient Uptake/Cell Growth Function

We use the same functional form for the nutrient uptake and cell proliferation rates, reflecting an assumption that cell proliferation is proportional to nutrient consumed. Since we anticipate that at low cell numbers proliferation will occur at a rate proportional to the cell density, but at high cell numbers overcrowding and competition for resources will lead to saturation, we choose a logistic model for $g(n, c, \tau_s)$,

$$g(n, c, \tau_s) = G(\tau_s)c\left(1 - \frac{c}{\hat{c}(n)}\right), \tag{2.29}$$

where the carrying capacity, $\hat{c}(n)$, depends on local nutrient availability and $G(\tau_s)$ will be chosen to incorporate the shear stress dependence. Specific choices of $\hat{c}(n)$ can model different scenarios; we choose

$$\hat{c}(n) = \frac{\hat{c}_0 n}{1 + n^2}, \tag{2.30}$$

which, since $\hat{c}(n) \to 0$ as $n \to \infty$, implicitly assumes that excessive nutrient concentration is toxic (for example, oxygen is known to be toxic to chondrocytes in excess). However, increasing the exponent of n in the numerator to 2 can easily incorporate non-toxicity for large nutrient levels as seen in Figure 2.4. The coefficient, $\hat{c}_0 = 10$ is chosen to allow significant cell proliferation over experimental timescales; again this is easily modified if experimental data suggest a different value.

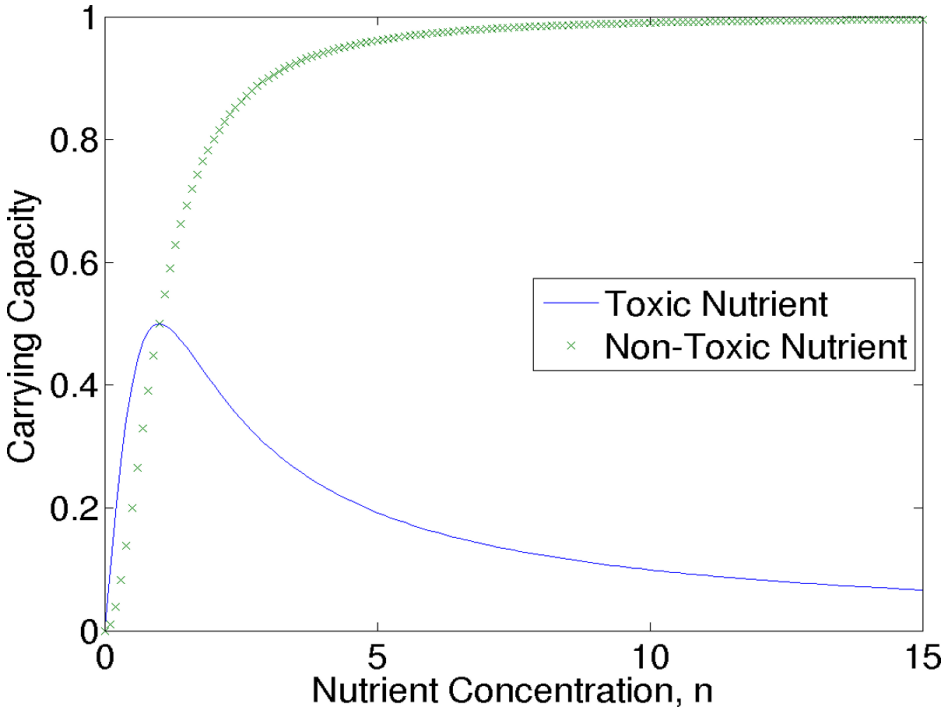

Figure 2.4 Plot of toxic $\left(\hat{c}(n) = \frac{\hat{c}_0 n}{1+n^2}\right)$ and non-toxic $\left(\hat{c}(n) = \frac{\hat{c}_0 n^2}{1+n^2}\right)$ carrying capacity functions (i.e. changing the exponent in the numerator to 2) with $\hat{c}_0 = 10$.

2.3.6 Shear Stress Coefficient, $G(\tau_s)$

We model cells for which moderate shear stress leads to enhanced proliferation (and thus nutrient uptake), while excessive shear suppresses proliferation (and nutrient uptake). An acceptable form for the prefactor $G(\tau_s)$ in equation (2.29) is therefore

$$G(\tau_s) = \frac{\tau_s^{\eta_1}}{1 + \tau_s^{\eta_2}}, \tag{2.31}$$

where $0 < \eta_1 \leq \eta_2$. Following [22] we set $\eta_1 = 1/2$, and we choose $\eta_2 = 1$. Hence

$$G(\tau_s) = \frac{\tau_s^{1/2}}{1 + \tau_s}, \tag{2.32}$$

and its form is seen in Figure 2.5, together with curves for other values of η_2.

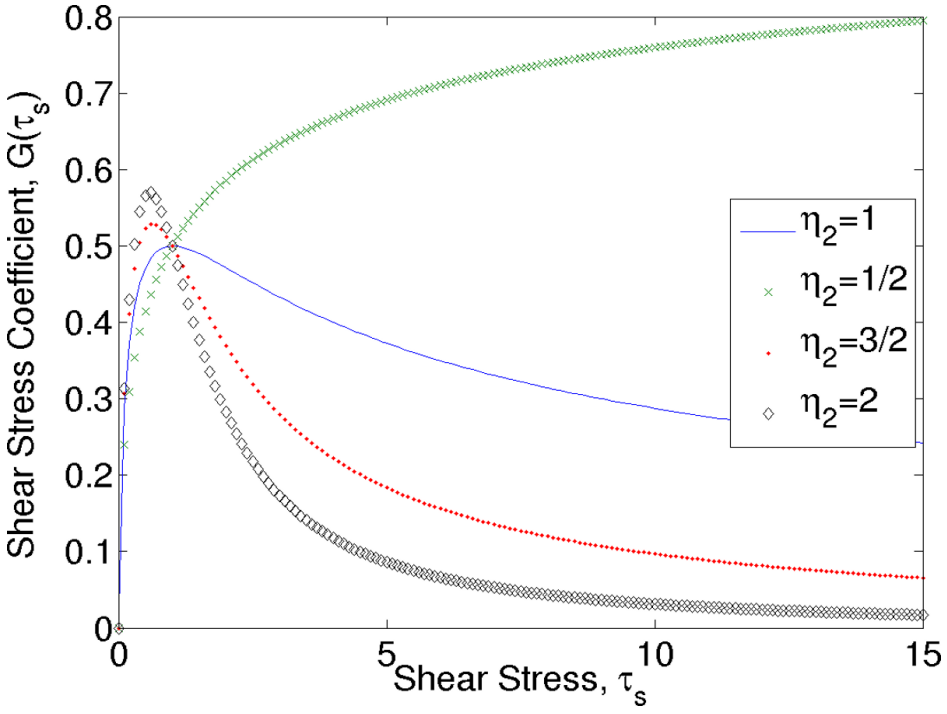

Figure 2.5 Plot of the shear stress coefficient, $G(\tau_s) = \frac{\tau_s^{1/2}}{1+\tau_s^{\eta_2}}$ with $\eta_2 = 1/2, 1, 3/2, 2$.

CHAPTER 3

MODEL SUMMARY AND BOUNDARY CONDITIONS

3.1 Introduction

Now that suitable preliminary forms for all of the constituent equations have been determined, the variables (independent and dependent), names of functions, and functional forms are summarized for easy reference. We then introduce appropriate boundary and initial conditions for the system, which includes a discussion of a rescaling that may be exploited to solve the fluid flow problem. Further extensions to the basic model considered so far are presented in later chapters.

3.2 Model Summary

Tables 3.1 and 3.2 summarize the relevant independent and dependent variables and functional forms.

Table 3.1 Summary of Variables

Independent Variables	
Variables	**Description**
(x, y)	Spatial coordinates
t	Time
Dependent Variables	
$\boldsymbol{u} = (u, v)$	Darcy velocity of culture medium
p	Pressure of culture medium
c	Cell density
n	Nutrient concentration in culture medium

Table 3.2 Summary of Functional Forms (Including Equation References)

Functional Forms	
$k(c)$	Permeability as a function of cell density, (2.28)
τ_s	Shear stress, (2.24)
$g(n, c, \tau_s)$	Cell proliferation/nutrient uptake function, (2.29)
$\hat{c}(n)$	Cellular carrying capacity as a function of nutrient, (2.30)
$G(\tau_s)$	Shear stress dependence of cell growth/nutrient uptake, (2.32)

The full dimensionless system is

$$\begin{aligned}
\boldsymbol{u} &= -k(c)\nabla p, && (3.1)\\
\nabla \cdot \boldsymbol{u} &= 0, && (3.2)\\
\boldsymbol{u} \cdot \nabla n &= -\theta g(n, c, \tau_s), && (3.3)\\
\frac{\partial c}{\partial t} + \frac{\delta}{\epsilon}\boldsymbol{u}_p \cdot \nabla c &= D_c \nabla^2 c + g(n, c, \tau_s) - \nu c, && (3.4)\\
g(n, c, \tau_s) &= G(\tau_s) c \left(1 - \frac{c}{\hat{c}(n)}\right), && (3.5)\\
\hat{c}(n) &= \frac{\hat{c}_0 n}{1 + n^2}, && (3.6)\\
G(\tau_s) &= \frac{\tau_s^{1/2}}{1 + \tau_s}, && (3.7)\\
\tau_s &= |\nabla p| \sqrt{1 + k(c)}, && (3.8)\\
k(c) &= \frac{1}{1 + c^2}. && (3.9)
\end{aligned}$$

3.3 Model Parameters

Representative values of required dimensional parameters are found in Table 3.3, and the parameters contained in the dimensionless system are in Table 3.4 (all dimensional values are for chondrocyte growth in response to oxygen).

Table 3.3 Representative Values

Scaling	**Name**	**Dimensional Value**
n_0^*	Oxygen concentration	0.2 moles/m^3 [46]
c_0^*	Cell density	4×10^{17} cells/m^3 [46]
L^*	Scaffold length	0.01 m [46]
U_0^*	Pump flow rate	5×10^{-4} m^2/s [46]
$u_0^* = U_0^*/L^*$	Fluid velocity scale	5×10^{-2} m/s [46]
θ^*	Oxygen consumption rate	1.86×10^{-18} moles/(cell·s) [32]
D_c^*	Cell diffusion coefficient	10^{-13} m^2/s [32]
λ^*	Cell proliferation timescale	2.3×10^{-6} s^{-1} [32]
ν^*	Natural cell death rate	3.3×10^{-7} s^{-1} [19]
D^*	Nutrient diffusion coefficient	1.5×10^{-9} m^2/s [46]

Table 3.4 Approximate Dimensionless Parameter Values

Parameter	**Formula**	**Dimensionless Value**
θ	$(\theta^* L^* c_0^*)/(u_0^* n_0^*)$	0.744
δ	[advective drag coefficient]	4.6×10^{-12}
D_c	$D_c^*/(\lambda^* L^{*2})$	4.3×10^{-4}
ν	ν^*/λ^*	0.1435
ϵ	$(L^*\lambda^*)/u_0^*$	4.6×10^{-7}
D	$D^*/(u_0^* L^*)$	3.0×10^{-6}

Where dimensional parameter values were not available in the literature, we simply chose values for associated dimensionless parameters as follows. For most of our simulations the ratio of the fluid velocity to the rate at which cells are advected (dragged) by the flow is chosen so that $\delta/\epsilon = 10^{-5}$ (cells strongly adhered to the scaffold). As was discussed in §2.2.2, the dimensionless nutrient diffusion coefficient,

D, is of comparable order to ϵ (Table 3.4). Since the temporal derivative was neglected in arriving at equation (2.15), the choice was made to also neglect the diffusive term in that equation, consistent with our assertion that the perfusion bioreactor set-up provides nutrient to the cells primarily via advection as opposed to diffusion.

3.4 Boundary and Initial Conditions

We now introduce the boundary and initial conditions used to solve the system (3.1)-(3.7).

3.4.1 Pressure and Fluid Velocity

Most experiments are run with a prescribed (usually constant) rate of fluid flow through the scaffold, therefore the most appropriate boundary condition on the flow is an imposed flux in the x-direction, with no-flux conditions on the y-boundaries. However, the problem for the fluid flow is most conveniently stated in terms of the elliptic PDE for the pressure,

$$\nabla \cdot (k(c)\nabla p) = 0, \tag{3.10}$$

(from equation (2.12)). If the pressure conditions at $x = 0, 1$ are known then this problem is straightforward to solve, with the additional no-flux conditions $\partial p/\partial y = 0$ on $y = 0, 1$. However, the pressure drop between entry ($x = 0$) and exit ($x = 1$) points of the domain is unknown *a priori* and, moreover, changes over time as cells proliferate in the scaffold (the pressure drop must increase as the permeability decreases to maintain a constant flow rate). We circumvent this difficulty by exploiting linearity: we solve (3.10) for the particular solution $\tilde{p}$ satisfying

$$\tilde{p}(0, y, t) = 1,\ \tilde{p}(1, y, t) = 0, \qquad \frac{\partial \tilde{p}}{\partial y}(x, 0, t) = \frac{\partial \tilde{p}}{\partial y}(x, 1, t) = 0, \tag{3.11}$$

with corresponding velocity $\tilde{\boldsymbol{u}} = -k\nabla\tilde{p}$, and flux $\tilde{Q}_0$, which may be calculated by

$$\tilde{Q}_0 = \int_0^1 -k(c)\left.\frac{\partial\tilde{p}}{\partial x}\right|_{x=l_0} dy, \tag{3.12}$$

where the integral is taken across any surface $x = l_0$ with $0 \leq l_0 \leq 1$. Without loss of generality (due to the no flux conditions at $y = 0,\ y = 1$ and incompressibility), we may take $l_0 = 0$. We then obtain the true fluid velocity as

$$\boldsymbol{u} = \frac{\tilde{\boldsymbol{u}}}{\tilde{Q}_0}. \tag{3.13}$$

A more detailed description of this rescaling is given in Shakeel *et al.* [46], where the reader is directed for further reference.

3.4.2 Cell Density

The only equation requiring an initial condition is that for cell density (equation (3.4)): we prescribe the initial cell density $c(x, y, 0)$ on $0 \leq (x, y) \leq 1$. Typically, experimentalists try to achieve a uniform initial cell-seeding density, but this is not always easy, nor is it clear that this is the optimal strategy. Our model allows us to investigate how different initial seeding patterns evolve over time, under various experimental conditions.

We also require suitable boundary conditions for the cell density equation. We assume that there is no net flux of cells into or out of the scaffold at the upstream or downstream ends, as well as no net flux through either of the impermeable walls at $y = 0, 1$. This may not be entirely correct as the scaffold is suspended in a fluid domain, which allows for the possibility of a small flux into or out of the scaffold: nonetheless it is a reasonable assumption. With the total cell flux defined as

$$\boldsymbol{J}_c = (\delta/\epsilon)\boldsymbol{u}_p c - D_c\nabla c, \tag{3.14}$$

the dimensionless boundary conditions on the cell density equation at all spatial boundaries are

$$\boldsymbol{J}_c \cdot \hat{\boldsymbol{n}} = 0, \tag{3.15}$$

where $\hat{\boldsymbol{n}}$ is the outward unit normal at each boundary.

3.4.3 Culture Medium

Assuming that fresh nutrient is supplied at fixed concentration, our nondimensionalization (2.10) gives the appropriate boundary condition at the inlet $x = 0$ as

$$n(0, y, t) = 1. \tag{3.16}$$

CHAPTER 4

BASIC MODEL RESULTS

In this chapter, we first outline the numerical methods used to solve the system (3.1)-(3.4). We then give some sample numerical results for this basic model, before examining its robustness to changes in the various functional forms that were proposed in Chapter 2. The effect of parameter variation is also investigated for this basic model, before we proceed to new extensions of the model in Chapters 5-7.

4.1 Numerical Method

While several variants of the model (equations (3.1)-(3.4)) will be considered in this dissertation, the basic numerical scheme, presented here, will not fundamentally change unless otherwise noted. The first step in solving the system consists of assigning an initial cell seeding, which (via equation (3.9)) determines an initial scaffold permeability.

4.1.1 Pressure

Equations (3.1) and (3.2) then combine to form

$$\nabla \cdot (k(c)\nabla p) = 0, \tag{4.1}$$

which is solved, subject to the unit pressure drop boundary conditions (3.11), using a finite volume method. A sample control volume on which the method is performed is shown in Figure 4.1. The discretization for solving equation (4.1) is

$$-a_S p_S - a_W p_W + a_P p_P - a_E p_E - a_N p_N = b, \tag{4.2}$$

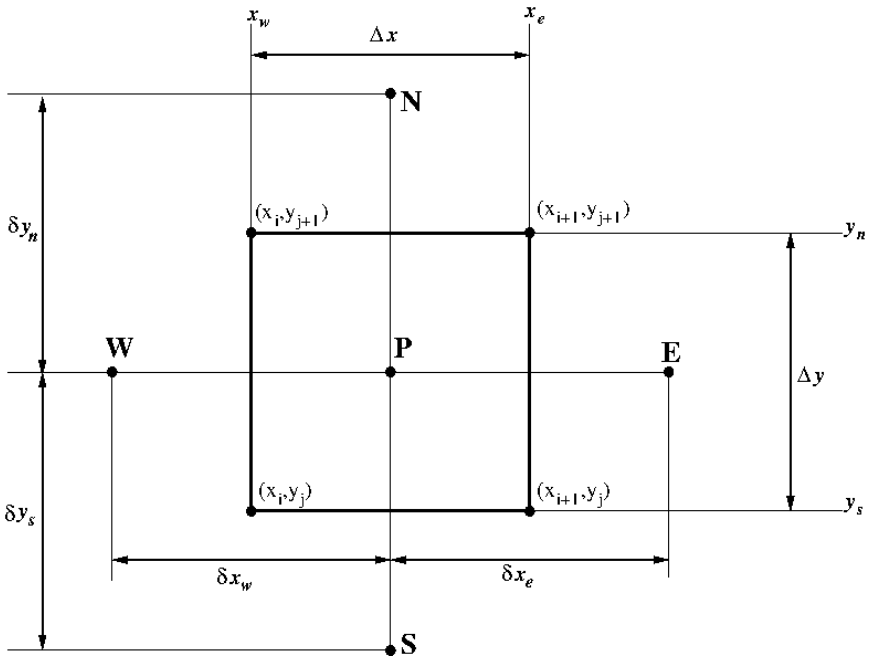

Figure 4.1 Sample control volume for the finite volume method used.

where b contains boundary data,

$$a_E = \frac{k_e}{\Delta x \delta x_e}, \tag{4.3}$$

$$a_W = \frac{k_w}{\Delta x \delta x_w}, \tag{4.4}$$

$$a_N = \frac{k_n}{\Delta y \delta y_n}, \tag{4.5}$$

$$a_S = \frac{k_s}{\Delta y \delta y_s}, \tag{4.6}$$

$$a_P = a_E + a_W + a_N + a_S, \tag{4.7}$$

and capital letters refer to points while lower case letters refer to the edge of the control volume. The discretization is set up to find solutions at the centers of boxes created by the prescribed grid, and because of this it allows for simple inclusion of the Dirichlet boundary data at $x = 0, 1$ and Neumann boundary data at $y = 0, 1$. The built-in MATLAB GMRES program is used to solve the pressure equation at the aforementioned centers of the boxes, and a MATLAB command "TriScatteredInterp"

is used to extrapolate the data back onto the desired grid space. From this pressure solution we determine the fluid velocity corresponding to a unitary pressure drop from Darcy's law, and calculate the total flux, $\tilde{Q}_0$, as in equation (3.12). We then determine the true fluid velocity in the domain via equation (3.13).

4.1.2 Nutrient Concentration

We solve for the "initial" nutrient concentration in the scaffold by solving equation (3.3) via an upwind finite difference method from $x = 0$ to $x = 1$. The method is

$$\frac{n_{i+1,j} - n_{i,j}}{\Delta x} + a_+ \frac{n_{i,j} - n_{i,j-1}}{\Delta y} + a_- \frac{n_{i,j+1} - n_{i,j}}{\Delta y} = -\theta g(c_{i,j}, n_{i,j}, \tau_{s_{i,j}}), \tag{4.8}$$

$$a_+ = max\left\{\frac{v_{i,j}}{u_{i,j}}, 0\right\},\ a_- = min\left\{\frac{v_{i,j}}{u_{i,j}}, 0\right\}, \tag{4.9}$$

where $\boldsymbol{u} = (u, v)$. This method can be used because in all cases we consider, flow is unidirectional with respect to the $x-$component of the velocity, thus $u_{i,j}$ is always positive.

4.1.3 Cell Density

The advective drag experienced by the cells is then determined as a ratio of the fluid velocity by $(\delta/\epsilon)\boldsymbol{u}$ and the cell density is calculated at the subsequent time step using a semi-implicit ADI-type method (the nonlinear proliferation term is dealt with explicitly). The ADI-type method is

$$\begin{aligned}
&\frac{c_{i,j}^{t+1/2} - c_{i,j}^{t}}{\Delta t/2} + \frac{\delta}{\epsilon} u_{i,j} \delta_x c_{i,j}^{t+1/2} + \frac{\delta}{\epsilon} v_{i,j} \delta_y c_{i,j}^{t} = \\
&\qquad = D_c(\delta_x^2 c_{i,j}^{t+1/2} + \delta_y^2 c_{i,j}^{t}) + g(c_{i,j}^{t}, n_{i,j}^{t}, \tau_{s_{i,j}}^{t}) - \nu c_{i,j}^{t} \qquad (4.10) \\
&\frac{c_{i,j}^{t+1} - c_{i,j}^{t+1/2}}{\Delta t/2} + \frac{\delta}{\epsilon} u_{i,j} \delta_x c_{i,j}^{t+1/2} + \frac{\delta}{\epsilon} v_{i,j} \delta_y c_{i,j}^{t+1} = \\
&\qquad = D_c(\delta_x^2 c_{i,j}^{t+1/2} + \delta_y^2 c_{i,j}^{t+1}) + g(c_{i,j}^{t+1/2}, n_{i,j}^{t}, \tau_{s_{i,j}}^{t}) - \nu c_{i,j}^{t+1/2} \qquad (4.11)
\end{aligned}$$

This process is then repeated until the user-defined end time is attained. The solution method described is first order in time and first order in space, as can be seen in Figures 4.2 and 4.3.

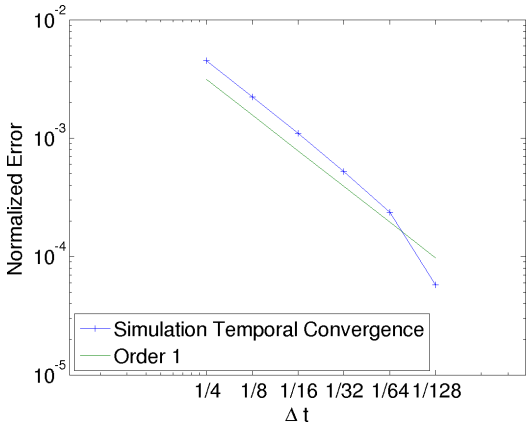

Figure 4.2 Temporal convergence of the basic mathematical model.

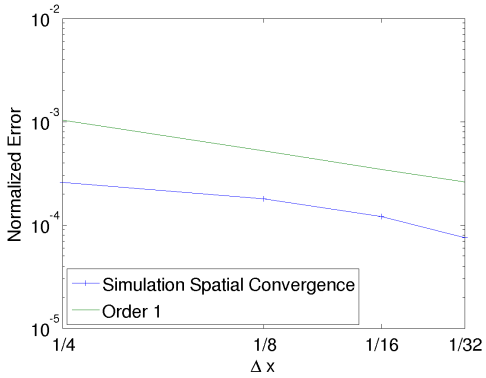

Figure 4.3 Spatial convergence of the basic mathematical model.

4.2 Results

The results are presented in separate subsections based on the initial cell density seeding chosen for each simulation. We first consider very simple initial cell density seedings, and then increase in spatial complexity. The model parameters used for the first simulations are those presented in Table 3.4, although some later results will be presented with varying parameters to demonstrate the effect of changing parameters. The parameters for the numerical simulation (step size, time steps, etc) are presented in Table 4.1. Finally, the basic model (equations (3.1)-(3.7)) is used to present the flexibility and robustness of the model as a whole; the last set of results in this chapter will show the relative lack of difference when using different functions for the constituent parts of the system equations (3.8)-(3.7).

Table 4.1 Input Specified for the Numerical Simulation of the Model

NX,NY	Steps in x and y direction	32
dx, dy	Step size	0.03125
T	Time steps	100
t_0	Initial time	0 days
t_n	Final time	5 days

4.2.1 Constant Initial Cell Density

We first consider uniform cell seeding throughout the entire domain. We start with this choice as it is the simplest to see and analyze and also also it is widely believed that a uniform initial cell density is most likely to lead to a uniform density at large times [3]. The results from simulations with initial cell density $c(x, y, 0) = 1$ are shown in Figures 4.4-4.7. As can be seen, the cell density remains relatively uniform over the course of the experiment, while increasing. The figures also indicate a slightly higher cell density (as indicated by the shades of red) near $x = 0$, which is a result of the fresh nutrient being delivered to the scaffold at $x = 0$. The cells here are thus exposed to the highest concentration (and therefore consume more nutrient), while cells downstream see slightly depleted nutrient levels.

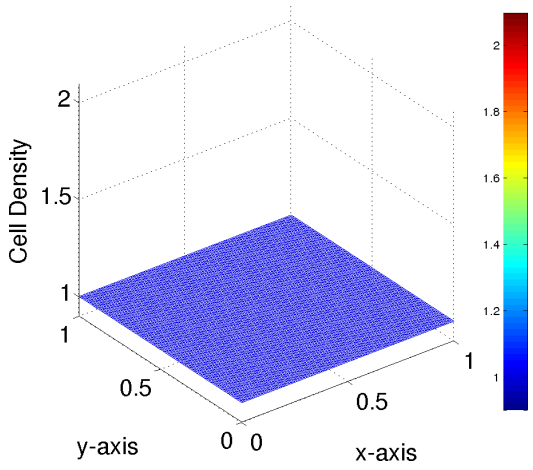

Figure 4.4 Initial constant cell seeding.

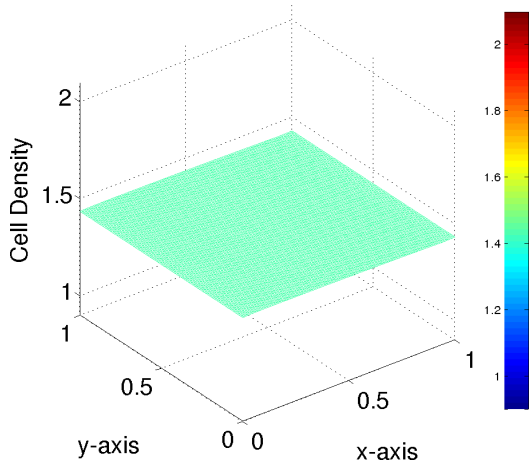

Figure 4.5 Cell density at 240 hours (10 days).

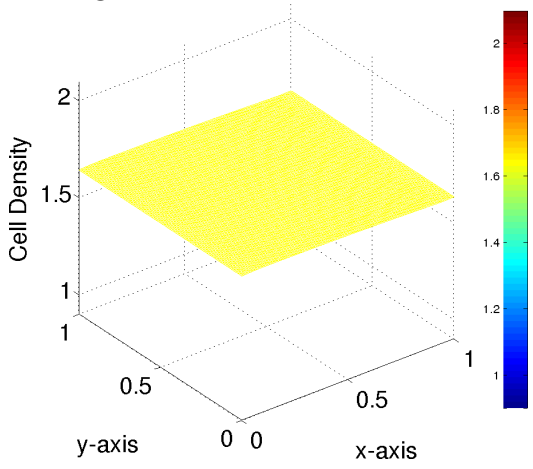

Figure 4.6 Cell density at 360 hours (15 days).

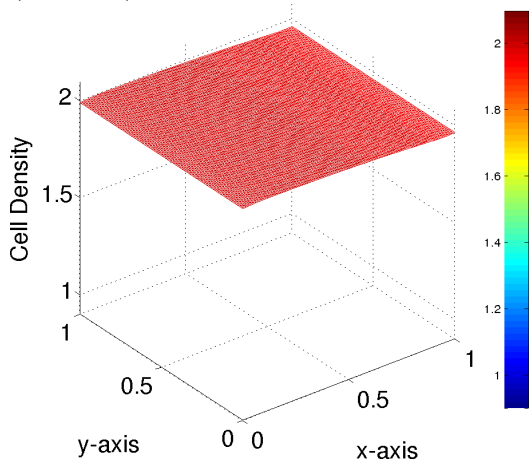

Figure 4.7 Cell density at 600 hours (25 days).

4.2.2 Initial Cell Density Varying Only in x

The results from the constant initial density indicated that any spatial invariance in the initial seeding tends to persist throughout the course of the simulation. Since the perfused flow is directed strictly from $x = 0$ to $x = 1$, the next choice for an initial seeding only varies in the direction of the flow, x (this, and the previous example, also provide a useful check on the numerical code as it is easy to check whether the

cell-seeding remains independent of y for all time). We choose

$$c(x, y, 0) = 1 - \frac{1}{4}(\tanh(5(x - 0.15)) - \tanh(5(x - 0.85))), \tag{4.12}$$

which models cells seeded seeded preferentially near the nutrient inlet and outlet with a slight dip in the middle of the scaffold, as can be seen in Figure 4.8. Figures 4.9-4.11 show the simulation results after ten, fifteen, and twenty-five days. The figures

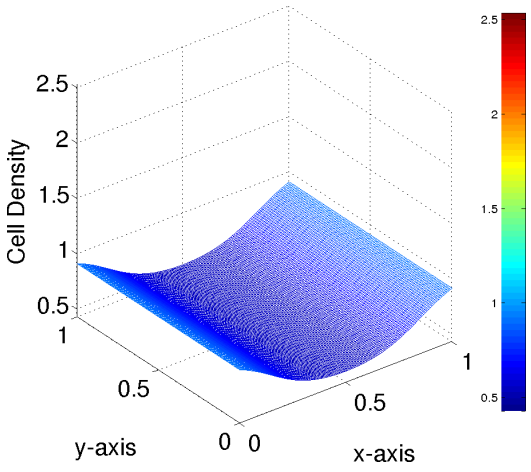

Figure 4.8 Initial cell seeding varying only in x, equation (4.12).

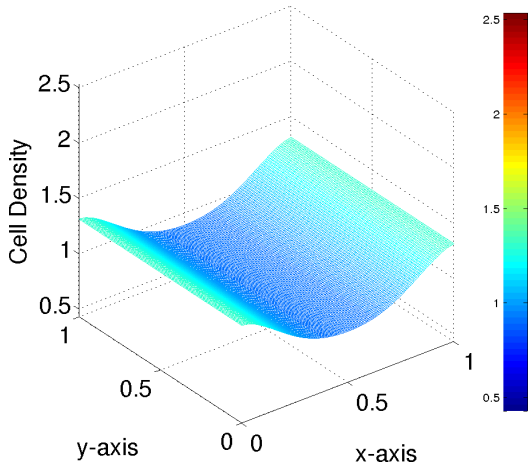

Figure 4.9 Cell density at 240 hours (10 days).

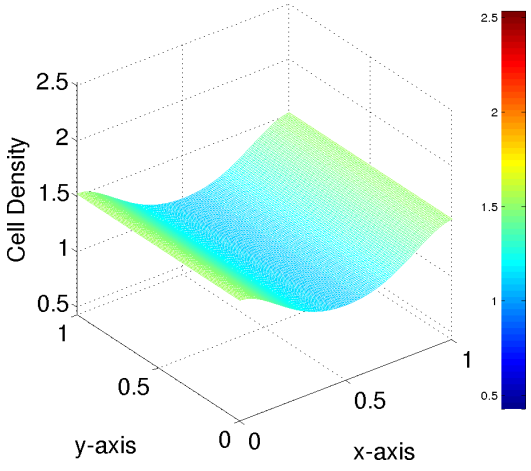

Figure 4.10 Cell density at 360 hours (15 days).

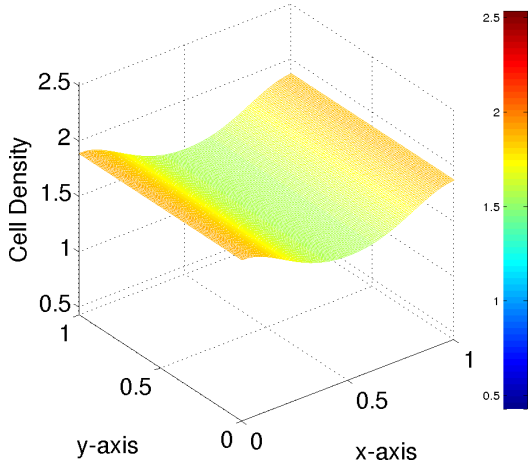

Figure 4.11 Cell density at 600 hours (25 days).

show that the cell density retains the basic shape of the initial seeding for the entire simulation. By the end of the simulation, the seeding density shows tendency to "flatten out" near the inlet and outlet, presumably as it approaches the local carrying capacity; and the density, which initially was lowest near the center seems to be increasing faster there than near $x = 0$ and $x = 1$.

Development of a Steady State The observation of the cell density saturating near the edges $x = 0$ and $x = 1$ leads to the expectation that, after sufficiently long time, the density might reach some sort of spatial "steady state," an assumption which very long time simulations confirm. Figures 4.12 and 4.13 show the scaffold after thirty-five days (4.12) and fifty days (4.13) and while these are not reasonable lengths of time for an experiment of this nature, the results are presented simply to indicate the eventual steady state of the model.

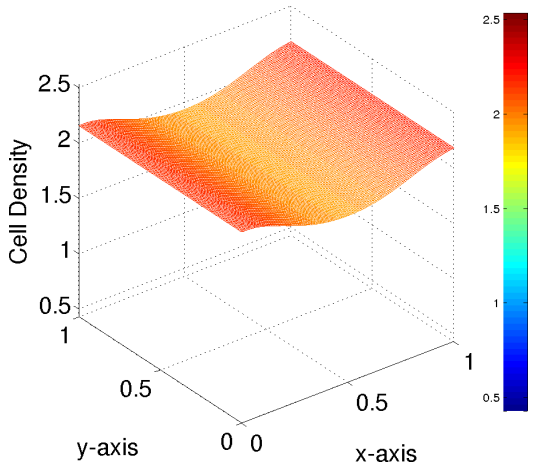

Figure 4.12 Cell density at 840 hours (35 days).

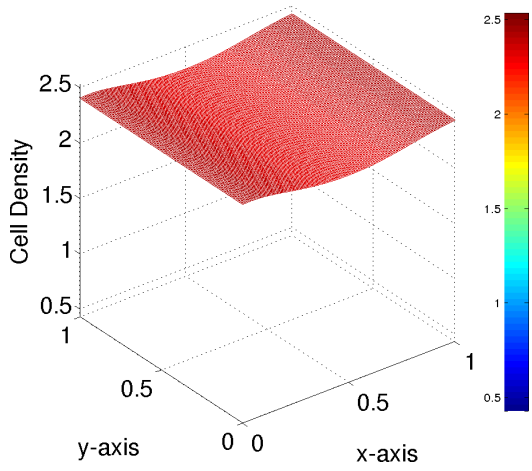

Figure 4.13 Cell density at 1200 hours (50 days).

4.2.3 Initial Cell Density Varying in x and y

Having investigated simple 1D solutions numerically (partly to check our numerical scheme) we now consider some fully 2D initial seedings. Since a fully 2D seeding

induces fully 2D permeability and flow, and hence proliferation rates that vary both in x and y, we anticipate the 2D nature of the cell distribution to persist over time. The results of a simulation with initial cell density

$$c(x, y, 0) = x^3 + y^3, \tag{4.13}$$

(Figure 4.14) are shown in Figures 4.15-4.17. These figures show that the initial cell

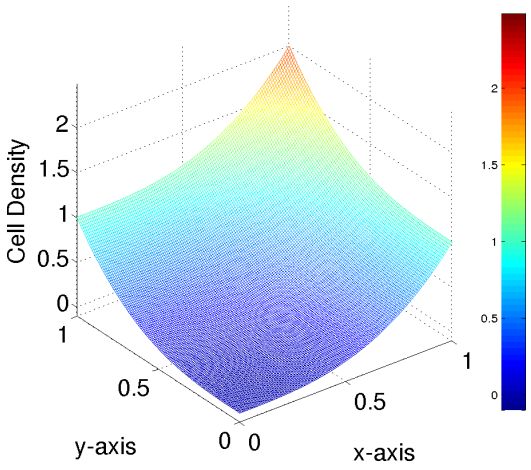

Figure 4.14 Initial cell seeding varying in x and y, equation (4.13).

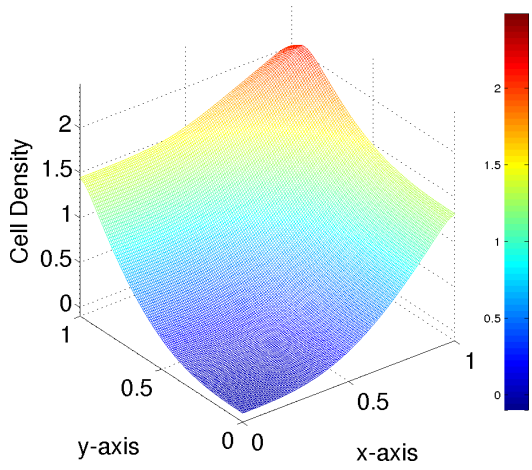

Figure 4.15 Cell density at 240 hours (10 days).

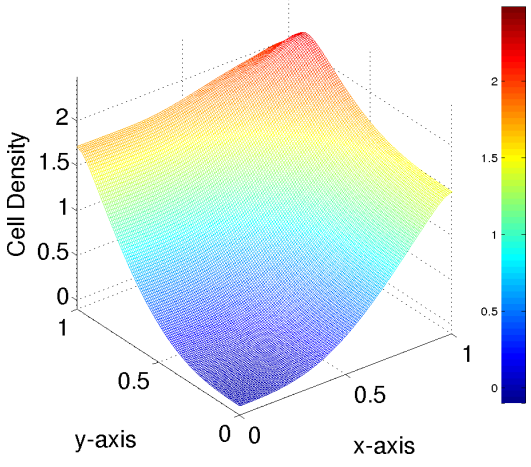

Figure 4.16 Cell density at 360 hours (15 days).

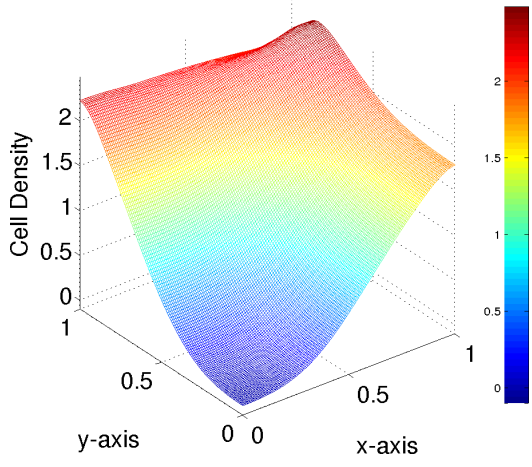

Figure 4.17 Cell density at 600 hours (25 days).

density pattern is relatively well preserved over the course of the simulation, but do

not well reveal the y evolution of the cell density. Figures 4.18-4.21 show contour plots of the same simulation, and they more clearly show the differences in proliferation in the different regions of the scaffold. What is important to notice from this simulation,

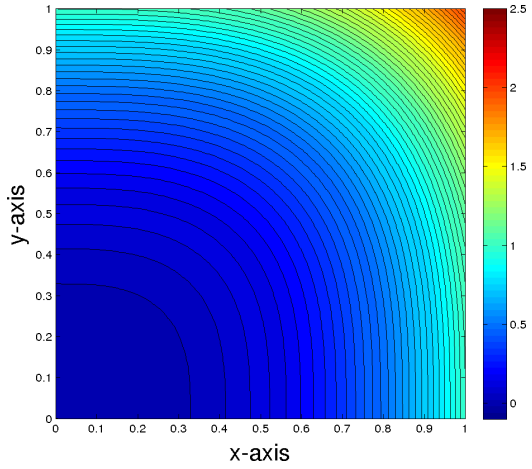

Figure 4.18 Initial cell seeding varying in x and y, equation (4.13).

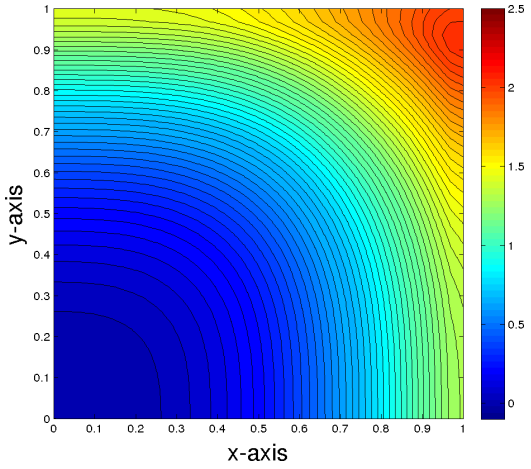

Figure 4.19 Cell density at 240 hours (10 days).

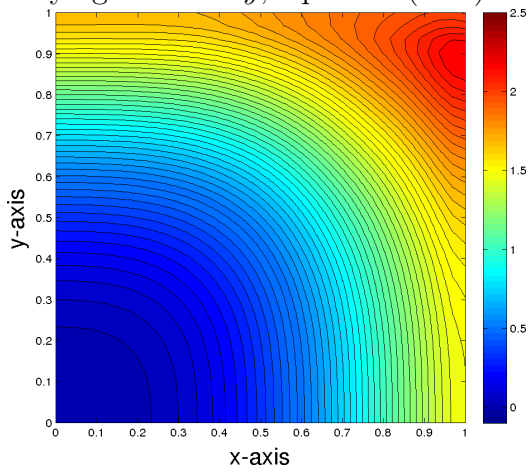

Figure 4.20 Cell density at 360 hours (15 days).

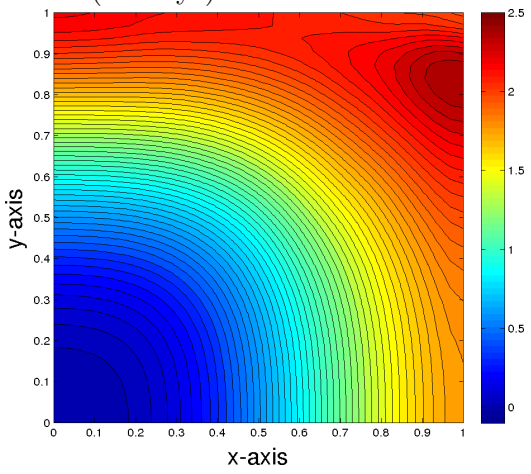

Figure 4.21 Cell density at 600 hours (25 days).

though, is that while the general form of the initial cell density is preserved relatively well, it takes a very long time for cells to appear in regions in which there were little or none in the initial density. Because of the very small coefficient of diffusion of the cells, the density invades new regions very slowly. This is an issue that will be addressed further in Chapter 5, but for now we simply note that all of the simulation

results presented thus far do a fairly good job of retaining the key features of the initial seedings.

Retention of the initial seeding density for the basic model is even evident in more complex initial cell seedings. Figures 4.23-4.25 show the evolution of the cell density with with the initial seeding presented in equation (4.14)

$$c(x, y, 0) = 1 + \frac{1}{2}\sin 6x + \frac{1}{2}\cos 6y, \tag{4.14}$$

seen in Figure 4.22. Here we observe that differently-seeded regions appear to

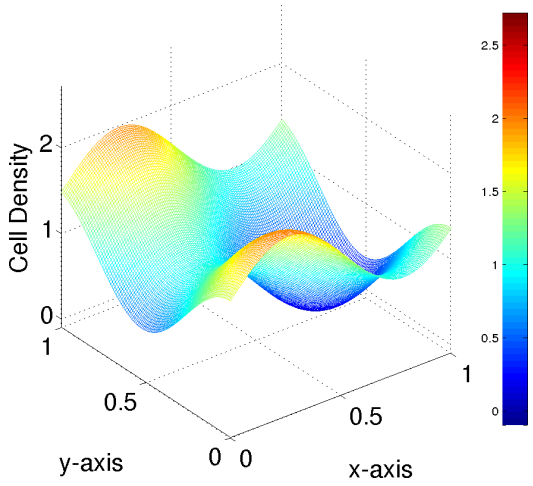

Figure 4.22 Initial cell seeding varying in x and y, equation (4.14).

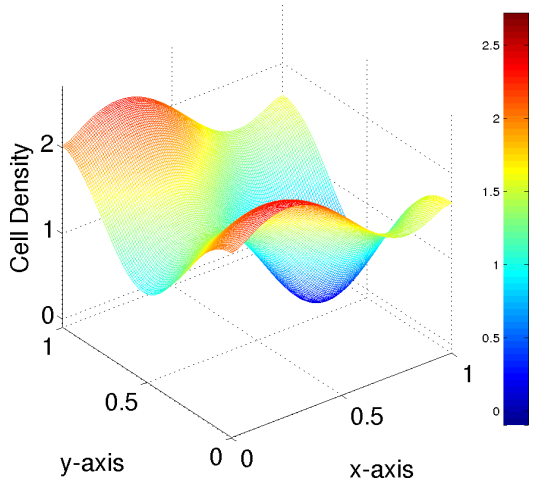

Figure 4.23 Cell density at 240 hours (10 days).

proliferate at different rates. The region region where cell density is initially lowest grows most slowly, whereas the rest of the scaffold seems to be approaching a spatial steady state much faster. This suggests that there may be a threshold of cell density after which the rate of cell proliferation increases.

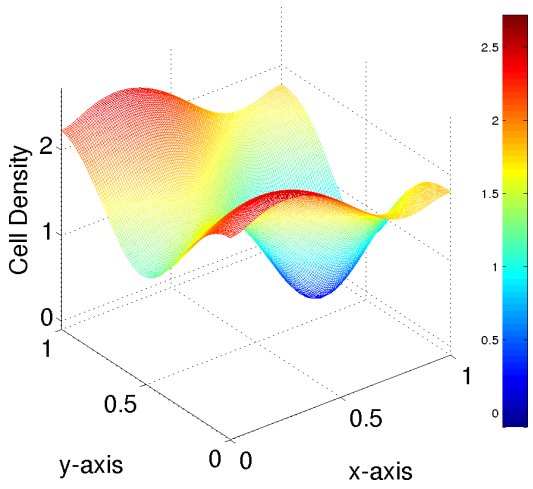

Figure 4.24 Cell density at 360 hours (15 days).

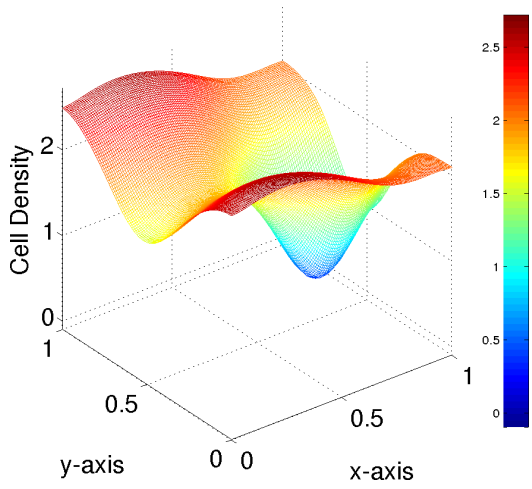

Figure 4.25 Cell density at 600 hours (25 days).

4.2.4 Initial Cell Density Concentrated at Center of Scaffold

All three of the previous simulations indicate very well that the results produced from the model exhibit cell density patterns that are qualitatively similar to the initial seeding pattern over moderate times, but which eventually approach a steady state over very long times. The examples presented so far serve mainly to illustrate how the model behaves as the complexity of the initial seeding increases. The next two simulations use initial conditions that may be more experimentally-relevant. A constant initial seeding, as described in §4.2.1, is assumed to be a favorable choice for uniform final densities, but obtaining a uniform initial density can be difficult. Figures 4.27-4.29 show the evolution of a scaffold on which cells are initially seeded as a central mass, shown in Figure 4.26 and described by equation (4.15)

$$c(x, y, 0) = e^{-20\left(\left(x-\frac{1}{2}\right)^2+\left(y-\frac{1}{2}\right)^2\right)}. \tag{4.15}$$

We notice again that the qualitative shape of the initial seeding density is relatively well-preserved over the course of the simulation. Over a relatively long time the cell density is focused around the center of the scaffold, and it is only after twenty-five

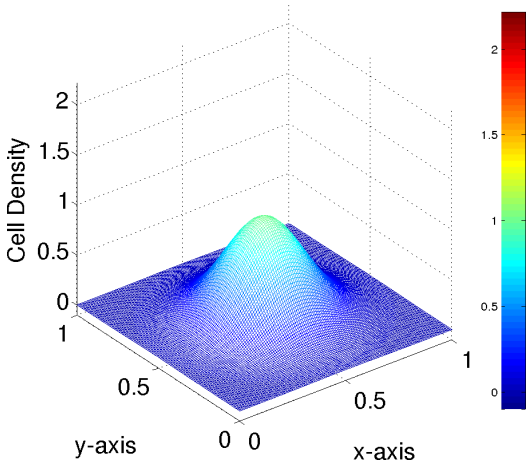

Figure 4.26 Central bump initial cell seeding, equation (4.15).

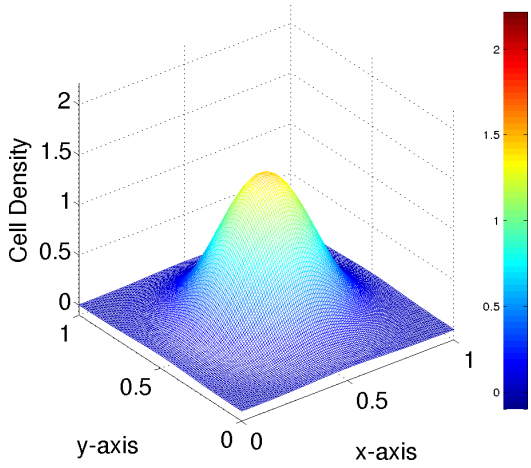

Figure 4.27 Cell density at 240 hours (10 days).

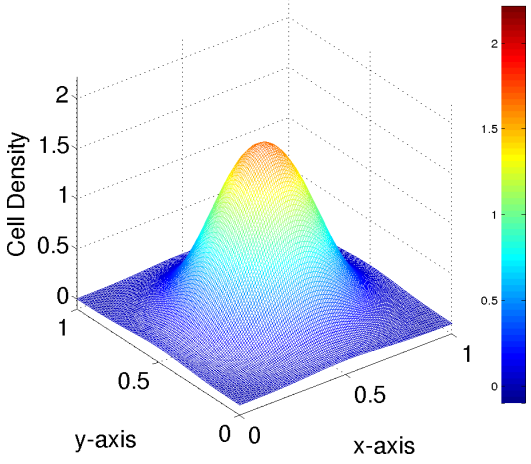

Figure 4.28 Cell density at 360 hours (15 days).

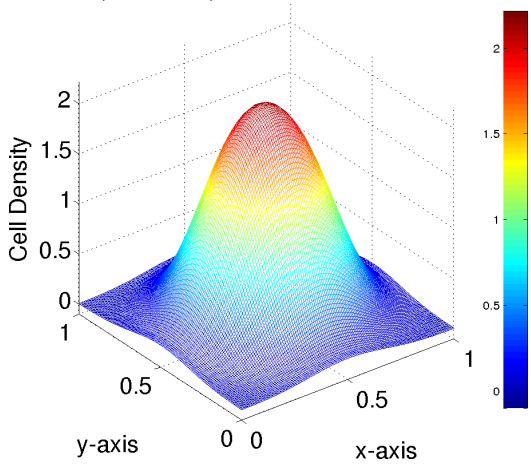

Figure 4.29 Cell density at 600 hours (25 days).

days that cells tend to appear near the boundaries of the scaffold. While the goal of tissue engineering is is often to obtain a relatively uniform final cell density, there may be situations where a small concentrated mass of cells is desired, and this result shows promise that an initial localized mass can hold its form while increasing in overall cell population.

4.2.5 Initial Cell Density Around Periphery of Scaffold

While our results indicate that a constant initial cell density gives the best opportunity to have a relatively spatially constant final cell density, this may not be practical as it may be difficult to achieve a constant initial density. It may be easier to seed cells round the periphery of the scaffold, and hope that diffusion and flow advection (drag) can act to bring cells into the unseeded center. Figure 4.30 shows the initial seeding with cells around the edges of the scaffold, and Figures 4.31-4.33 show the results from this simulation. These results are the first which indicate some true qualitative

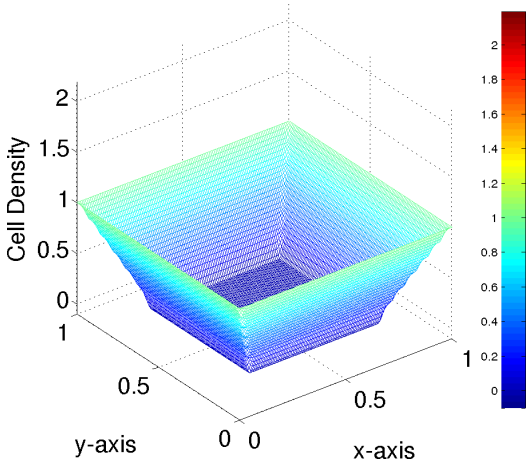

Figure 4.30 Peripheral initial cell seeding.

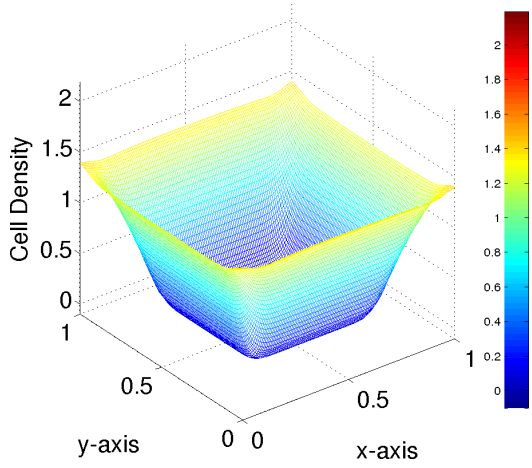

Figure 4.31 Cell density at 240 hours (10 days).

spatial deviation of the final cell distribution from the initial seeding. There is a clear tendency for the cells to proliferate at a higher rate near the inflow $x = 0$, where the nutrient is supplied to the scaffold. It is also important to note that the central region, in which no cells were present initially, is invaded by cells over time and shrinks; but even after twenty-five days there is still a relatively large central region without any cells.

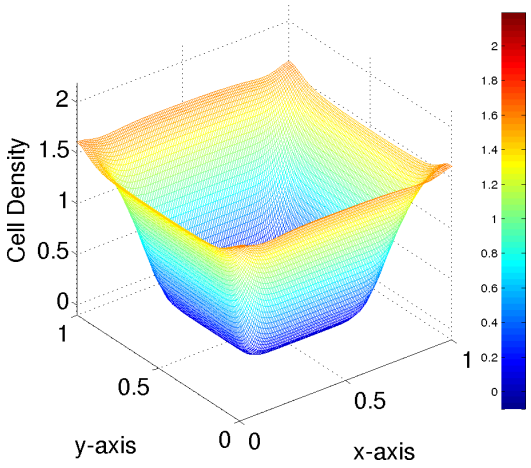

Figure 4.32 Cell density at 360 hours (15 days).

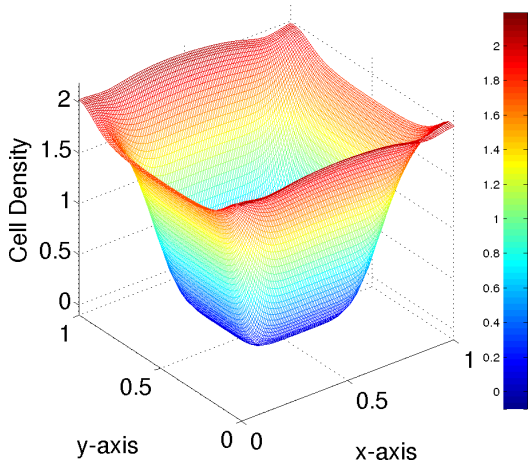

Figure 4.33 Cell density at 600 hours (25 days).

4.2.6 Discussion

In all of the previously presented simulations, we see that when the basic tissue engineering model is simulated, whatever initial density is prescribed is generally retained well over the course of the experiment. One of the goals of this model is to be able to be able to prescribe an initial seeding and then determine what the resulting density will be. In the sense of the model this seems to be an easy feat, but it is not necessarily experimentally feasible. Ultimately we would like to be able to direct cell growth in certain regions to encourage a certain pattern without having to initially "seed in" that pattern (presumably, the greater the spatial complexity of the desired end cell density, the greater the experimental difficulty of creating a similar initial seeding). We investigate one possible method of directing cell proliferation into specific patterns without needing to increase the complexity of the initial cell density in Chapter 5, but before that we address the flexibility and robustness of the model by presenting results while changing the functional forms for equations (3.8)-(3.7).

4.3 Model Robustness and Versatility

One of the main goals of this project is to develop a model that is relatively robust to slight qualitative changes in the forms of constituent functions, yet also versatile so that different modeling scenarios can be easily incorporated. Some of the functional forms that are used were made by choice to satisfy only a few specific properties. For example, the relationship between cell density and permeability ($k(c)$, equation (3.9)) primarily needs to satisfy the conditions that $k(c) \to 1$ as $c \to 0$ and $k(c) \to \infty$ as $c \to \infty$. Two other functional forms play significant roles in the model: the shear stress coefficient which depends on shear stress ($G(\tau_s)$, equation (3.8)), and the carrying capacity function which appears in the cell proliferation/nutrient uptake term ($\hat{c}(n)$, equation (3.6)). In this section, we exhibit the robustness of the model when making small changes to the functional forms that respect the same key conditions. In §4.4 we will also show that the model is easily able to incorporate different modeling scenarios (e.g. higher advective drag) relatively easily, as well. Chapters 5, 6 and 7 explore more significant model extensions.

4.3.1 Permeability and Cell Density

The basic requirements for the functional relationship between cell density c and permeability $k(c)$ were relatively simple: that $k(0) = 1$, and that $k(\infty) = 0$. We chose $k(c) = 1/(1 + c^2)$; here we test the model with several qualitatively similar permeability functions, given in equations (4.16)-(4.19)

$$k_1(c) = e^{0.45c^{-2}}, \tag{4.16}$$

$$k_2(c) = 1 - \tanh\left(\frac{c}{2}\right), \tag{4.17}$$

$$k_3(c) = e^{-0.8c}, \tag{4.18}$$

$$k_4(c) = \operatorname{erfc}\left(\frac{c}{2}\right), \tag{4.19}$$

(see Figure 4.34). We ran simulations for each of the five permeability functions,

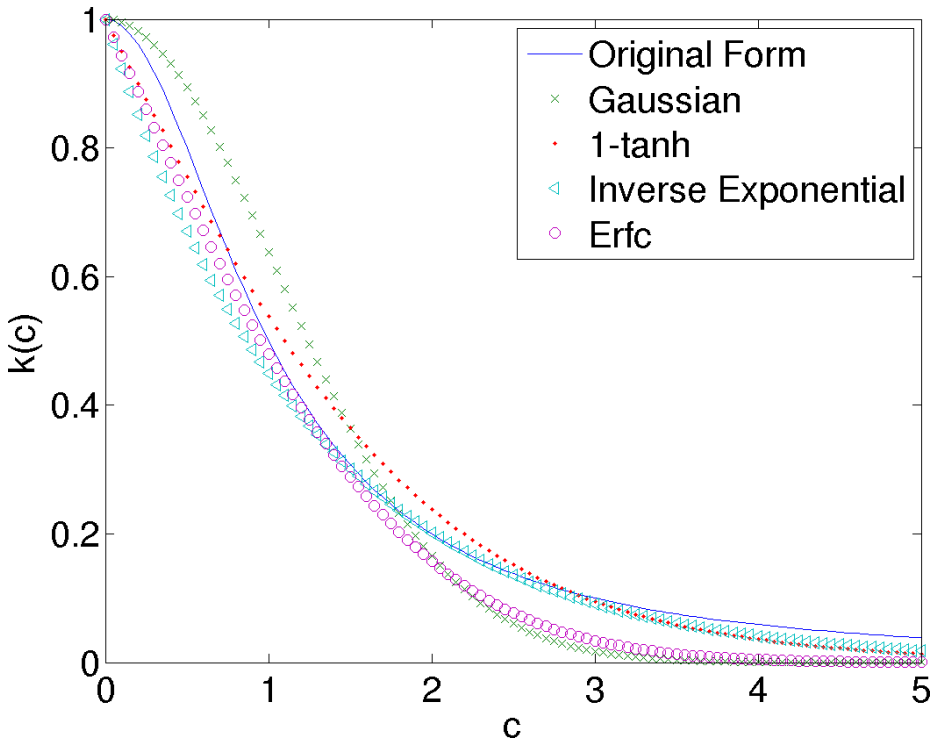

Figure 4.34 Possible functional forms for permeability (equations (4.16)-(4.19)) compared to the original choice.

with other parameters as in the preceding simulations, for the "central bump" initial cell seeding given by equation (4.15). To determine how the results for the permeabilities in equations (4.16)-(4.19) differ from those for the original permeability (equation (3.9)), the maximum of the norm of the difference between each new simulation and the original (normalized by the norm of the original simulation) was calculated at each time step,

$$\frac{\max_{x,y}\|c(x,y,t) - c_i(x,y,t)\|_2}{\max_{x,y}\|c(x,y,t)\|_2}, \tag{4.20}$$

where $c_i(x,y,t),\ i = 1,2,3,4$ are the cell densities for each corresponding permeability functional form. The results, seen in Figure 4.35, indicate that there is less than a 2.5% difference in the results for all of the previously described permeability and

cell density relationships, indicating good robustness of the model to changes in this functional form.

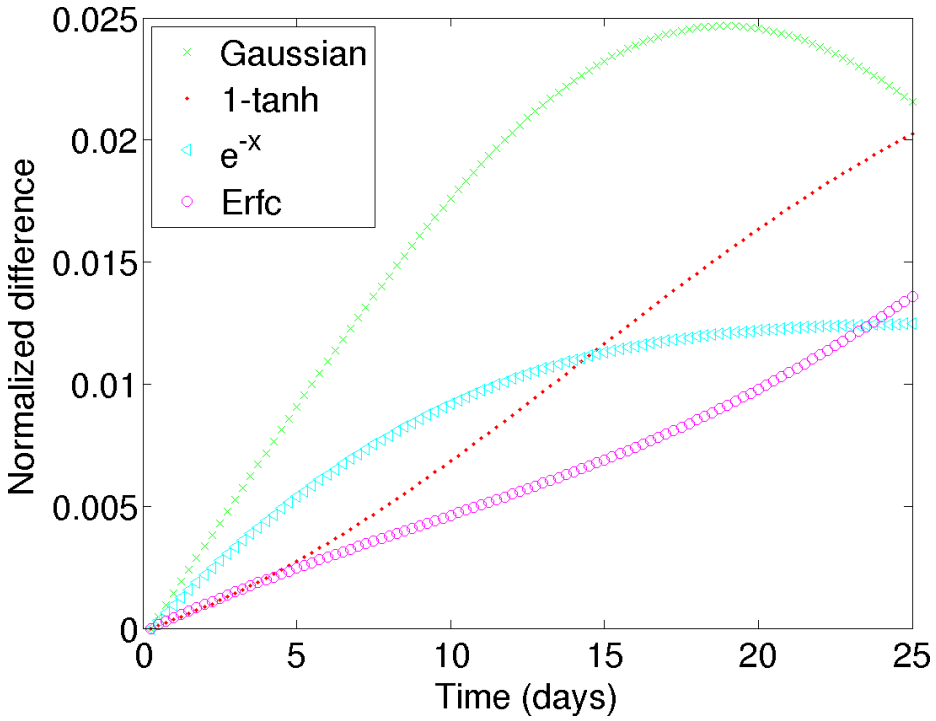

Figure 4.35 Norms of results when considering different functional forms for permeability, equations (4.16)-(4.19) at each time step, as calculated in equation (4.20).

4.3.2 Shear Stress Coefficient

The conditions imposed on our original choice of shear stress coefficient, $G(\tau_s)$, were that it behaves like $\sqrt{\tau_s}$ for small values of τ_s [22] and as $\tau_s \to \infty$, $G(\tau_s) \to 0$. Here we examine the model's robustness to moderate changes in $G(\tau_s)$, incorporating different decay rates as $\tau_s \to 0$ and ∞. The original function choice is $G(\tau_s) = \sqrt{\tau_s}/(1+\tau_s)$

(equation (3.7)); here we investigate different functional forms, given by:

$$G_1(\tau_s) = \frac{5}{2}\left(\frac{\mathrm{erf}(\tau_s)}{1+3\sqrt{\tau_s}}\right), \tag{4.21}$$

$$G_2(\tau_s) = \frac{\sqrt[3]{\tau_s}}{1+\tau_s}, \tag{4.22}$$

$$G_3(\tau_s) = \frac{\tau_s}{1+\tau_s^2}, \tag{4.23}$$

and their comparisons to the original functional form are seen Figure 4.36. We again run simulations for each choice of G with the "central bump" initial cell-seeding of equation (4.15). We can see that while the general forms of the graphs for $G(\tau_s)$ are similar, there is a larger disparity between all of the examples than was seen in the permeability choices tested, Figure 4.34. Because of this we observe in Figure 4.39, as expected, that the norm of the difference calculated as in equation (4.20) is higher than it was for the permeability results, Figure 4.35. The functional form that most closely approximates the original choice, equation (4.21), shows a difference close to 4%, while the other functional forms are closer to 15% difference. These relatively large differences that are observed with equation (4.22) and (4.23) are likely due to the fact that, for each of these choices, the stress function $G(\tau_s)$ is smaller than the control for moderate to large shear stresses, giving suppressed growth as proliferation occurs (with decreased permeability and thus higher shear stresses).

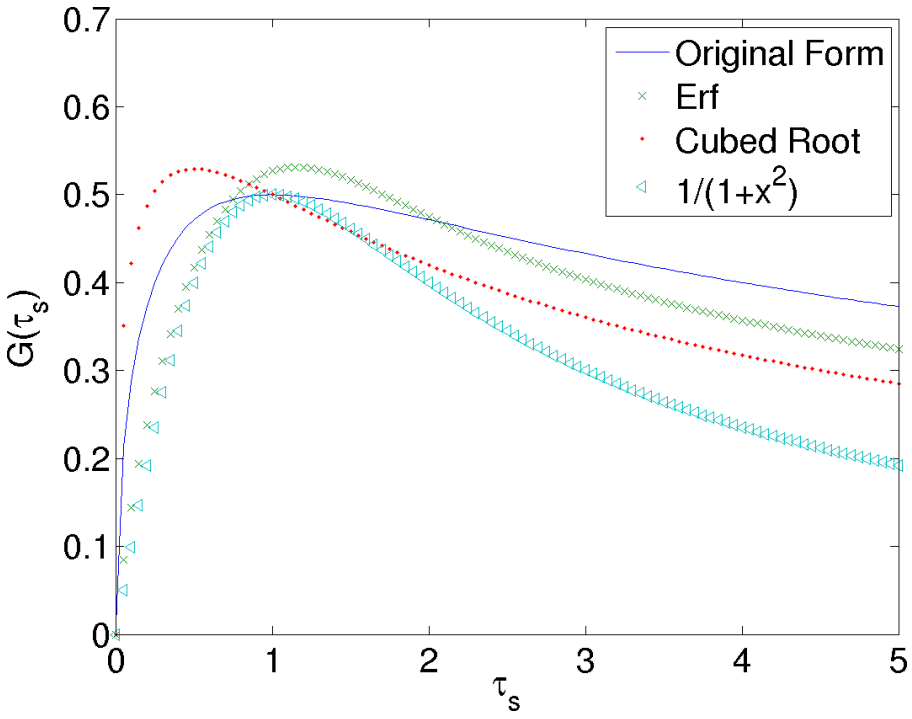

Figure 4.36 Possible functional forms for the shear stress coefficient (equations (4.21)-(4.23)) compared to the original choice.

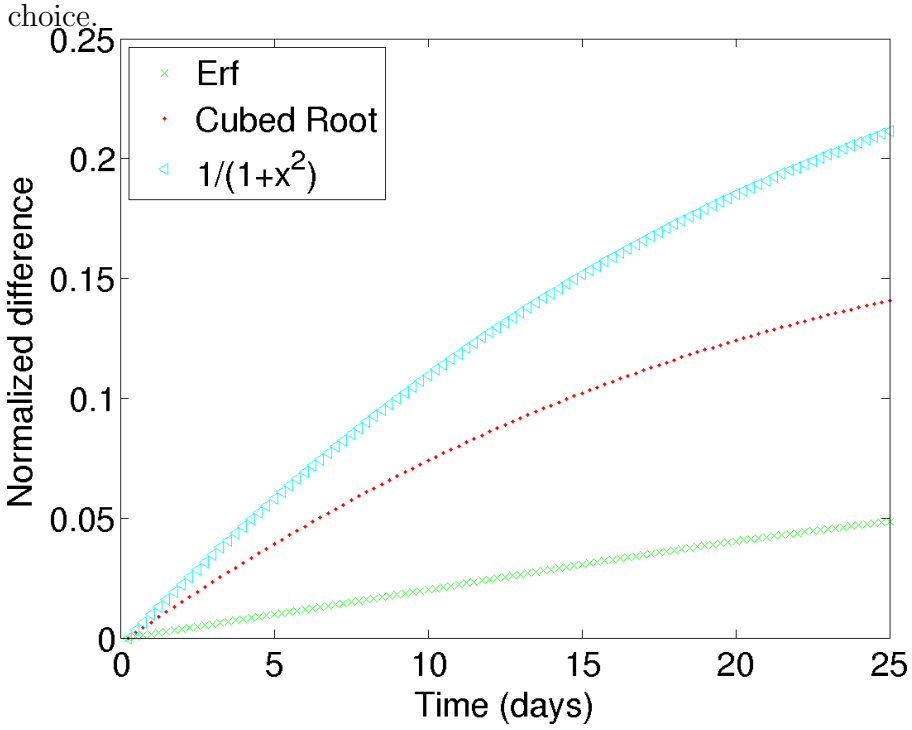

Figure 4.37 Norms of results when considering different functional forms for the shear stress coefficient, equations (4.21)-(4.23) at each time step, as calculated in equation (4.20).

4.3.3 Carrying Capacity Function

Finally, the the principal requirements for the cell density carrying capacity function in terms of local nutrient availability, $\hat{c}(n)$, are that $\hat{c}(n) \to 0$ as $n \to 0$ and $\hat{c}(n) \to 0$ as $n \to \infty$ (nutrient toxic in excess). The original choice of this function is $\hat{c}(n) = \hat{c_0} n/(1+n^2)$ and we see in Figure 2.4 that this functional form also has a relatively slow decay in terms of n. We simulate the model with a further four choices of carrying capacity function, each of which respect the basic requirements:

$$\hat{c}_1(n) = \hat{c_0}\frac{\arctan(1.5n)}{1+n}, \tag{4.24}$$

$$\hat{c}_2(n) = \hat{c_0}\frac{1.2\,\mathrm{erf}(n)}{1+n}, \tag{4.25}$$

$$\hat{c}_3(n) = \hat{c_0}\frac{\sqrt[3]{n}}{1+n}, \tag{4.26}$$

$$\hat{c}_4(n) = \hat{c_0}\frac{\sqrt{n}}{1+n}, \tag{4.27}$$

and their graphs relative to the original functional form choice are shown in Figure 4.38. These chosen functional forms, while qualitatively similar, exhibit increase and decrease rates that differ from the chosen carrying capacity (equation (3.6)). The results of of the simulations (with the "central bump" initial cell-seeding of equation (4.15)), as measured by the differences in total cell density calculated according to equation (4.20) are summarized in Figure 4.39. We observe that the choice (4.26) provides the largest deviation from the results of the original model; this is to be expected since Figure 4.39 reveals this function to have the largest net deviation from the chosen carrying capacity, equation (3.6). Nonetheless, even here the difference is always less than 1.5%.

Discussion The simulations of §4.3.1, 4.3.2, and 4.3.3 clearly demonstrate the robustness of the model to qualitative changes in the behavior of the constituent functions, and also its flexibility in terms of ease of adaptation to different hypotheses. When a particular functional form is changed by only a small amount, only small

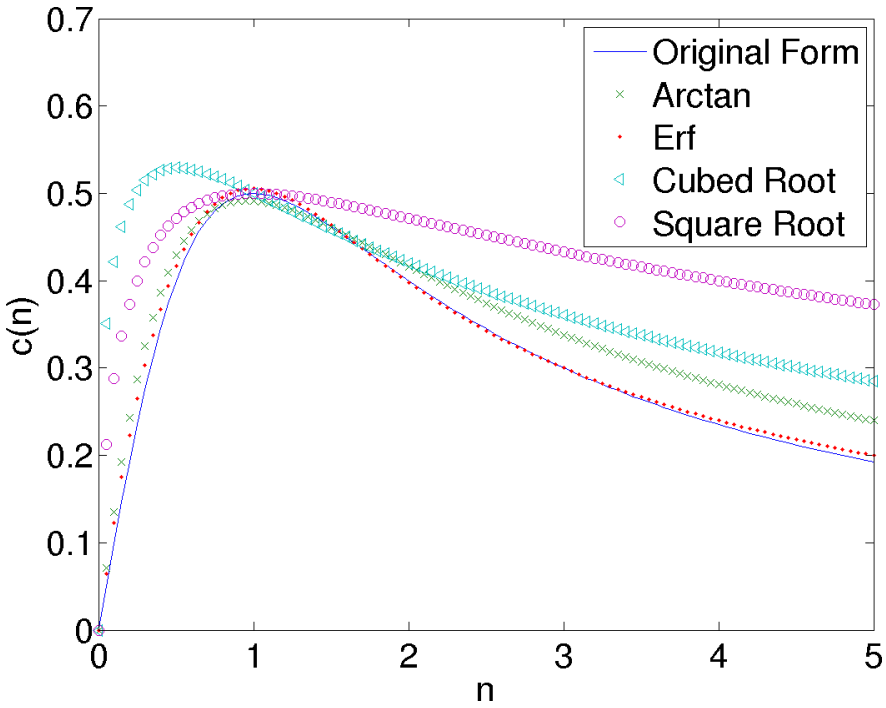

Figure 4.38 Possible functional forms for the carrying capacity (equations (4.24)-(4.27)) compared to the original choice.

changes in the results are seen. If future research suggests that alternative functional relations are more appropriate, then the model is easily changed to incorporate the new information.

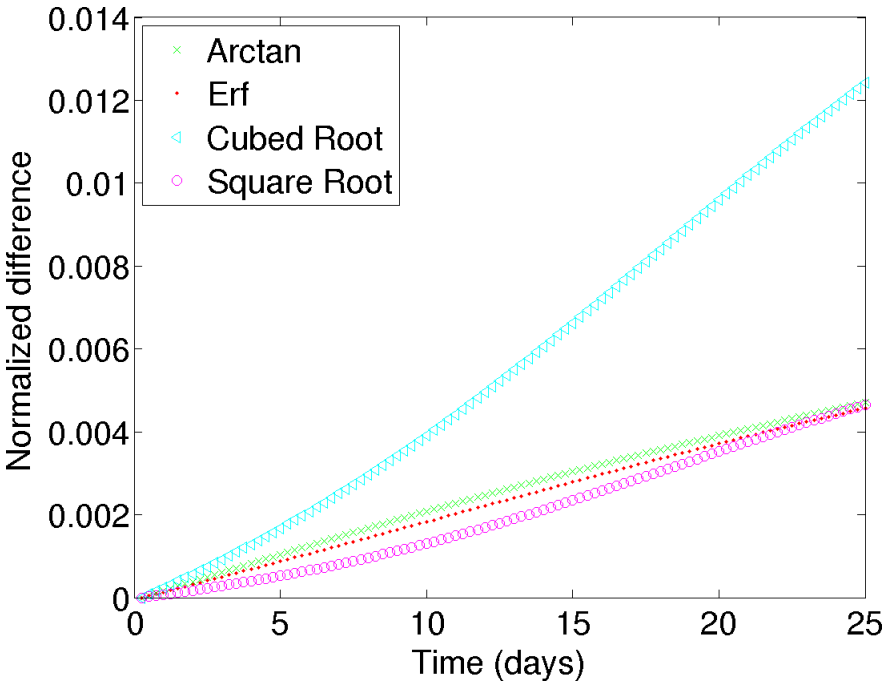

Figure 4.39 Norms of results when considering different functional forms for the carrying capacity function, equations (4.24)-(4.27) at each time step, as calculated in equation (4.20).

4.4 Effects of Changing Parameter Values

The final numerical investigation of the basic model is the effect of changing parameter values such as the death rate, ν, and the nutrient uptake rate, θ. Many of the parameter values are inherently variable, depending as they do on the type of nutrient, cell, and scaffold used. In this section, we change the values of parameters to illustrate how the model outcome (again measured by the total cell yield over time) changes in response. In particular, we investigate the effect of changing the constant cell death rate ν, the cellular advective drag coefficient δ/ϵ, the nutrient uptake rate θ, and the cellular diffusion coefficient D_c. We will use initial cell seedings from previous simulations, giving just one example for each effect analyzed. The chosen initial cell seeding for each example is that which best illustrates the effect of the parameter change.

4.4.1 Death Rate

The dimensionless death rate, as first presented in Table 3.4, is $\nu = 0.1435$. Simulations were run with the initial cell seeding concentrated in the center of the scaffold as prescribed by equation (4.15), with all other parameters unchanged from the introductory simulations. Three more simulations were run with the death rate increasing by a factor of 1.5 to values $\nu = 0.21525,\ 0.322875,$ and 0.4843125. As the death rate increases a general reduction in cell density is naturally expected. The results are presented in Figures 4.40-4.43 after ten days and in Figures 4.44-4.47 after twenty-five days.

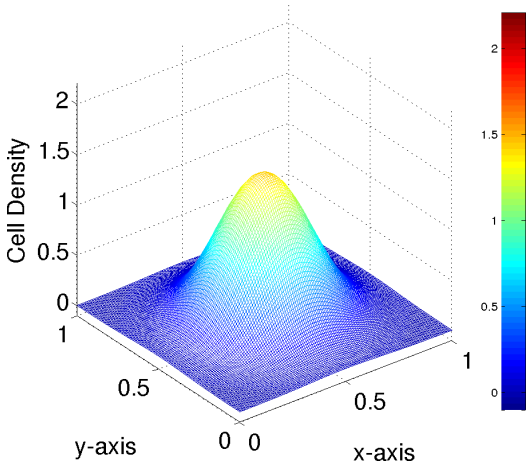

Figure 4.40 Cell density at 240 hours (10 days) with $\nu = 0.1435$.

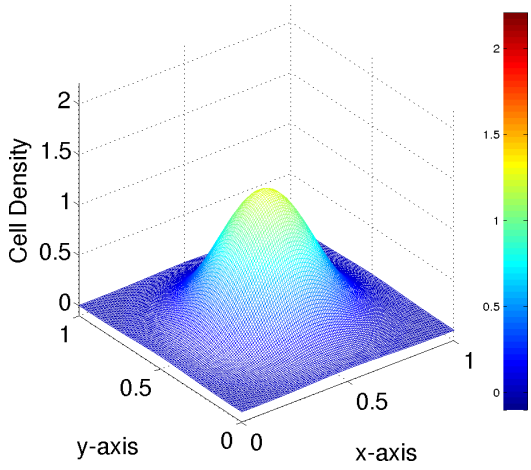

Figure 4.41 Cell density at 240 hours (10 days) with $\nu = 0.21525$.

The results clearly demonstrate that even a relatively small increase in the death rate greatly affects the cell density in an adverse way. This is even more evident when looking at the total population in the scaffold over the course of the experiment, Figure 4.48. This figure confirms what one might suspect from Figures 4.43 and 4.47: with the largest chosen death rate, $\nu = 0.484$, proliferation is suppressed altogether and the cell population is slowly moving towards extinction. This indicates the existence of a threshold value for ν, above which a population is not viable.

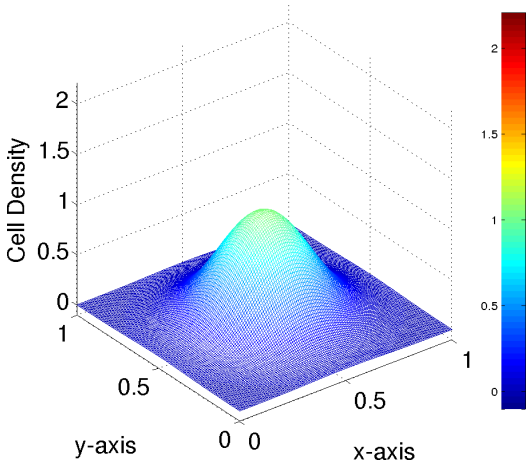

Figure 4.42 Cell density at 240 hours (10 days) with $\nu = 0.322875$.

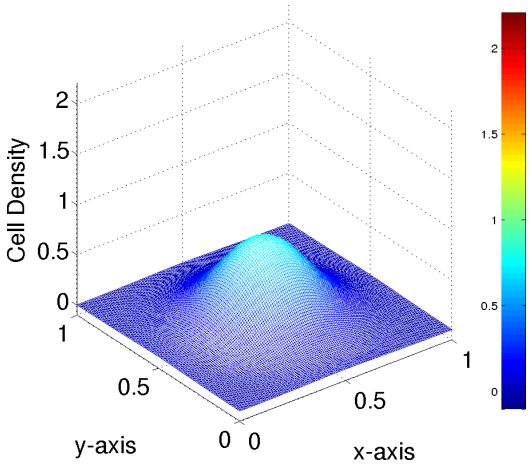

Figure 4.43 Cell density at 240 hours (10 days) with $\nu = 0.4843125$.

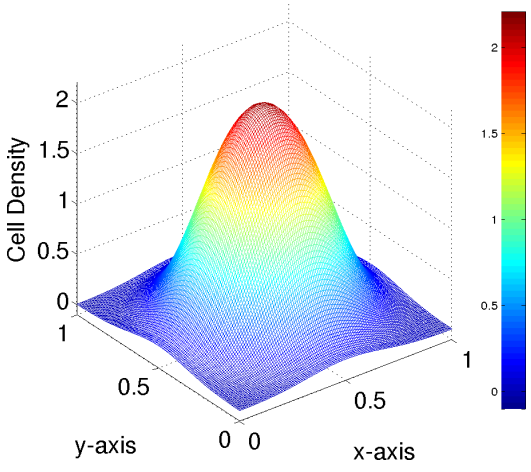

Figure 4.44 Cell density at 600 hours (25 days) with $\nu = 0.1435$.

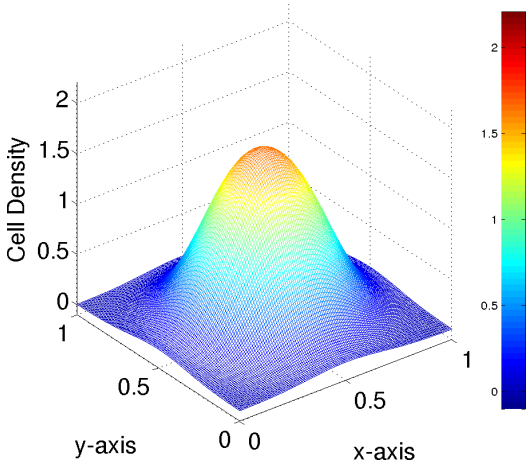

Figure 4.45 Cell density at 600 hours (25 days) with $\nu = 0.21525$.

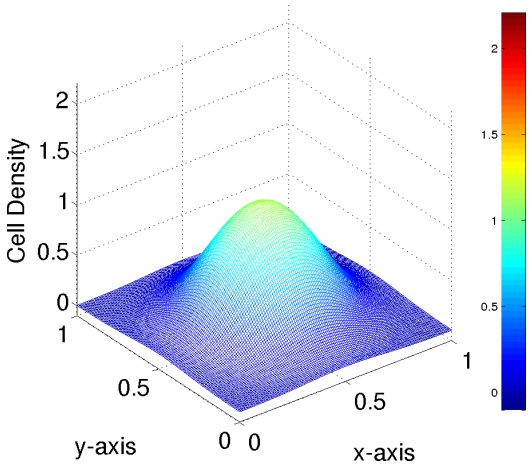

Figure 4.46 Cell density at 600 hours (25 days) with $\nu = 0.322875$.

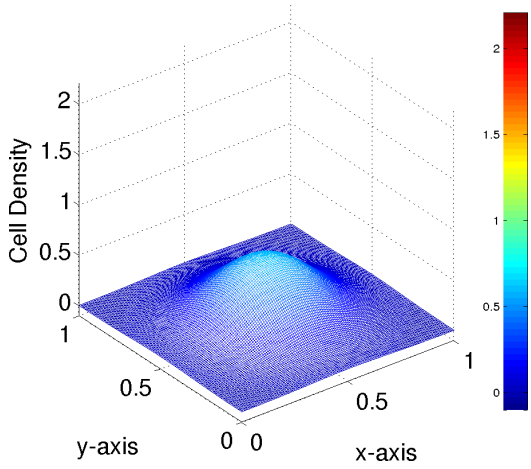

Figure 4.47 Cell density at 600 hours (25 days) with $\nu = 0.4843125$.

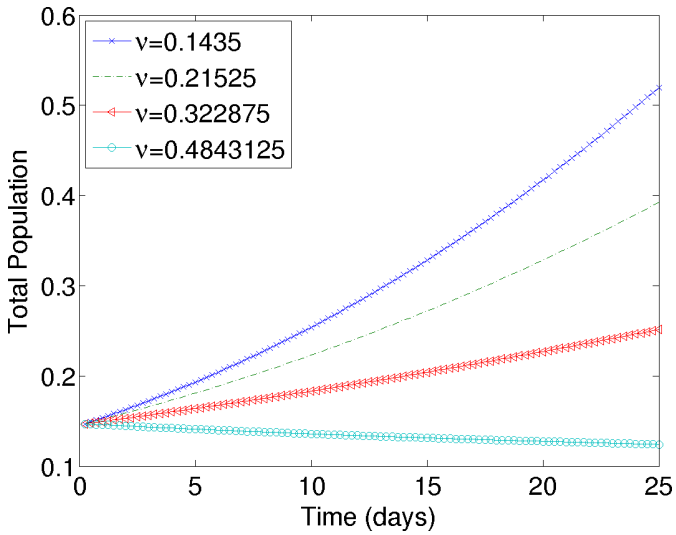

Figure 4.48 Total cell population in the scaffold for the four different death rates, ν.

4.4.2 Cell Advective Drag Coefficient

The dimensionless advective drag coefficient is calculated as δ/ϵ, and using values from Table 3.4 it is set to be $\delta/\epsilon = 10^{-5}$ in the original simulations. We illustrate the effect of changing this parameter using the "peripheral" cell seeding, with all other parameters again unchanged from the introductory simulations. In addition to the simulation presented earlier in Figures 4.30-4.33, we run three additional simulations where the coefficient δ/ϵ increases by an order of magnitude each time to $\delta/\epsilon = 10^{-4}$, 10^{-3}, and 10^{-2}. The results are presented in Figures 4.49-4.52 after ten days and in Figures 4.53-4.56 after twenty-five days.

As the advective drag coefficient is increased, the cell density is expected to shift from being relatively even throughout the scaffold for $\delta/\epsilon = 10^{-5}$ to being weighted toward the outlet at $x = 1$. Interestingly, the effect of increasing the advective

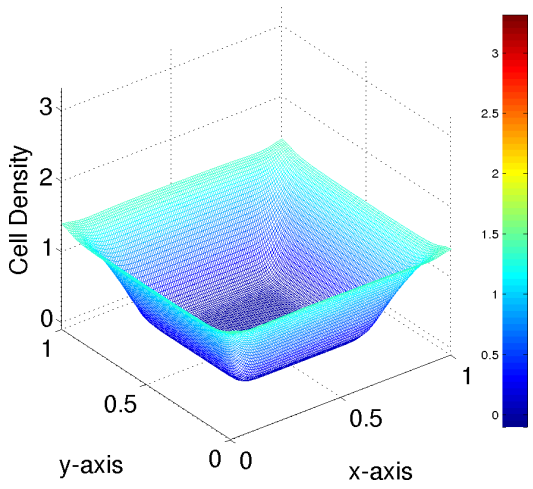

Figure 4.49 Cell density at 240 hours (10 days) with $\delta/\epsilon = 10^{-5}$.

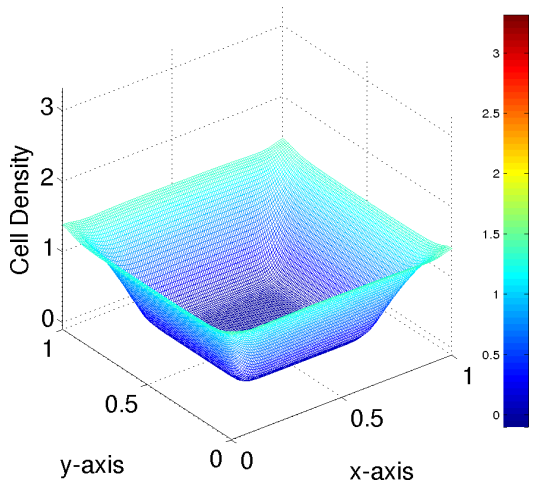

Figure 4.50 Cell density at 240 hours (10 days) with $\delta/\epsilon = 10^{-4}$.

drag was not as drastic as was originally expected until the drag was increased to the final value of $\delta/\epsilon = 10^{-2}$. There is a noticeable difference in the cell densities in Figures 4.53-4.55 in the sense that there is a slightly obvious down tick in density near the inlet and a slight up tick in density near the outlet. The most significant difference

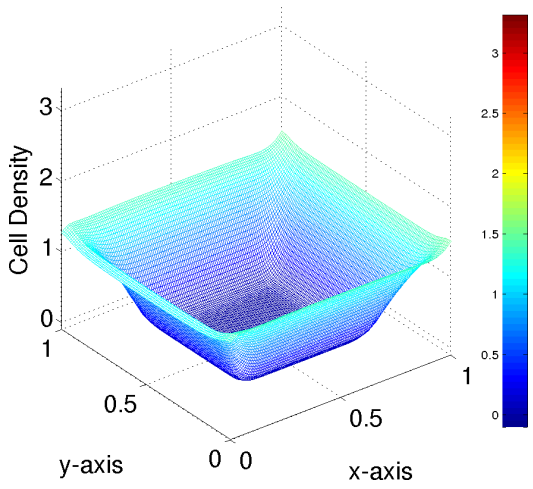

Figure 4.51 Cell density at 240 hours (10 days) with $\delta/\epsilon = 10^{-3}$.

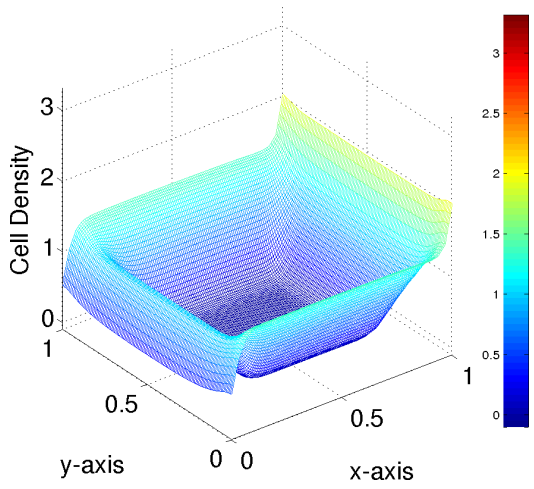

Figure 4.52 Cell density at 240 hours (10 days) with $\delta/\epsilon = 10^{-2}$.

occurs at the final value ($\delta/\epsilon = 10^{-2}$), though, where the drop in density near $x = 0$ and the rise in density near $x = 1$ is drastic. This result is somewhat misleading, though, in that the model assumes the boundary $x = 1$ is permeable to flow but impermeable to cells; realistically, cells experiencing this high level of drag would likely be flushed from the scaffold with the flow due to their weak adherence. Another

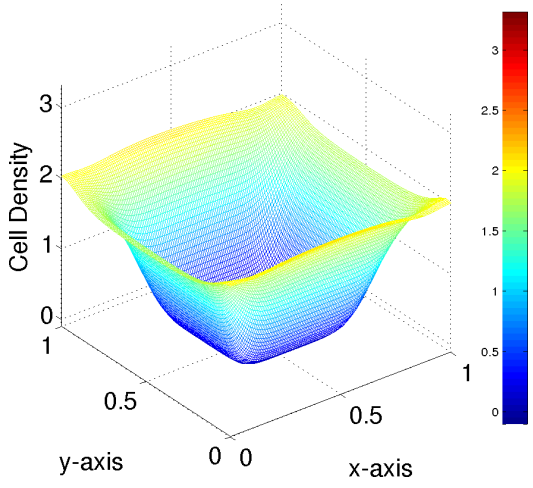

Figure 4.53 Cell density at 600 hours (25 days) with $\delta/\epsilon = 10^{-5}$.

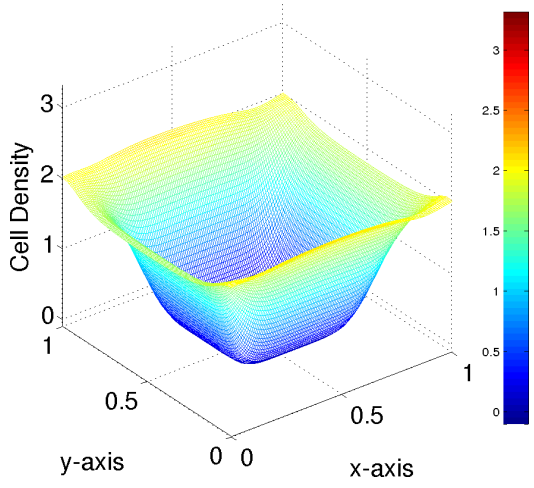

Figure 4.54 Cell density at 600 hours (25 days) with $\delta/\epsilon = 10^{-4}$.

interesting result is that while the cell density distribution can vary quite significantly,

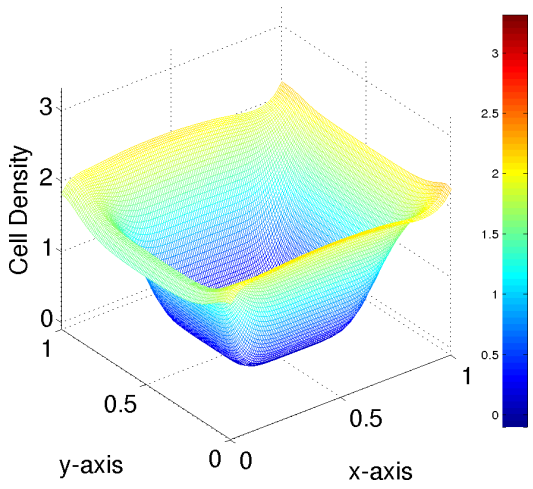

Figure 4.55 Cell density at 600 hours (25 days) with $\delta/\epsilon = 10^{-3}$.

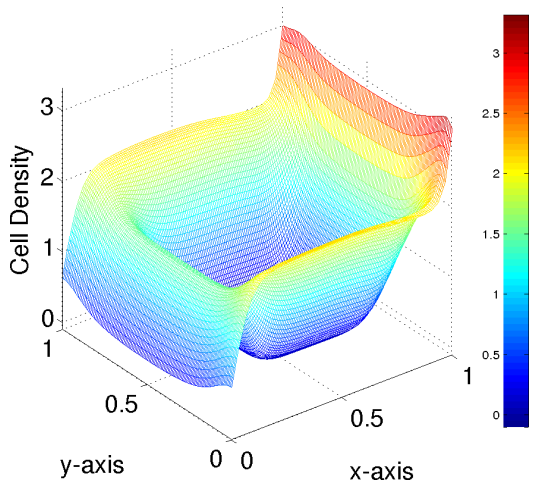

Figure 4.56 Cell density at 600 hours (25 days) with $\delta/\epsilon = 10^{-2}$.

the total cell population is almost unaffected by the change in the advective drag coefficient, as can be seen in Figure 4.57. We might expect that as cellular adhesion is reduced the proliferation decreases, which is not something that is captured by this model. These results are not necessarily indicative of a shortcoming of the model, but rather reflect the fact that 10^{-2} is an unrealistically large value of the advective drag coefficient. Nonetheless, the results are instructive and we include them for completeness.

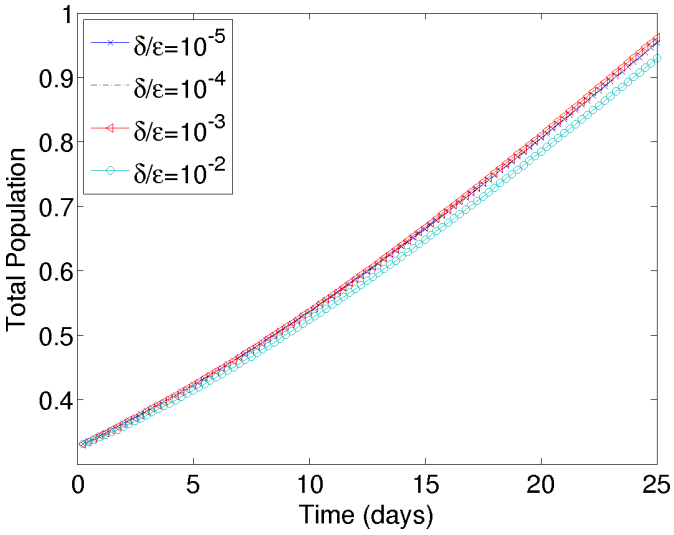

Figure 4.57 Total cell population in the scaffold for the four different advective drag coefficients, δ/ϵ.

4.4.3 Cellular Diffusion Coefficient

The dimensionless cellular diffusion coefficient presented in Table 3.4 has a value of $D_c = 4.32 \times 10^{-4}$. Results from simulations testing the effect of changing the diffusion coefficient are most noticeable with the "peripheral" initial cell seeding, again with all other parameters unchanged from the introductory simulations. The values of the diffusion coefficient tested are: $10D_c = 4.32 \times 10^{-3}$, $25D_c = 1.08 \times 10^{-2}$, and $40D_c = 1.728 \times 10^{-2}$. The results are presented in Figures 4.58-4.61 after ten days and in Figures 4.62-4.65 after twenty-five days. After only ten days, the cells have invaded the central region of the scaffold significantly even when the diffusion coefficient is increased by one order of magnitude. Though it is clear that, with a larger diffusion coefficient proliferation occurs much faster in the center of the scaffold, it is not immediately evident whether an increased rate of total proliferation accompanies this. While the cell density in the central region is higher, the densities near the periphery of the scaffold have decreased as cells have diffused from these regions. At the highest level of cellular diffusion the population is even close to a relative

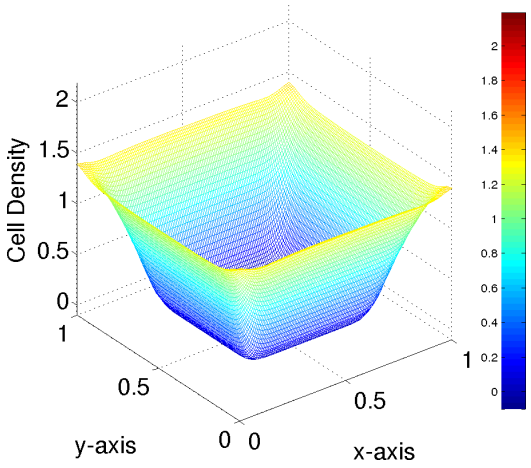

Figure 4.58 Cell density at 240 hours (10 days) with $D_c = 4.32 \times 10^{-4}$.

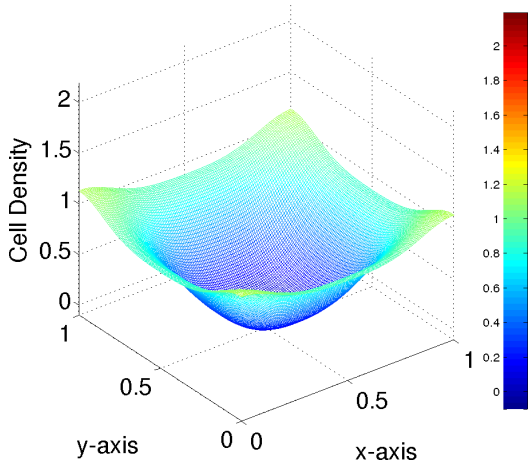

Figure 4.59 Cell density at 240 hours (10 days) with $D_c = 4.32 \times 10^{-3}$.

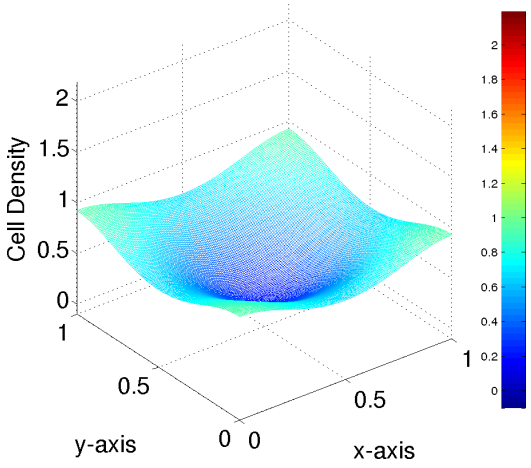

Figure 4.60 Cell density at 240 hours (10 days) with $D_c = 1.08 \times 10^{-2}$.

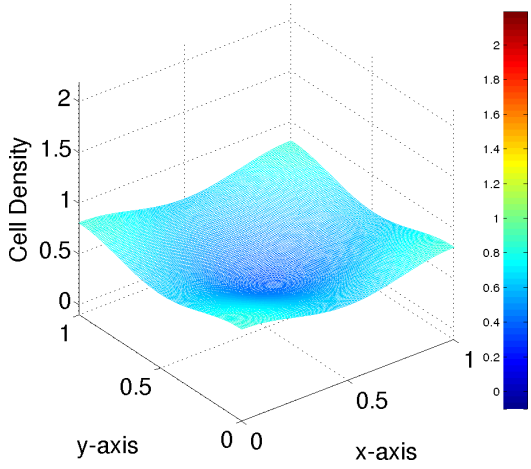

Figure 4.61 Cell density at 240 hours (10 days) with $D_c = 1.728 \times 10^{-2}$.

spatial steady state after only ten days. After twenty-five days the effects are even more apparent. The cell densities resulting from the highest two diffusion coefficients are very similar, and the density due to increasing the diffusion coefficient by one order of magnitude differs greatly from that for the original parameter values. Any spatial variation from the inlet to the outlet due to the fluid flow is nearly lost, as the dominant effect is now diffusion of cells from areas of high concentration to those with

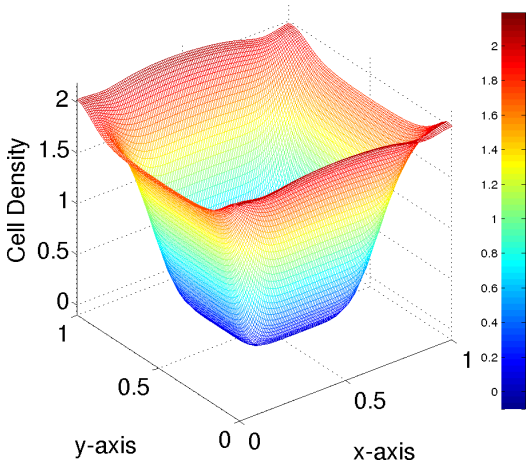

Figure 4.62 Cell density at 600 hours (25 days) with $D_c = 4.32 \times 10^{-4}$.

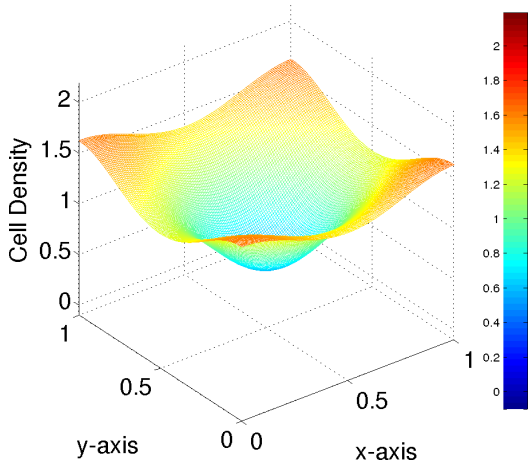

Figure 4.63 Cell density at 600 hours (25 days) with $D_c = 4.32 \times 10^{-3}$.

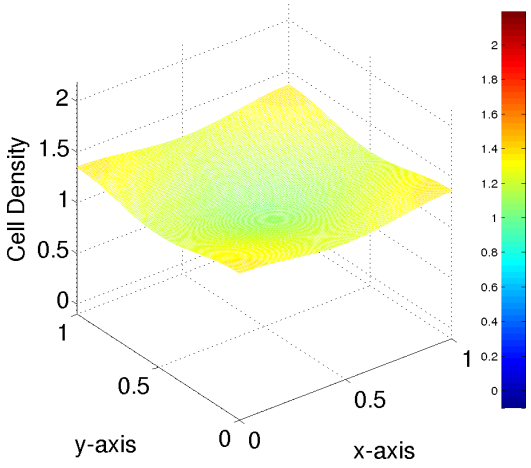

Figure 4.64 Cell density at 600 hours (25 days) with $D_c = 1.08 \times 10^{-2}$.

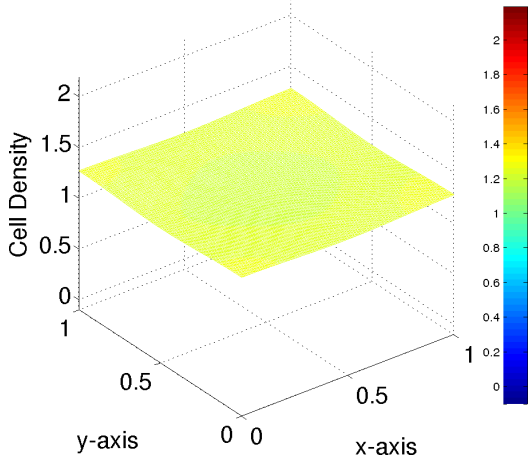

Figure 4.65 Cell density at 600 hours (25 days) with $D_c = 1.728 \times 10^{-2}$.

lower concentrations. Figure 4.66 indicates that increasing the diffusion coefficient, at least for this initial seeding, slightly increases total proliferation. This is due to cells invading the empty space faster and being able to proliferate at an earlier time than in the original simulation. Again, while instructive, these results for larger diffusion coefficients are not necessarily experimentally-relevant. Experimentalists would likely choose to work with scaffolds whose pore sizes complemented the sizes of the cells,

thus reducing the cellular diffusion coefficient to something more in line with our original chosen value.

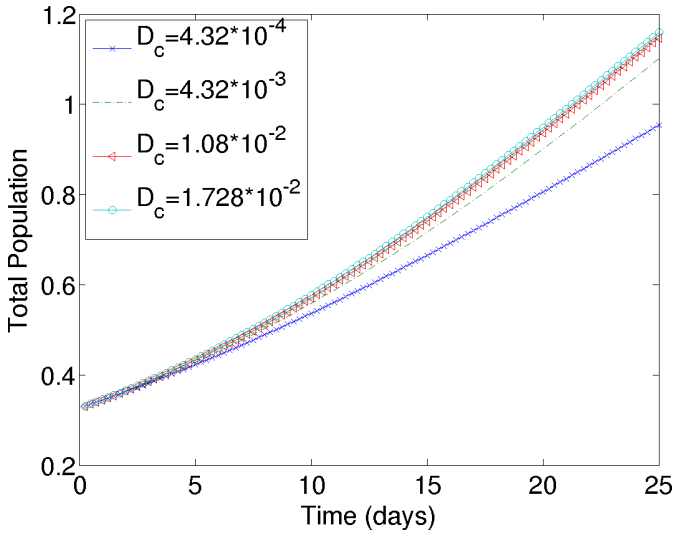

Figure 4.66 Total cell population in the scaffold for the four different cell diffusion coefficients, D_c.

4.4.4 Nutrient Uptake Rate

The default value of the dimensionless rate of nutrient uptake is $\theta = 0.744$, first presented in Table 3.4. We carried out simulations at different uptake rates for all of the previously-mentioned initial cell seedings, but the most interesting were those with the initial cell density varying in both x and y (presented in equation (4.13) in §4.2.3), hence we show only these. In each subsequent simulation, the rate of nutrient uptake was doubled, giving values of $\theta = 1.488,\ 2.976,$ and 5.952 with all other parameters the same as in the original simulations. We anticipate a general increase in proliferation as theta increases: since cells consume nutrient faster, they grow faster. The results are presented in Figures 4.67-4.70 after ten days and in Figures 4.71-4.74 after twenty-five days. The results after ten days suggest an interesting effect, that being a tendency to higher proliferation near the inlet of the

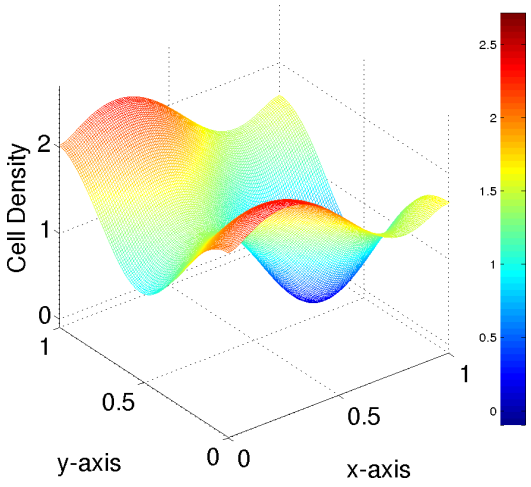

Figure 4.67 Cell density at 240 hours (10 days) with $\theta = 0.744$.

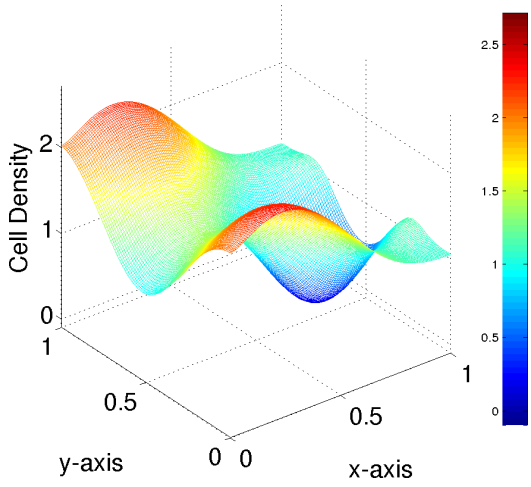

Figure 4.68 Cell density at 240 hours (10 days) with $\theta = 1.488$.

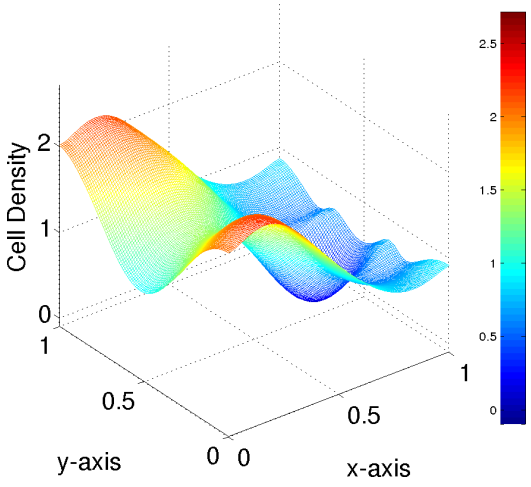

Figure 4.69 Cell density at 240 hours (10 days) with $\theta = 2.976$.

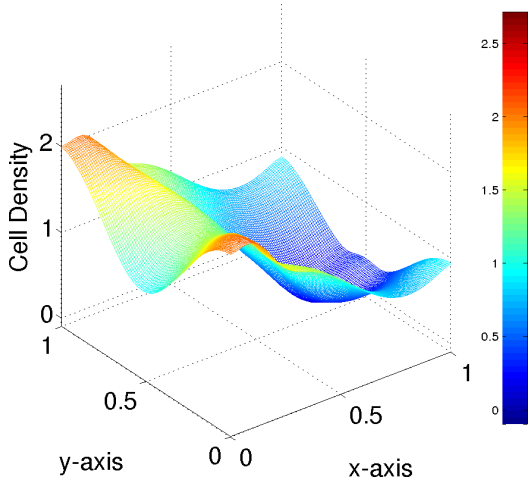

Figure 4.70 Cell density at 240 hours (10 days) with $\theta = 5.952$.

scaffold. The first two simulations ($\theta = 0.744$ and $\theta = 1.488$) show that the form of the initial seeding is held relatively well, whereas the latter two simulations ($\theta = 2.976$ and $\theta = 5.952$) seem to indicate that the form of the initial cell density is becoming somewhat lost: the high rate of nutrient uptake means that cells near the inlet that are exposed to the fresh nutrient take it up quickly, depleting the levels available for cells downstream towards the outlet. This effect is even more pronounced after

twenty-five days, even with the rate simply doubled from the original simulation (Figure 4.72). The initial cell seeding form is still noticeable in this simulation, but further doubling (Figures 4.71-4.74) indicates a near complete loss of the initial seeding form. Figure 4.75 compares the total cell populations over time for each value of the nutrient uptake coefficient. Somewhat counter-intuitively, the total cell population decreases as the nutrient uptake coefficient increases: the enhanced proliferation at the inlet leaves the downstream cells so depleted of nutrient that proliferation is considerably suppressed, to such an extent that the enhanced upstream proliferation cannot compensate.

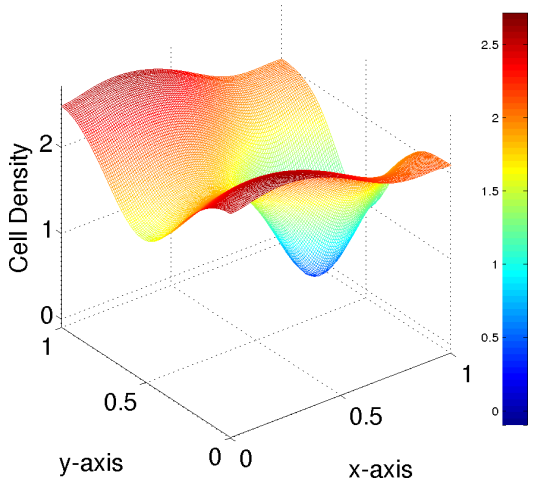

Figure 4.71 Cell density at 600 hours (25 days) with $\theta = 0.744$.

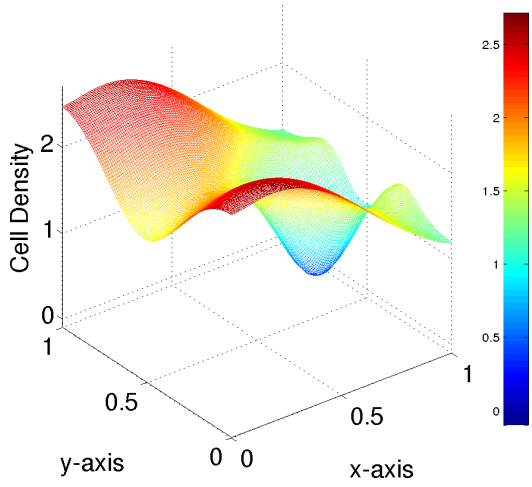

Figure 4.72 Cell density at 600 hours (25 days) with $\theta = 1.488$.

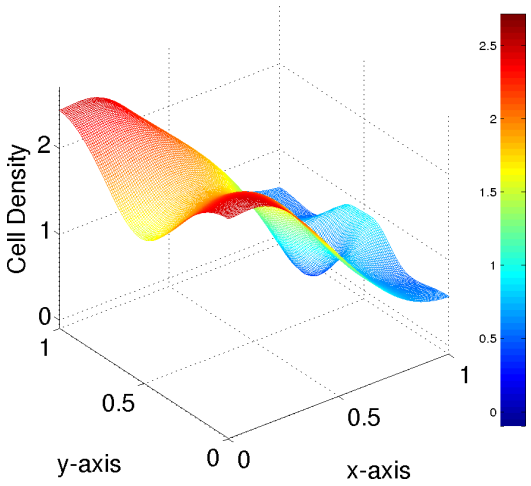

Figure 4.73 Cell density at 600 hours (25 days) with $\theta = 2.976$.

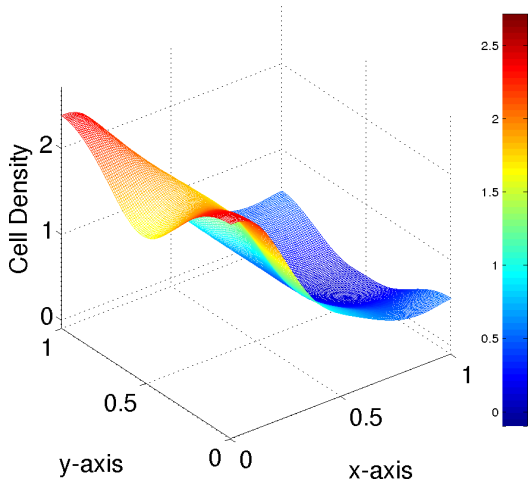

Figure 4.74 Cell density at 600 hours (25 days) with $\theta = 5.952$.

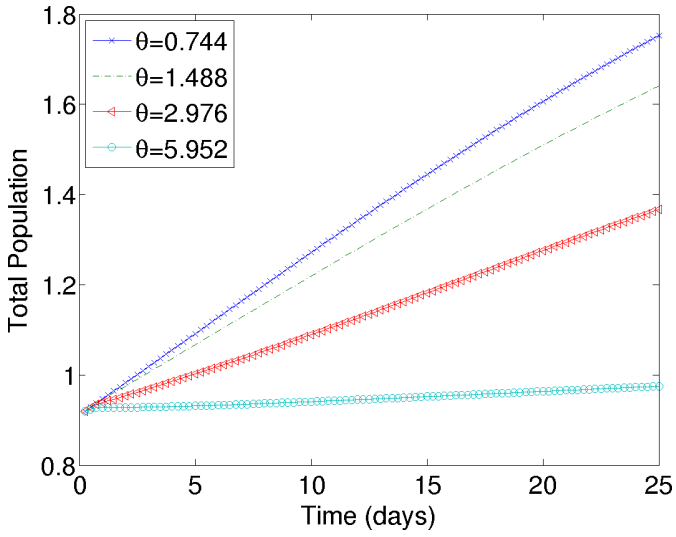

Figure 4.75 Total cell population in the scaffold for the four different nutrient uptake rates, θ.

CHAPTER 5

HAPTOTAXIS

5.1 Introduction

Until this point the model considered only how a local cell density increased due to supply of nutrient via a perfused flow. The results presented in the previous chapter indicate quite well that with the parameter values presented in Table 3.4 the final cell density somewhat closely resembles the initial prescribed cell seeding density. As seeding the scaffold with a set initial density is not a trivial process, an alternative method to obtain a prescribed final cell density without increasing the complexity of the initial seeding could be very useful.

The alternative process investigated in this chapter is the concept of bioprinting a growth factor onto the scaffold, to (i) direct cell motion up gradients in growth factor via haptotaxis; and (ii) stimulate enhanced proliferation in regions of high growth factor concentration. Haptotaxis is the directional motility or outgrowth of cells, usually up a gradient of either adhesion proteins or another chemoattractant (the growth factor, here). The motivation for this extension to the model is experimental work by Miller *et al.* [28, 29], who realized that it is much easier to bioprint growth factor onto a scaffold in chosen patterns than it is to seed the scaffold with cells in the desired final pattern.

In this chapter, we will first present the the changes to the model brought about by introducing this new effect. We then compare results presented by the model qualitatively to experimental images produced by Miller *et al.* in [28, 29] to show that the model seems to capture the main effects of introducing a spatially fixed growth factor density to the scaffold. We will then present some theoretical simulations, comparing to a few of the simulations presented in Chapter 4 as well

as some interesting supplementary simulations that illustrate the potential of this approach.

5.2 Model Development

The inclusion of growth factor is assumed to have no direct effect on either the fluid flow or the nutrient concentration in the culture medium, hence equations (2.1), (2.2), and (2.4) (and their dimensionless forms, equations (3.1), (3.2), and (3.3)) are left unchanged. The first term to be added to the cell density equation (equation (3.4)) describes cellular motility up gradients in growth factor density. To model this change, an extra term is added to the original total flux term, changing equation (2.6) to

$$\boldsymbol{J}_c^* = \boldsymbol{u}_c^* c - D_c^* \nabla^* c^* + \alpha^* c^* \nabla^* \rho^*, \tag{5.1}$$

where α^* is the haptotactic coefficient, and $\rho^* = \rho^*(\boldsymbol{x}^*, t)$ is the local growth factor density. This form of haptotactic flux is well known and can be found, for example, in [31]. The growth factor is bioprinted onto the scaffold, where it is assumed to stimulate proliferation. Hence, we add a source term, $\gamma^* f(\rho^*)$ (where γ^* is a dimensional constant and f is an order-one function accounting for the growth-factor dependence) to the cell density equation. We expect that the rate of supplemental proliferation will be small when there is only a small amount of growth factor available and it will saturate at high growth-factor concentrations. We take then

$$f(\rho^*) = \frac{\rho^{*\zeta}}{\rho_0^{*\zeta} + \rho^{*\zeta}}, \tag{5.2}$$

for a chosen value of ζ. Plots of $f(\rho)$ for different values of ζ are shown in Figure 5.1 where we can see that for $\zeta \geq 3$ the differences between possible forms seem to reduce. In the absence of definitive data to suggest otherwise, we choose $\zeta = 3$ for our simulations.

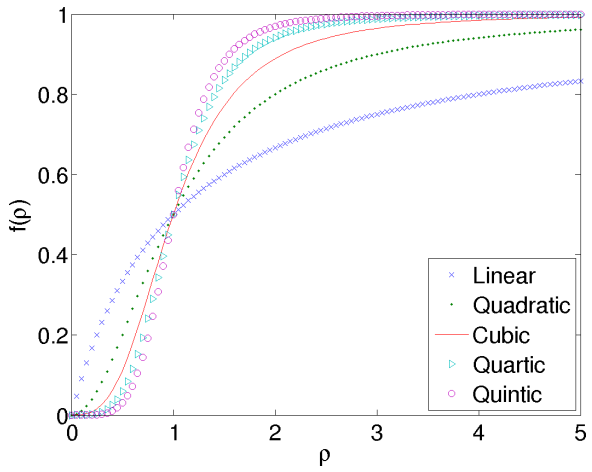

Figure 5.1 Graphical representation of possible functional forms for the supplemental growth factor term with $\zeta = 1, 2, 3, 4, 5$ in equation (5.2).

5.2.1 Revised Cell Density Equation

These two new terms can now be introduced to the cell density equation to change equation (2.8) to

$$\frac{\partial c^*}{\partial t^*} + \boldsymbol{u}_c^* \cdot \nabla^* c^* = D_c^* \nabla^{*2} c^* - \alpha^* \nabla^* \cdot (c^* \nabla^* \rho^*) + \lambda^* g^*(n^*, c^*) - \nu^* c^* + \gamma^* f(\rho^*), \quad (5.3)$$

where γ^* is a representative supplemental rate of change of cell density. We nondimensionalize the growth factor with a characteristic density ρ_0^* so that $\rho^* = \rho_0^* \rho$, giving the dimensionless form of equation (5.3) as

$$\frac{\partial c}{\partial t} + \frac{\delta}{\epsilon} \boldsymbol{u}_p \cdot \nabla c = D_c \nabla^2 c - \alpha \nabla \cdot (c \nabla \rho) + g(n, c, \tau_s) - \nu c + \gamma c f(\rho), \quad (5.4)$$

where $\alpha = (\alpha^* \rho_0^*)/(\lambda^* L^{*2})$, $\gamma = \gamma^*/\lambda^*$ and

$$f(\rho) = \frac{\rho^3}{1 + \rho^3}. \quad (5.5)$$

The numerical method described in §4.1 is unchanged by introducing the new terms, and the same ADI-type method is used with the two extra terms simply added to the discretization.

5.2.2 Growth Factor Decay Equation

The introduction of a new dependent variable requires another equation to complete the system. Since the growth factor will be bioprinted onto the scaffold, it will not undergo advection or diffusion (hence haptotaxis rather than chemotaxis); it will, however, decay as it is used up by the cells. We take

$$\frac{\partial \rho^*}{\partial t^*} = -\psi^* c^* \rho^*, \tag{5.6}$$

where ψ^* is a constant dimensional parameter capturing the rate at which growth factor is consumed by the cells. With the previously noted scaling factors, this equation nondimensionalizes to

$$\frac{\partial \rho}{\partial t} = -\psi c \rho, \tag{5.7}$$

with $\psi = (\psi^* c_0^*)/\lambda^*$. This supplemental equation requires us to prescribe the initial growth factor density, $\rho(x, y, 0) = \rho_0(x, y)$. The expectation is that the final simulated cell density will be affected directly by the choice of initial growth factor density, so the specific form of $\rho_0(x, y)$ will be presented for each simulation. The cell density and growth factor density are both prescribed at the initial time, and the cell density is first solved at the next time-step using the set growth factor density. The cell density obtained at this new time-step is used with the cell density from the old time-step to solve for the growth factor at the new time-step.

5.2.3 Additional Parameter Values

Finally, we need to determine appropriate values for the new dimensionless parameters, α, γ, and ψ. Since the concept of bioprinting growth factor to direct motility and enhance cell proliferation is a relatively novel concept, there is a lack of empirical data to inform suitable values. The dimensionless haptotactic coefficient, α, may take a wide range of values depending on the particular substrate and haptoattractant. Friedman *et al.* [18] noted values between 0.001 and 1 over many different systems. Since Miller *et al.* [28,29] believe haptotactic effects to be negligible in their experimental system, we choose a small value for the majority of our simulations, $\alpha = 0.001$ (finding observable effects nonetheless). The dimensionless rate of supplemental growth due to growth factor, γ, is chosen so that it is not higher than regular growth determined by $g(n, c, \tau_s)$, and the degradation rate of growth factor, ψ, is chosen so that growth factor decays neither too slowly nor quickly in comparison to regular cell proliferation. All other parameters used are those described in Table 3.4.

5.3 Simulation Results

The first simulations presented will be qualitative comparisons to experimental results obtained by Miller *et al.* in [28,29]. We then present some comparisons to results from the basic model to observe the specific effect of adding growth factor to the scaffold. Finally, we present simulations with some more complex initial growth factor seedings to investigate the feasibility of directing cell densities into desired final forms.

5.3.1 Comparison of the Model to Experimental Results

As noted in the introductory chapter, there has been promising experimental work in which fibroblast growth factor 2 is bioprinted onto scaffolds to stimulate cell proliferation [6, 28, 29]. In this section, we use our model to reproduce, *qualitatively*,

the key observations of Miller *et al.* [28], in which osteosarcoma cells are seeded uniformly onto scaffolds with different concentrations of growth factor printed uniformly onto a central square region within the scaffold. In the absence of full data (describing cell features such as death rate, diffusion coefficient, etc.) for osteosarcoma cells, we use the available data for chondrocyte growth (detailed in Tables 3.3 and 3.4) and compare the experimental images with theoretically-obtained contour plots of local cell density after approximately 61 hours (figure 5.2 and 5.3) and 176 hours (figure 5.4 and 5.5). The experimental images, reproduced in Figures 5.2 and 5.4 clearly demonstrate enhanced cell proliferation in the central square region containing growth factor, an effect that persists over time (cells also proliferate in the region free from growth factor, but at a lower rate).

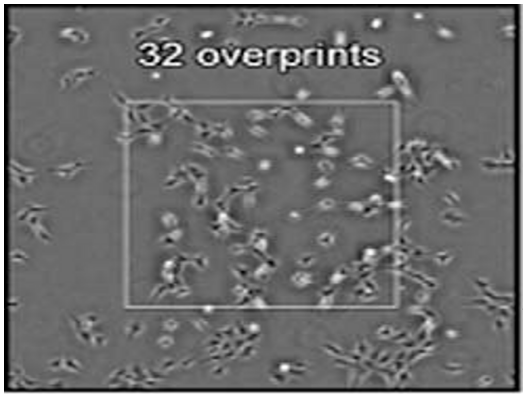

Figure 5.2 Experimental image from [28] at 61 hours with model parameters from Table 3.4, and $\hat{\rho}_0 = 0.32$.

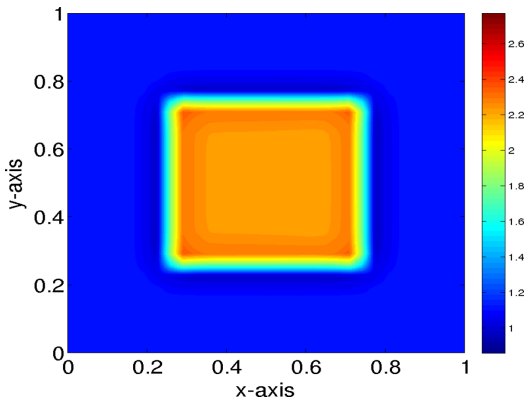

Figure 5.3 Simulation image at 61.6 hours with model parameters from Table 3.4, and $\hat{\rho}_0 = 0.32$.

The experimental images in Figures 5.2 and 5.4 contain the phrase "32 overprints": higher growth factor densities were obtained by printing the same area of the scaffold multiple times. In principle, the initial growth factor density should be proportional to the number of overprints. We simulate these experimental conditions

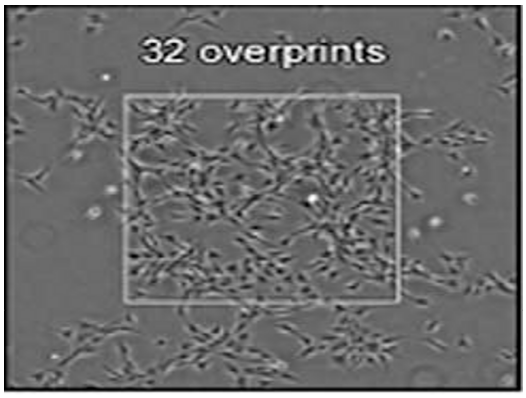

Figure 5.4 Experimental image from [28] at 176 hours with model parameters from Table 3.4, and $\hat{\rho}_0 = 0.32$.

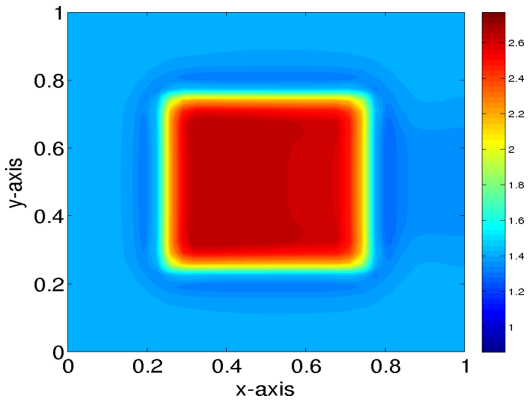

Figure 5.5 Simulation image at 176 hours with model parameters from Table 3.4, and $\hat{\rho}_0 = 0.32$.

by using an initial growth factor density

$$\begin{aligned} \rho(x,y,0) &= \hat{\rho}_0(\tanh(50(x-0.25)) - \tanh(50(x-0.75))) \times \\ &\times \quad (\tanh(50(y-0.25)) - \tanh(50(y-0.75))), \end{aligned} \tag{5.8}$$

where we chose $\hat{\rho}_0 = 0.32$ (so that in principle, a value of $\hat{\rho}_0 = 1$ corresponds to 100 overprints).

Figures 5.7-5.11 and 5.12-5.16 show the comparison between experiment and theory as the initial growth factor density is varied. The experimental results shown are for 2, 12, 22 and 32 overprints of growth factor respectively: to mimic this in our model, we used $\hat{\rho}_0 = 0.02$, 0.12, 0.22 and 0.32. Results are compared after 61 hours (Figures 5.7-5.11) and 176 hours (Figures 5.12-5.16). As the initial growth factor density increases (more overprints), the experiments showed higher cell numbers in the printed region, a feature that the model reproduces. We emphasize that the comparison is not intended to be quantitative, not least because the full dataset needed to simulate correctly the experimental setup is not available. Note also that the experimental printed region is very small, making a continuum approximation for

the cell density here questionable. In particular, the gradients of cell density that emerge in the simulations would not be evident in an experiment carried out on this scale. Nonetheless, the qualitative agreement for the similar systems is encouraging.

A study of simulated total (normalized) cell population over time (Figure 5.6) reveals that with higher initial growth factor densities, cells proliferated to higher final populations, as would be expected. Note that the final growth-rate appears to be linear in time.

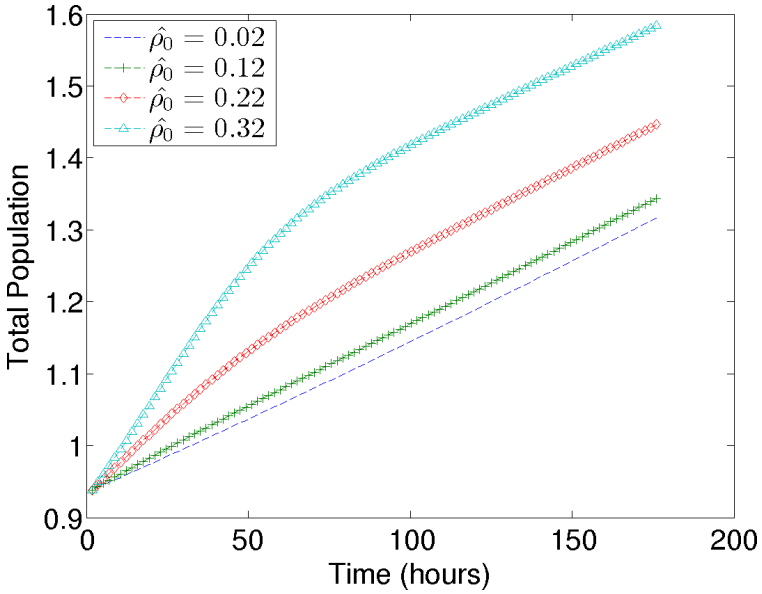

Figure 5.6 Simulations of total normalized cell population for differing growth factor overprints as seen in Figures 5.8-5.16 with parameters from Table 3.4.

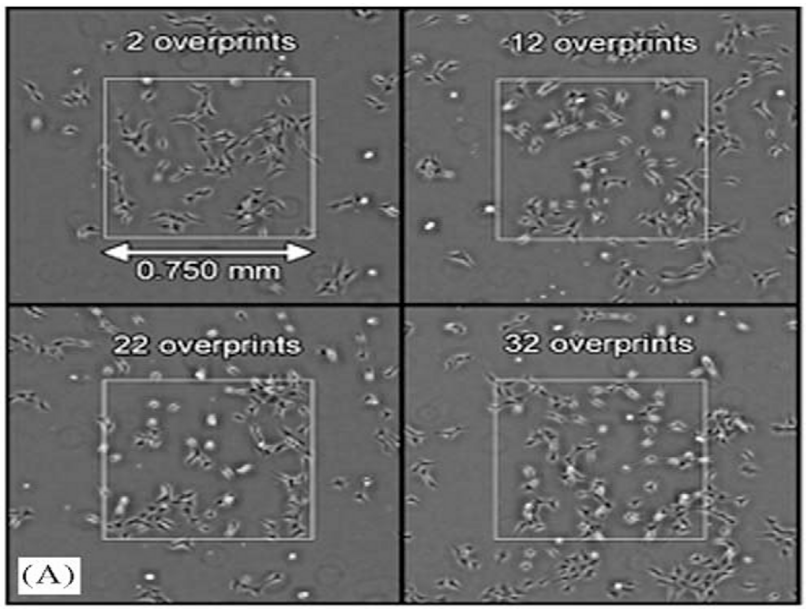

Figure 5.7 Experimental results with differing overprint values at 61 hours.

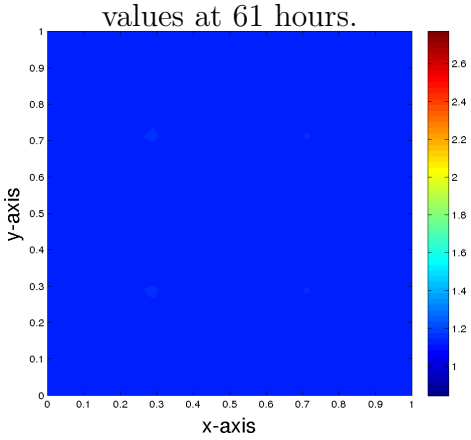

Figure 5.8 Experimental simulation results with $\hat{\rho}_0 = 0.02$ at 61.6 hours.

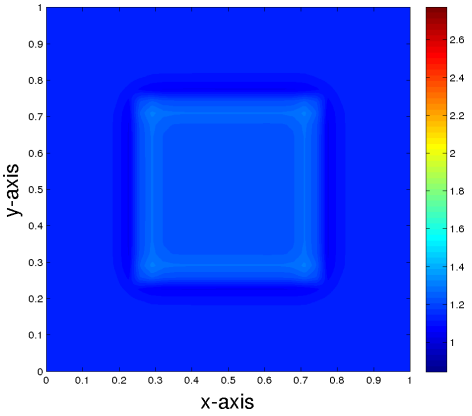

Figure 5.9 Experimental simulation results with $\hat{\rho}_0 = 0.12$ at 61.6 hours.

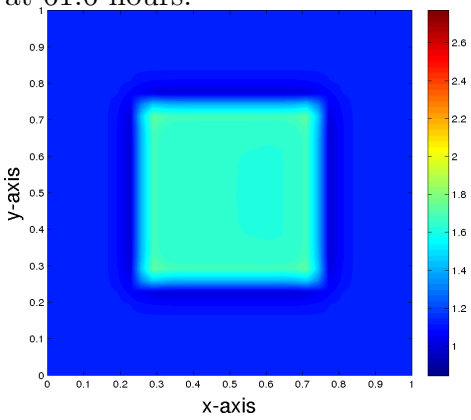

Figure 5.10 Experimental simulation results with $\hat{\rho}_0 = 0.22$ at 61.6 hours.

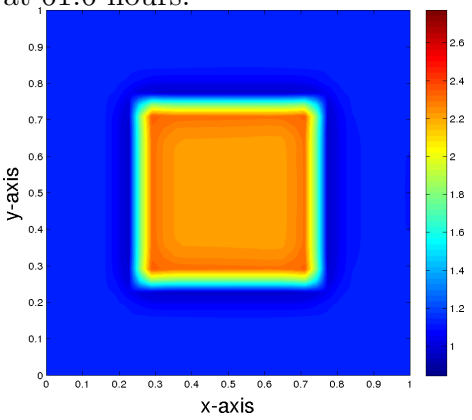

Figure 5.11 Experimental simulation results with $\hat{\rho}_0 = 0.32$ at 61.6 hours.

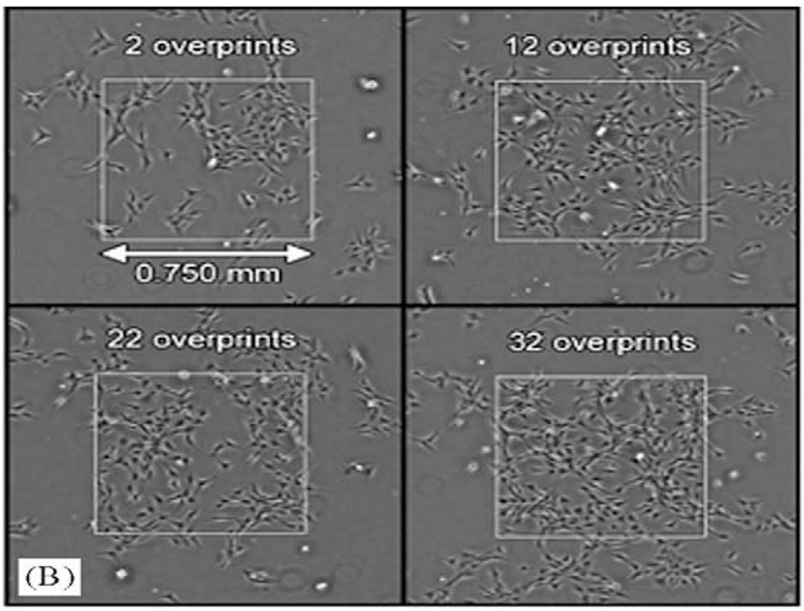

Figure 5.12 Experimental results with differing overprint values at 176 hours.

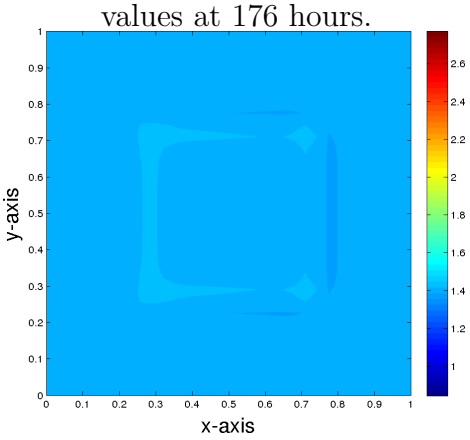

Figure 5.13 Experimental simulation results with $\hat{\rho}_0 = 0.02$ at 176 hours.

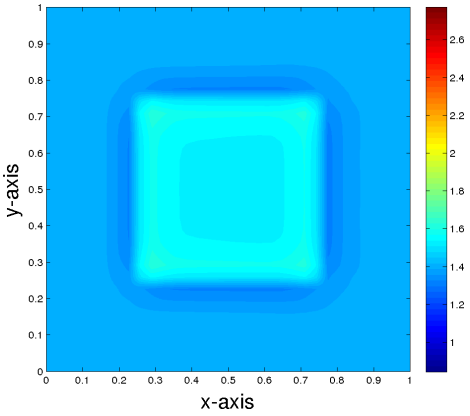

Figure 5.14 Experimental simulation results with $\hat{\rho}_0 = 0.12$ at 176 hours.

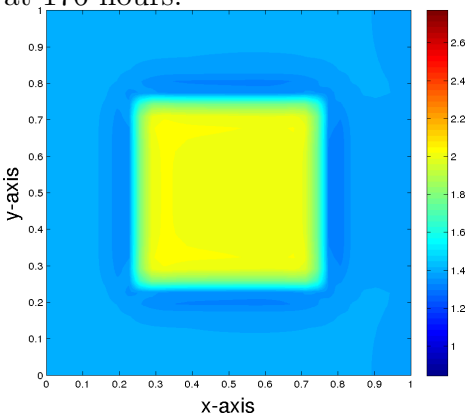

Figure 5.15 Experimental simulation results with $\hat{\rho}_0 = 0.22$ at 176 hours.

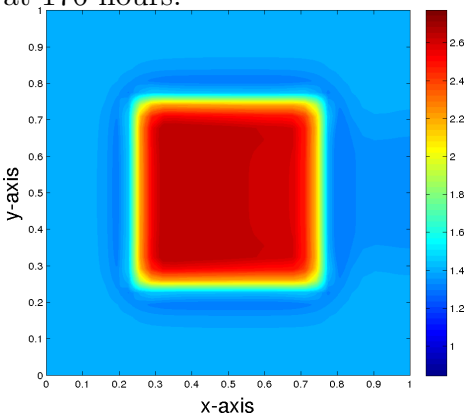

Figure 5.16 Experimental simulation results with $\hat{\rho}_0 = 0.32$ at 176 hours.

5.3.2 The Role of Haptotaxis

Despite the impossibility of making quantitative comparison, the results of the previous subsection suggest significant correlation between the experiments and our simulations. In [28], Miller *et al.* state that the primary organizational response to the growth factor by the cells is simple proliferation and not haptotactic migration. However, in these experiments, the gradients in the initial growth factor distributions are almost everywhere very small, and we therefore might not anticipate significant haptotactic movement of cells. To investigate the role of haptotaxis in our model, even with the small value of the haptotactic coefficient α used ($\alpha = 0.001$), we can run simulations in which the coefficient of the supplemental growth term in equation (3.4), γ, is set to zero, while haptotaxis is either "on" ($\alpha > 0$) or "off" ($\alpha = 0$). We use the same square growth factor distribution as previously (equation (5.8)), with $\hat{\rho}_0 = 0.32$.

Figures 5.17 and 5.19 in which haptotaxis is "on" both indicate distinct cell motility towards the center of the domain, where growth factor is present, whereas Figures 5.18 and 5.20, in which the growth factor is passive, show a relatively uniform cell density across the domain.

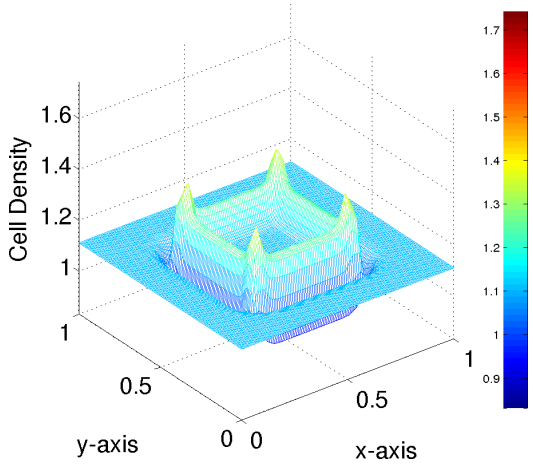

Figure 5.17 Effects of haptotaxis included with supplemental growth removed ($\gamma = 0$) at 61.6 hours.

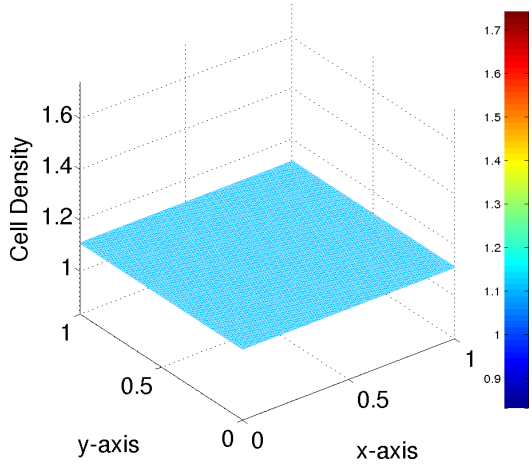

Figure 5.18 Effects of both haptotaxis and supplemental growth removed ($\alpha = 0, \gamma = 0$) at 61.6 hours.

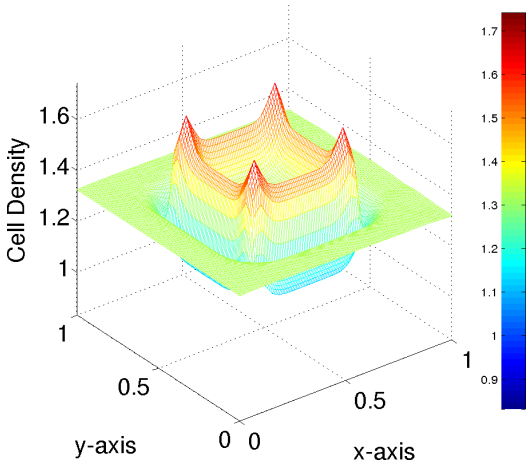

Figure 5.19 Effects of haptotaxis included with supplemental growth removed ($\gamma = 0$) at 176 hours.

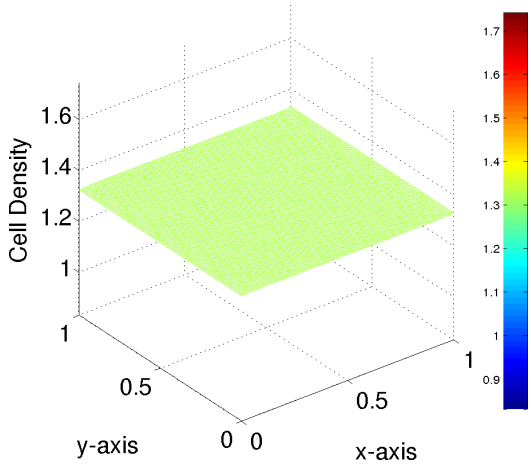

Figure 5.20 Effects of both haptotaxis and supplemental growth removed ($\alpha = 0, \gamma = 0$) at 176 hours.

Figure 5.21 shows the total (normalized) cell population in the entire domain versus time for the cases of haptotaxis and no haptotaxis (with no supplemental growth-factor-induced proliferation), indicating that the total cell population is almost unchanged by haptotaxis alone. Figures 5.17-5.21 together demonstrate that,

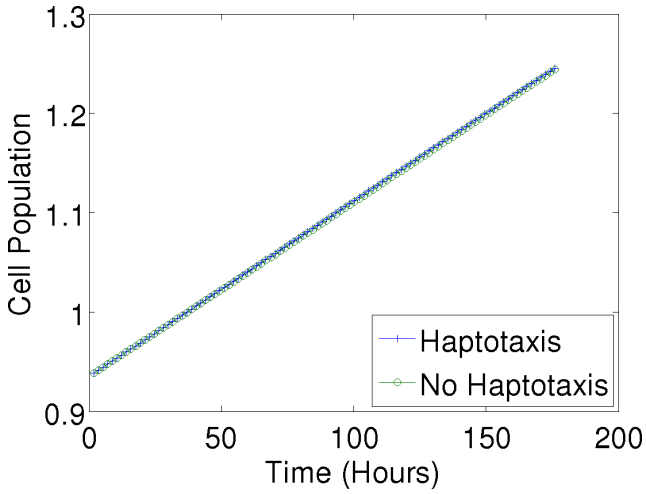

Figure 5.21 Total cell population with and without haptotaxis (no supplemental growth in both cases), with parameters from Table 3.4.

while haptotaxis does not affect the total cell population, cell migration does in fact play a role in the cell density spatial evolution in our model.

5.4 Beyond the Experiments: Further Theoretical Simulations

As observed, though haptotaxis may be playing a role in the experiments of [28], its effect is hard to detect, since gradients of growth factor are small over most of the domain, and any cell migration due to the growth factor is swamped by the enhanced proliferation it stimulates. To examine more thoroughly possible effects of haptotaxis, we also simulate selected scenarios where the initial cell seeding is spatially non-uniform, and where more exotic growth factor distributions are used.

First, we assume that it is experimentally easier to seed cells on the perimeter of the scaffold than uniformly throughout. Then, growth factor printed on the scaffold interior could (in principle) be used to attract cells from the periphery to the interior, giving a final cell density that is more or less uniform. Thus we simulate this scenario, and compare to the case where no growth factor is present. We also simulate a scenario where the initial cell density is constant, but the growth factor concentration increases linearly throughout the domain (a uniform initial growth factor gradient). We then simulate the effects of a banded initial growth factor distribution, with various initial cell densities.

Finally, we carry out sample simulations to investigate the effects of (i) changing the haptotactic coefficient, α; and (ii) changing the cellular advective drag coefficient, δ (see equation (5.4)).

5.4.1 Peripheral Cell Seedings

Here we model a scenario where cells are seeded only on the perimeter of the domain (Figures 5.22) and migrate inwards, under advection, haptotaxis (with initial growth-factor distribution as in Figure 5.23), and diffusion.

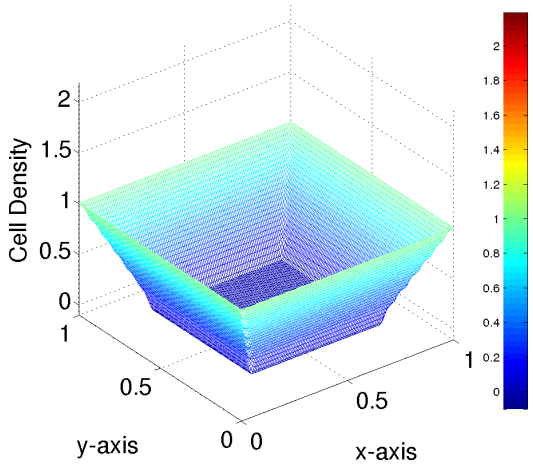

Figure 5.22 Initial cell seeding around periphery of scaffold.

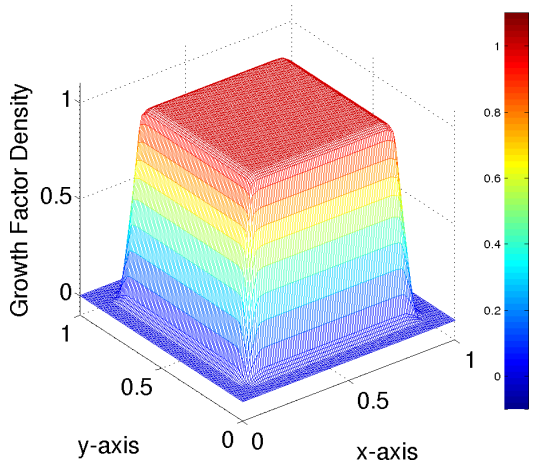

Figure 5.23 Initial growth factor seeding in central region of scaffold.

In Figures 5.24-5.27, we compare model results without and with growth factor, for the initial conditions of Figures 5.22 and 5.23. Figures 5.24 and 5.25 show results after five days and Figures 5.26 and 5.27 show results after twenty-five days. The cell migration towards the (initially empty) center of the domain is relatively slow, due to the small values assigned to cellular advective velocity, cellular diffusive flux and haptotaxis in our model; increasing the associated parameters would give more dramatic results far sooner.

Figure 5.28 shows the total normalized cell populations over time for these simulations, and also the cell density at the center of the scaffold. It is clearly seen that the total cell population grows faster when growth factor is introduced, an effect that increases over time. This effect is even more pronounced in the center of the scaffold, as seen in Figure 5.29.

Comparison of Figures 5.24 and 5.26 to Figures 5.25 and 5.27 shows that inclusion of growth factor with attendant haptotaxis and enhanced proliferation significantly affects the final outcome. In particular, the cells migrate much further into the interior within the same time period when the growth factor is present, due to

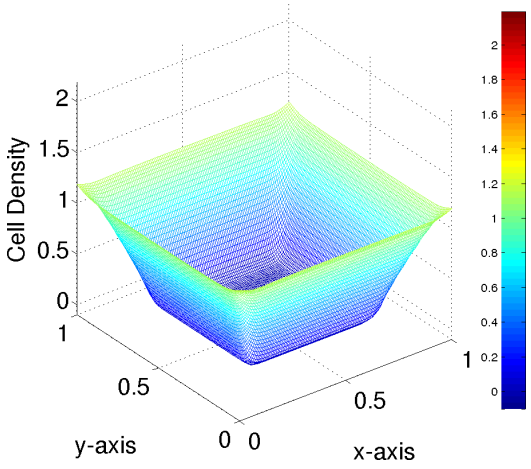

Figure 5.24 Cell density after 120 hours with initial peripheral cell seeding and no growth factor.

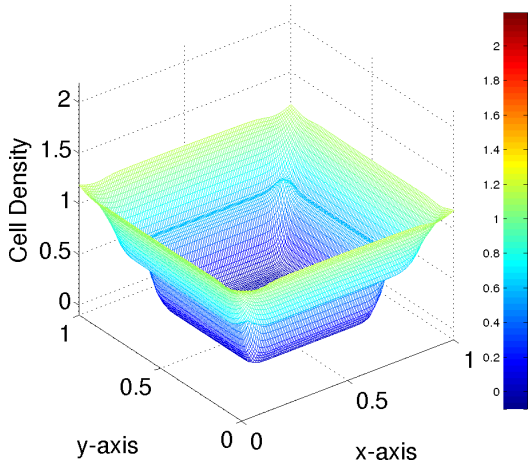

Figure 5.25 Cell density after 120 hours with initial peripheral cell seeding and central growth factor seeding.

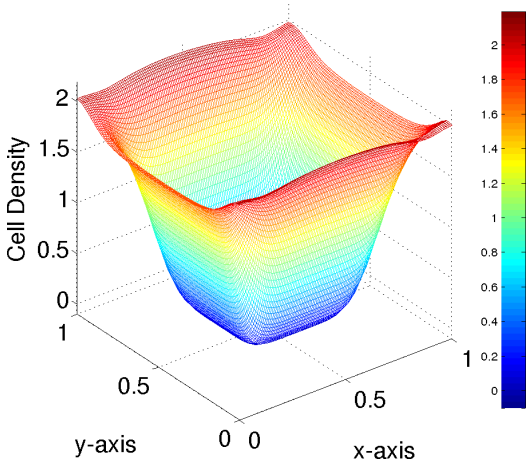

Figure 5.26 Cell density after 600 hours with initial peripheral cell seeding and no growth factor.

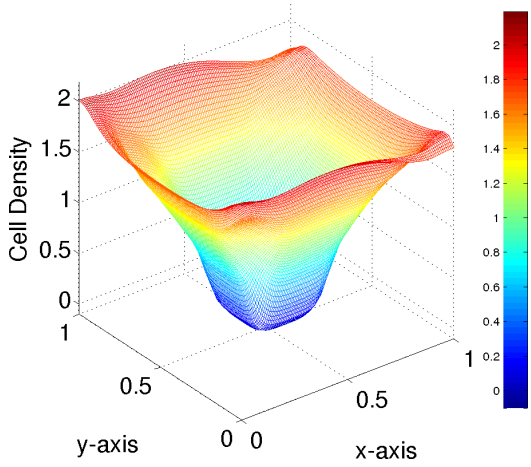

Figure 5.27 Cell density after 600 hours with initial peripheral cell seeding and central growth factor seeding.

the haptotaxis, an effect that was not largely evident in the experimental simulations (with the same parameters, but different initial conditions).

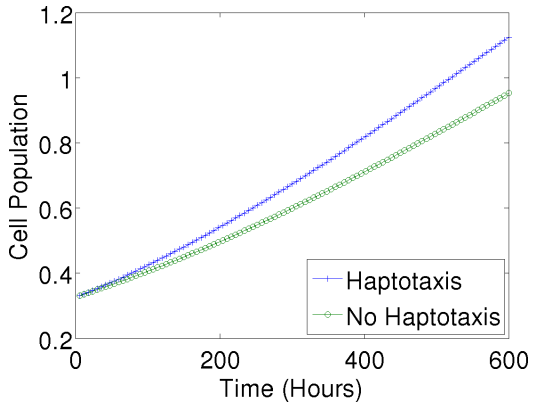

Figure 5.28 Total cell density comparison (with and without growth factor) of peripheral cell seeding central with growth factor seeding.

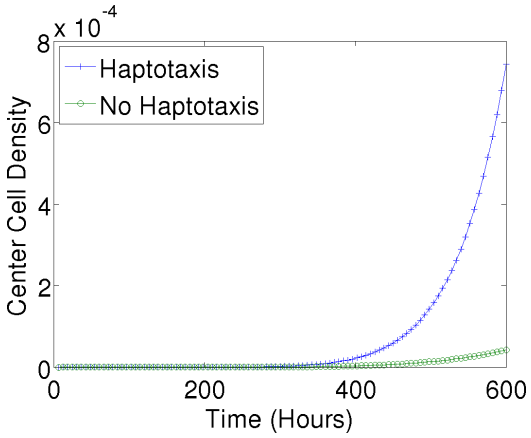

Figure 5.29 Center cell density comparison (with and without growth factor) of peripheral cell seeding central with growth factor seeding.

5.4.2 Higher Growth Factor Levels

The previous simulation leads us to examine the possibility of increasing the levels of growth factor throughout the scaffold to see under what conditions the cell density attains a relative uniformity by the end of the simulation. To achieve this, we can make two simple change to equation (5.9): increasing the value of $\hat{\rho}_0$ and seeding the entire region with growth factor instead of just the center. We consider the growth factor seeding

$$\begin{aligned} \rho(x,y,0) &= 0.75(\tanh(50(x-0.25)) - \tanh(50(x-0.75))) \times \\ &\times (\tanh(50(y-0.25)) - \tanh(50(y-0.75))) + 1, \end{aligned} \tag{5.9}$$

which provides growth factor to the entire scaffold, with a much more concentrated amount around the center. The new initial growth factor density is presented in Figure 5.30 and the results of this simulation are seen in Figures 5.31-5.33.

We clearly see aggressive cell migration and much higher proliferation after fifteen days (Figure 5.32) and after the full simulation of twenty-five days (Figure 5.33) the cell density throughout the entire scaffold seems to have reached a relatively

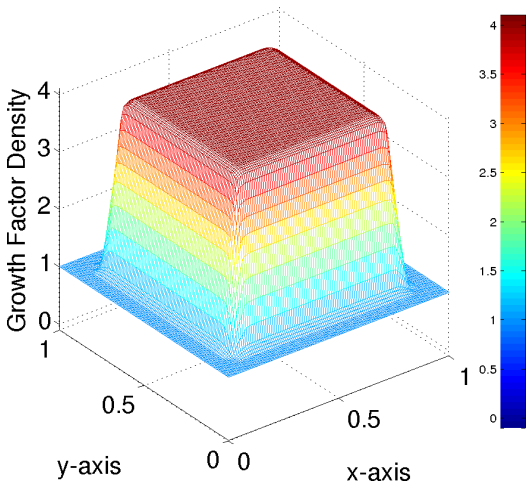

Figure 5.30 Increased growth factor seeding as described in equation (5.9).

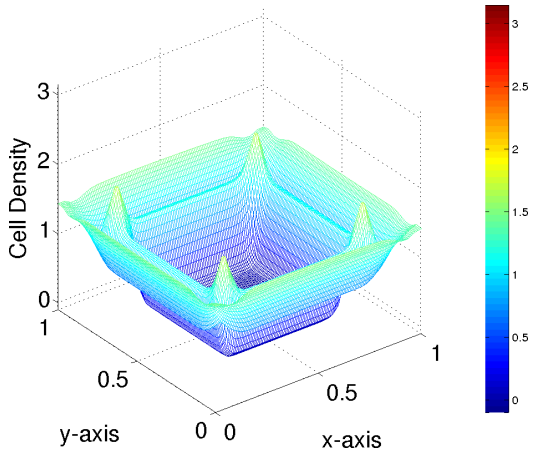

Figure 5.31 Cell density after 120 hours with initial peripheral seeding and higher central growth factor seeding as described in equation (5.9).

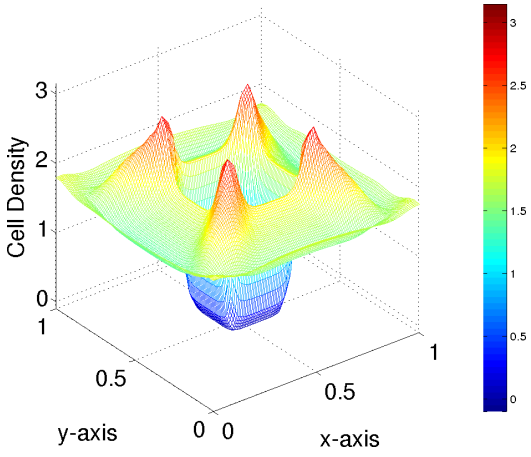

Figure 5.32 Cell density after 360 hours with initial peripheral seeding and higher central growth factor seeding as described in equation (5.9).

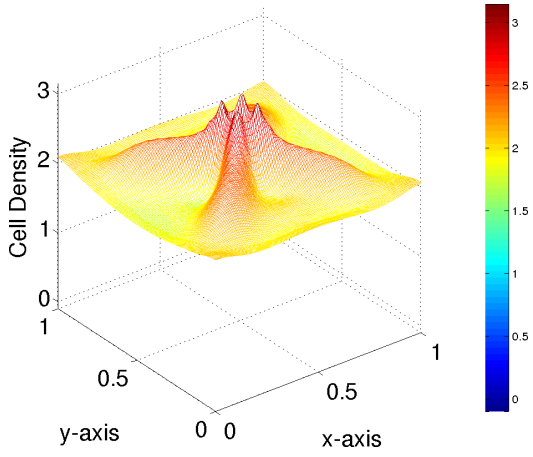

Figure 5.33 Cell density after 600 hours with initial peripheral seeding and higher central growth factor seeding as described in equation (5.9).

uniform distribution. It is unknown if such a high growth factor density is possible but these simulations provide promising indications that it may be possible to achieve a fully-populated scaffold from only a peripheral initial cell seeding.

5.4.3 Linear Growth Factor Distribution

To illustrate further the haptotaxis, we simulate a scenario in which a uniform (but skewed with respect to the flow direction) initial growth factor gradient exists, with initially-uniform cell seeding,

$$\rho(x, y, 0) = 3x + 3y + 1, \quad c(x, y, 0) = 1. \tag{5.10}$$

Results corresponding to this initial growth factor distribution are shown in Figures 5.34-5.37.

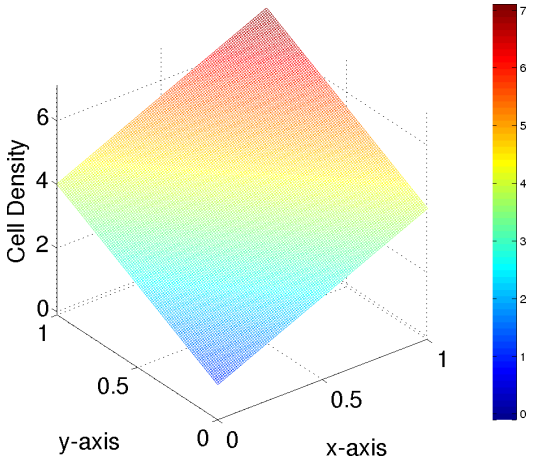

Figure 5.34 Linear growth factor initial seeding as described in equation (5.10).

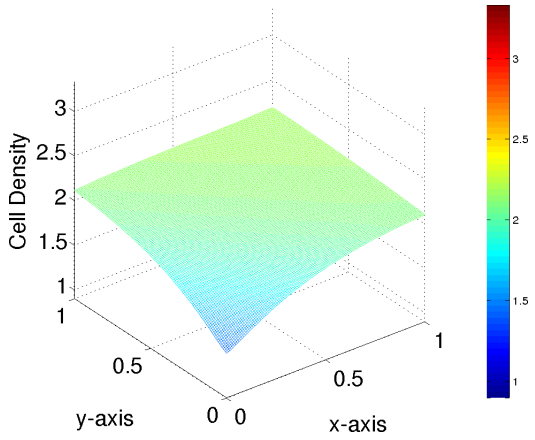

Figure 5.35 Cell density after 90 hours from constant initial cell seeding with linear initial growth factor seeding as described in equation (5.10).

After 90 hours (Figure 5.35) cell density has increased everywhere in the domain, with slightly lower density near $(x, y) = (0, 0)$, which had the lowest initial growth factor density. After 180 hours the cell density across the domain closely mirrors the original growth factor density; but the end of the simulation (600 hrs) indicates a tendency towards an eventual uniform cell density, due to the combined effects of cellular diffusion, and the higher nutrient concentration near the inlet $x = 0$. The density near $(x, y) = (1, 1)$ has decreased from 180 hours to 600 hours, most likely

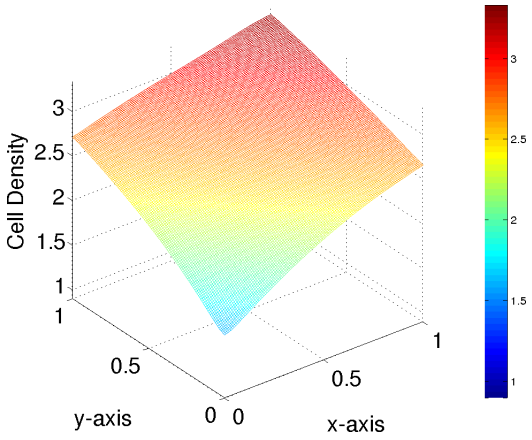

Figure 5.36 Cell density after 180 hours from constant initial cell seeding with linear initial growth factor seeding as described in equation (5.10).

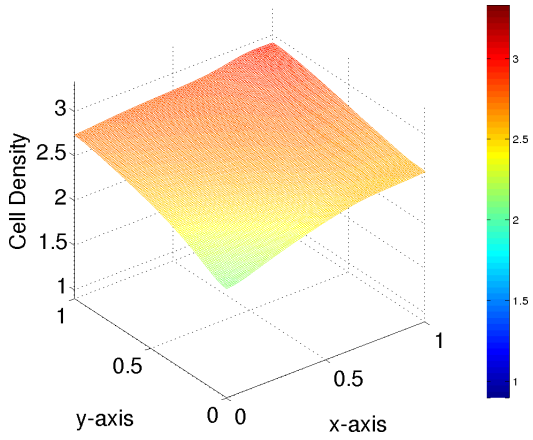

Figure 5.37 Cell density after 600 hours from constant initial cell seeding with linear initial growth factor seeding as described in equation (5.10).

due to cellular diffusion to areas of lower density. It is also possible that the transient growth-factor induced proliferation took the cell population in that region above the carrying capacity $\hat{c}(n)$, so that the proliferation is suppressed at later times once the growth factor has been used up.

5.4.4 Banded Growth Factor Printing

Our final scenario illustrates the effect of a more exotic initial growth factor distribution. We consider a banded initial growth factor density,

$$\rho(x, y, 0) = \sin(6\pi x) + 1, \tag{5.11}$$

as seen in Figure 5.38, with three different initial cell seedings. Such bioprinting of banded growth factor (or other cellular cue) may be experimentally useful when engineering tissues which contain many different cell types, e.g., liver.

We first consider a uniform initial cell seeding, simulated in Figures 5.38-5.41. We can clearly see in Figure 5.39 that after five days (120 hours) the pattern of the

cell density in the experiment nearly mirrors the initial growth factor density, showing significant banding. As time progresses, the banding becomes less pronounced (Figures 5.40 and 5.41): due to the cellular diffusion and advection of nutrient throughout the cell density rises in all areas of the scaffold (though the imprint of the initial banding is still evident).

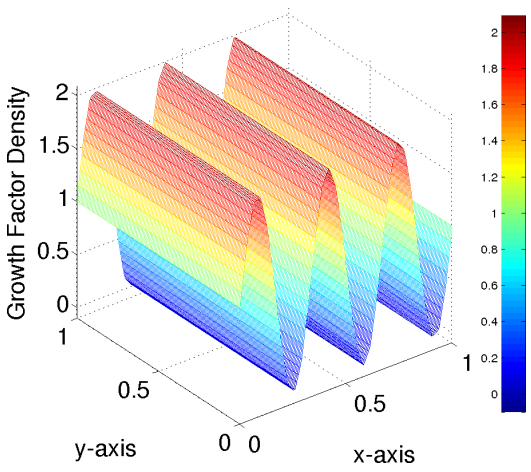

Figure 5.38 Sinusoidal initial growth factor seeding (as described in equation (5.11)) used in simulation with constant initial cell seeding.

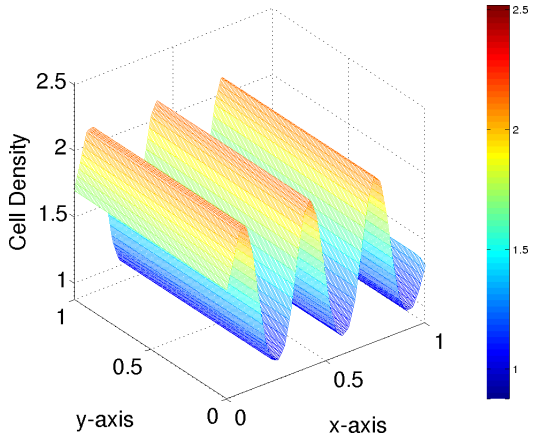

Figure 5.39 Cell density after 120 hours from simulation with constant initial cell density and sinusoidal initial growth factor density as described in equation (5.11).

Figures 5.42-5.45 and 5.46-5.49 show results for the same banded initial growth factor distribution (5.11), but with different initial cell seedings. Figures 5.42-5.45 show results for peripheral initial cell seeding at all four walls of the scaffold (shown in Figure 5.22), while Figures 5.46-5.49 show results for peripheral seeding at walls $x = 0$ and $x = 1$ only. The results for peripheral seeding at all four walls show an exotic pattern of cell density developing, due to the interplay between the initial growth factor pattern, the initial cell seeding, the nutrient flow, and the associated haptotactic, diffusive and advective effects. In particular, the fully 2D nature of the initial cell-seeding here gives rise to a fully 2D final pattern. The results with initial seeding only on two walls, on the other hand, has an initial cell seeding that is nearly

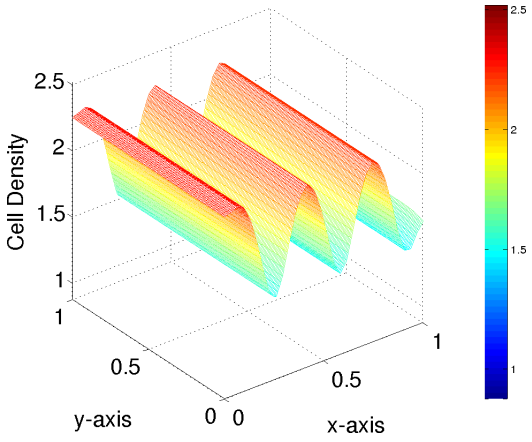

Figure 5.40 Cell density after 360 hours from simulation with constant initial cell density and sinusoidal initial growth factor density as described in equation (5.11).

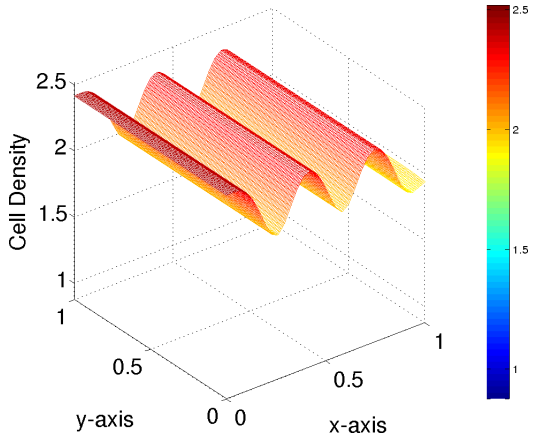

Figure 5.41 Cell density after 600 hours from simulation with constant initial cell density and sinusoidal initial growth factor density as described in equation (5.11).

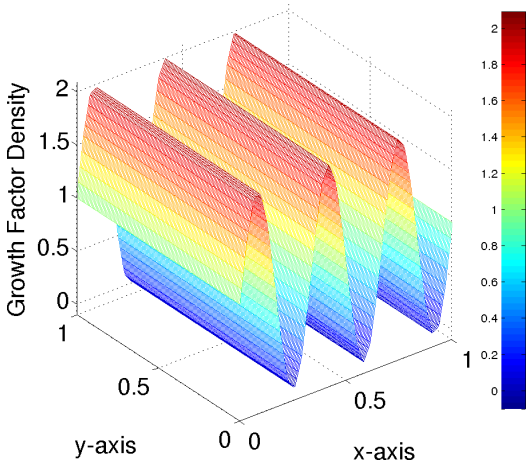

Figure 5.42 Sinusoidal initial growth factor seeding (as described in equation (5.11)) used in simulation with peripheral initial cell seeding.

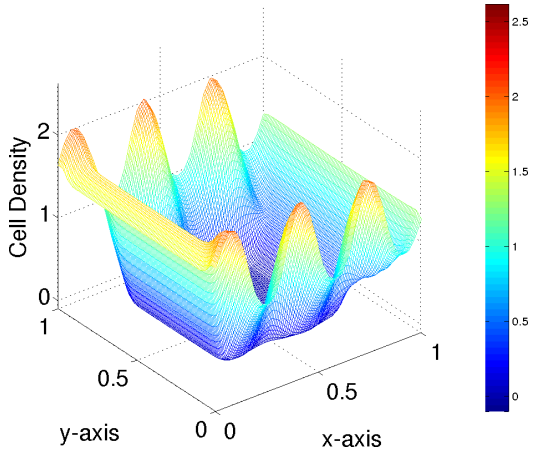

Figure 5.43 Cell density after 120 hours from simulation with peripheral initial cell density and sinusoidal initial growth factor density as described in equation (5.11).

one-dimensional (in line with the growth factor distribution), and the final pattern that develops is correspondingly nearly 1D, and less intricate than the previous case. This limited set of examples shows that with a controllable way of printing growth

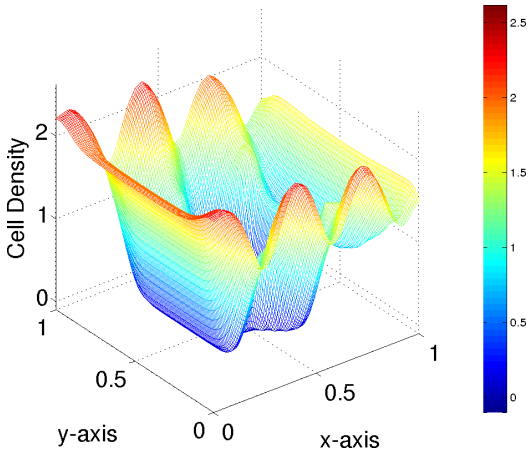

Figure 5.44 Cell density after 360 hours from simulation with peripheral initial cell density and sinusoidal initial growth factor density as described in equation (5.11).

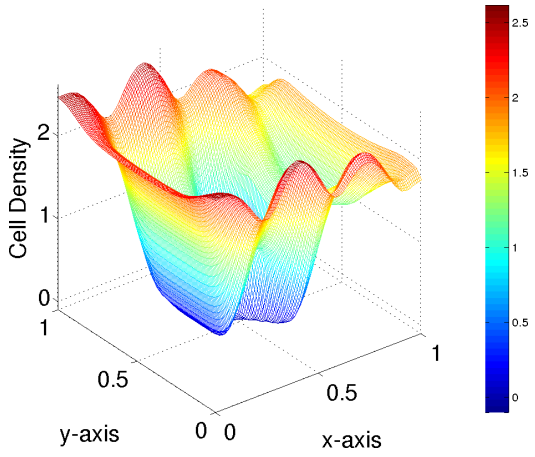

Figure 5.45 Cell density after 600 hours from simulation with peripheral initial cell density and sinusoidal initial growth factor density as described in equation (5.11).

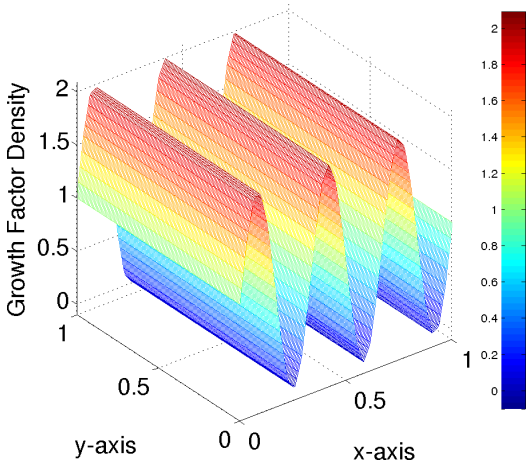

Figure 5.46 Sinusoidal initial growth factor seeding (as described in equation (5.11)) used in simulation with two-walled ($x = 0, 1$) initial cell seeding.

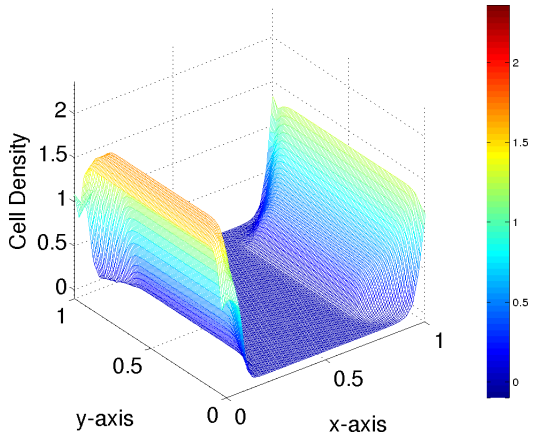

Figure 5.47 Cell density after 120 hours from simulation with two-walled ($x = 0, 1$) initial cell density and sinusoidal initial growth factor density as described in equation (5.11).

factor onto scaffolds, there is great potential for creating cellular structures with detailed spatial structure.

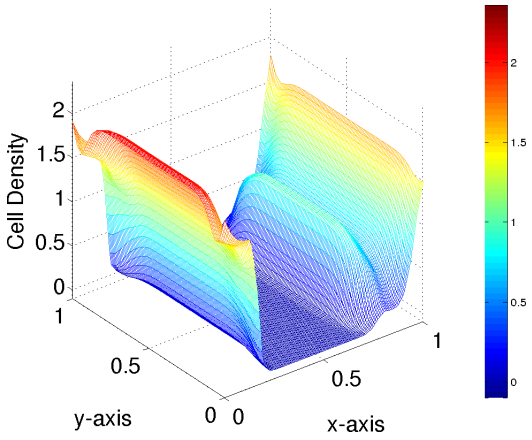

Figure 5.48 Cell density after 360 hours from simulation with two-walled ($x = 0, 1$) initial cell density and sinusoidal initial growth factor density as described in equation (5.11).

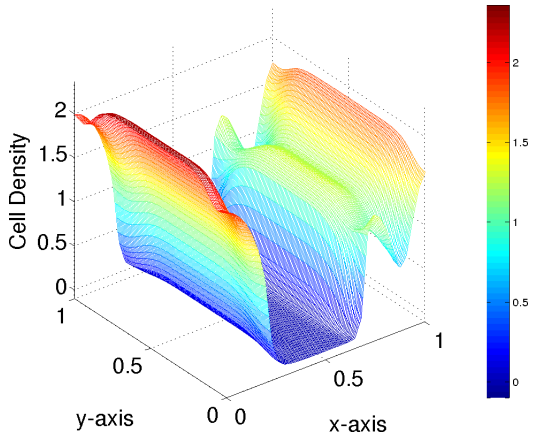

Figure 5.49 Cell density after 600 hours from simulation with two-walled ($x = 0, 1$) initial cell density and sinusoidal initial growth factor density as described in equation (5.11).

5.4.5 Varying Haptotactic and Cellular Advective Drag Coefficients α, δ

Different types of scaffold (*e.g.* different biomaterials, different pore structure, *etc.*) exhibit different cellular adhesion properties, with implications for the cell motility due to haptotaxis and fluid drag. The haptotactic cell motility would also change if a different haptoattractant was used on the scaffold. In all our simulations thus far in this chapter, we have used the same values for the haptotactic coefficient, α, and the cell advective velocity factor δ. Since these parameters were chosen in the absence of solid empirical evidence, we consider the effect of changing them to simulate different rates of cell motility and adhesion.

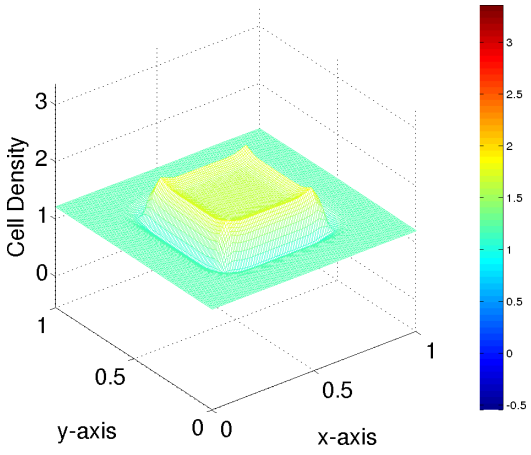

Figure 5.50 Cell density after 120 hours using original $\alpha = 0.001$ and $\delta/\epsilon = 10^{-5}$ parameter values.

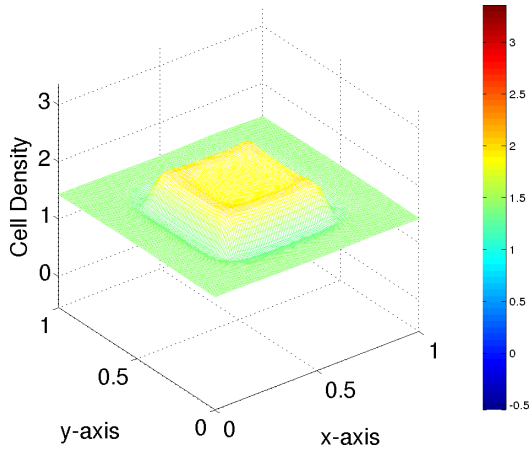

Figure 5.51 Cell density after 240 hours using original $\alpha = 0.001$ and $\delta/\epsilon = 10^{-5}$ parameter values.

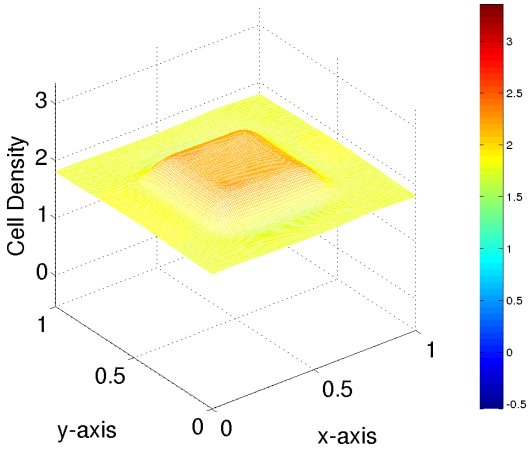

Figure 5.52 Cell density after 480 hours using original $\alpha = 0.001$ and $\delta/\epsilon = 10^{-5}$ parameter values.

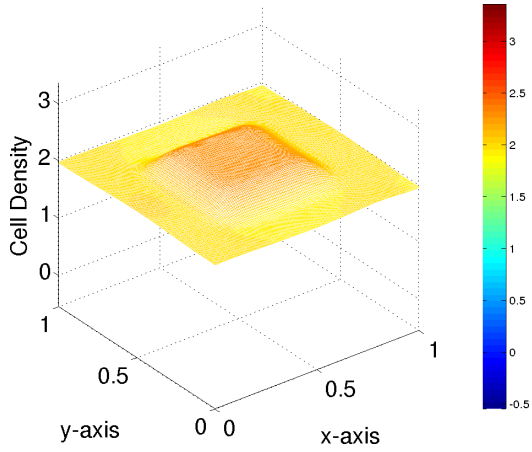

Figure 5.53 Cell density after 600 hours using original $\alpha = 0.001$ and $\delta/\epsilon = 10^{-5}$ parameter values.

In Figures 5.50-5.53 we show results of simulations with uniform initial cell seeding and initial growth factor distributed as in equation (5.8), run for a period of twenty-five days. The original parameters, presented in Table 3.4 are used; specifically, $\alpha = 0.001$ and $\delta/\epsilon = 10^{-5}$. In Figures 5.54-5.57 and 5.58-5.61 we show the analogous results with $\alpha = 0.005$ and $\alpha = 0.01$, respectively; and

in Figures 5.62-5.65 and 5.66-5.69 we show results for increased cell drag ratios, $\delta/\epsilon = 10^{-3}$ and $\delta/\epsilon = 3 \times 10^{-2}$, respectively.

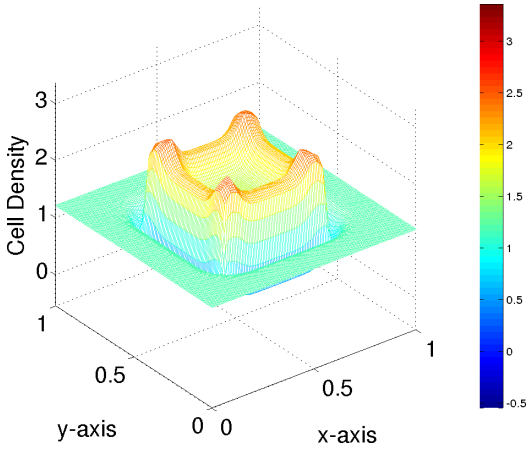

Figure 5.54 Cell density after 120 hours using $\alpha = 0.005$ and original $\delta/\epsilon = 10^{-5}$ parameter values.

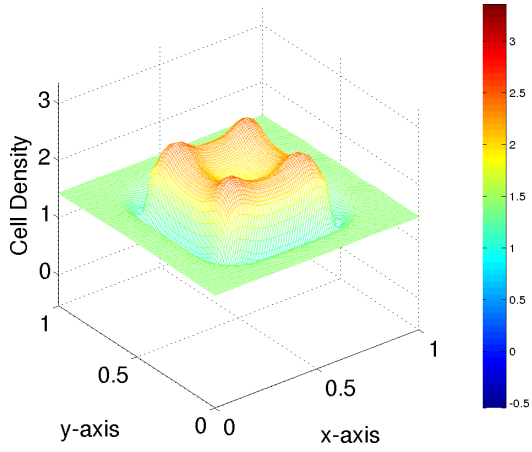

Figure 5.55 Cell density after 240 hours using $\alpha = 0.005$ and original $\delta/\epsilon = 10^{-5}$ parameter values.

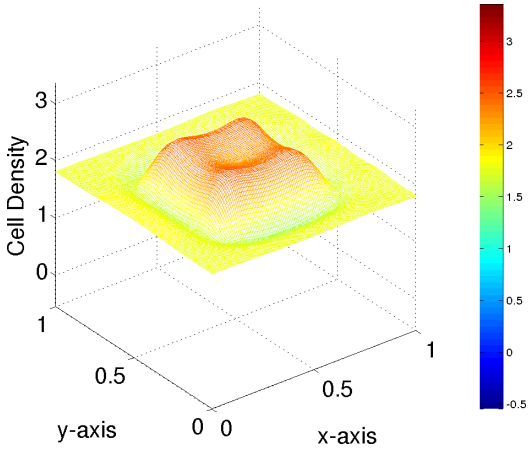

Figure 5.56 Cell density after 480 hours using $\alpha = 0.005$ and original $\delta/\epsilon = 10^{-5}$ parameter values.

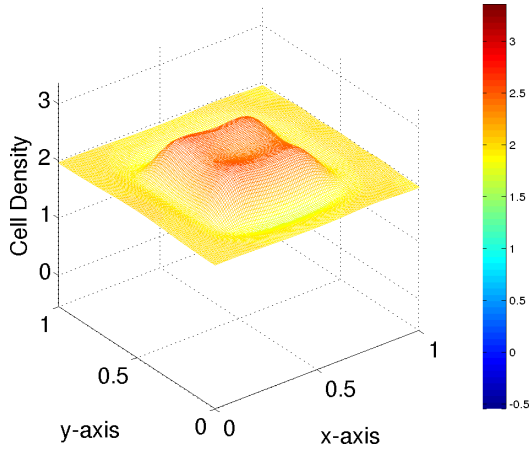

Figure 5.57 Cell density after 600 hours using $\alpha = 0.005$ and original $\delta/\epsilon = 10^{-5}$ parameter values.

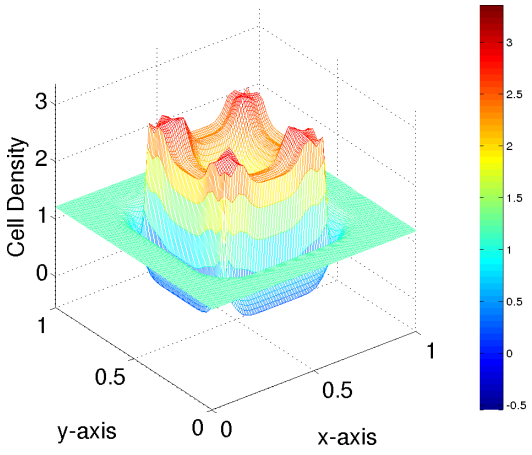

Figure 5.58 Cell density after 120 hours using $\alpha = 0.01$ and original $\delta/\epsilon = 10^{-5}$ parameter values.

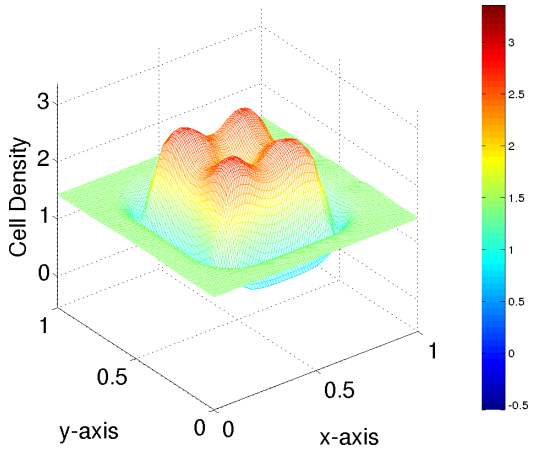

Figure 5.59 Cell density after 240 hours using $\alpha = 0.01$ and original $\delta/\epsilon = 10^{-5}$ parameter values.

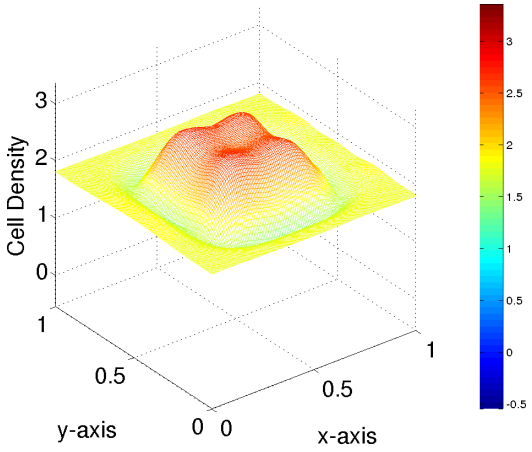

Figure 5.60 Cell density after 480 hours using $\alpha = 0.01$ and original $\delta/\epsilon = 10^{-5}$ parameter values.

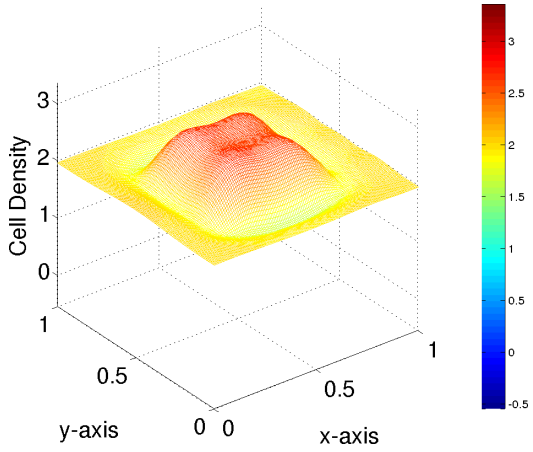

Figure 5.61 Cell density after 600 hours using $\alpha = 0.01$ and original $\delta/\epsilon = 10^{-5}$ parameter values.

Figures 5.54-5.57 and 5.58-5.61 show that the increased cell motility resulting from the larger values of α is quite visible at earlier times (5.54,5.55,5.58,5.59), as the regions in the corners of the square in which growth factor was initially printed have higher cell concentrations. The evolution at later times in all simulations follows the early-time results as expected. At later times in all three simulations proliferation has occurred throughout the entire domain (Figures 5.52, 5.53, Figures 5.56, 5.57,

and Figures 5.60, 5.61), but in the region printed with growth factor cell densities are higher as the haptotactic coefficient increases, due to the cells migrating toward the center region faster in the early stages of the simulation.

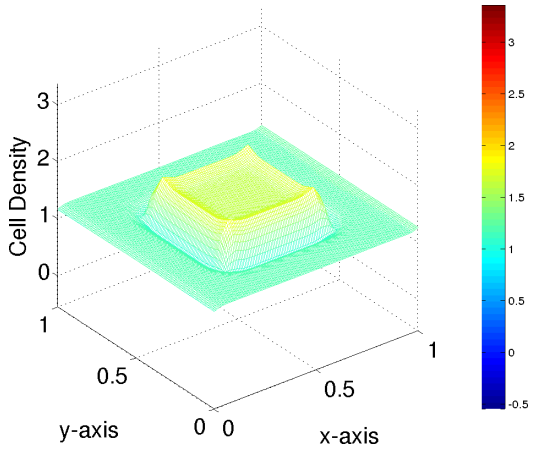

Figure 5.62 Cell density after 120 hours using $\delta/\epsilon = 10^{-3}$ and original $\alpha = 0.001$ parameter values.

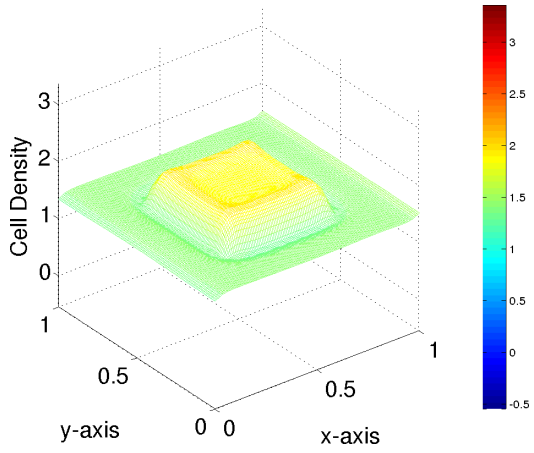

Figure 5.63 Cell density after 240 hours using $\delta/\epsilon = 10^{-3}$ and original $\alpha = 0.001$ parameter values.

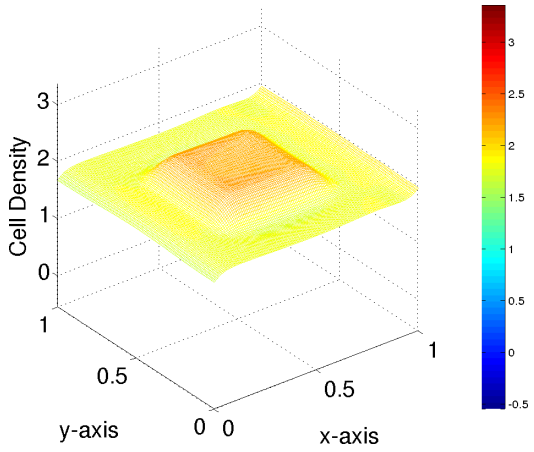

Figure 5.64 Cell density after 480 hours using $\delta/\epsilon = 10^{-3}$ and original $\alpha = 0.001$ parameter values.

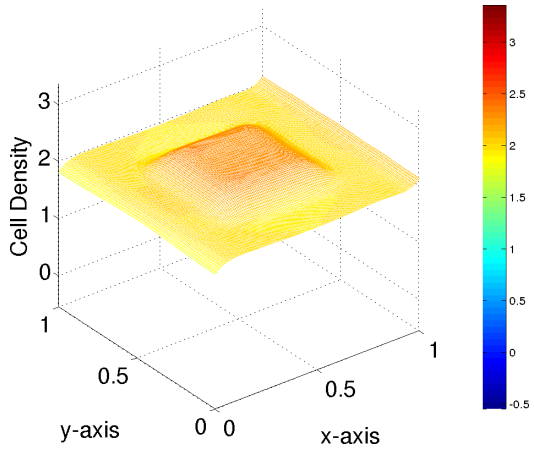

Figure 5.65 Cell density after 600 hours using $\delta/\epsilon = 10^{-3}$ and original $\alpha = 0.001$ parameter values.

Figures 5.62-5.65 and 5.66-5.69 show analogous results as the value of the cell drag coefficient is increased. Figures 5.62-5.65, with δ increased by two orders of

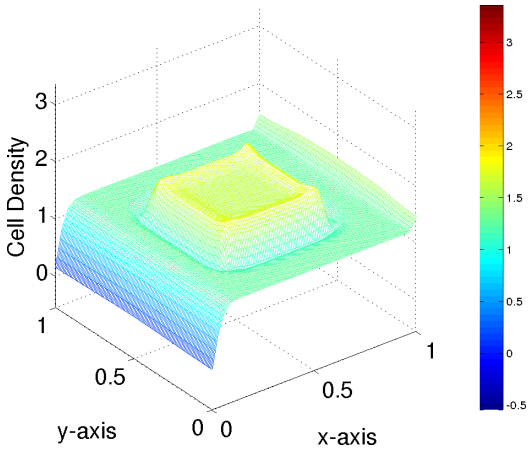

Figure 5.66 Cell density after 120 hours using $\delta/\epsilon = 3\times10^{-2}$ and original $\alpha = 0.001$ parameter values.

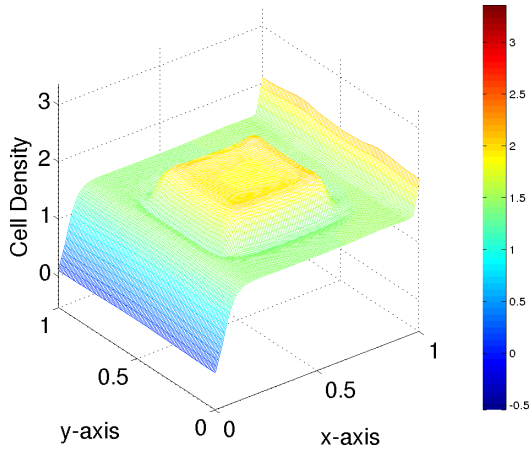

Figure 5.67 Cell density after 240 hours using $\delta/\epsilon = 3\times10^{-2}$ and original $\alpha = 0.001$ parameter values.

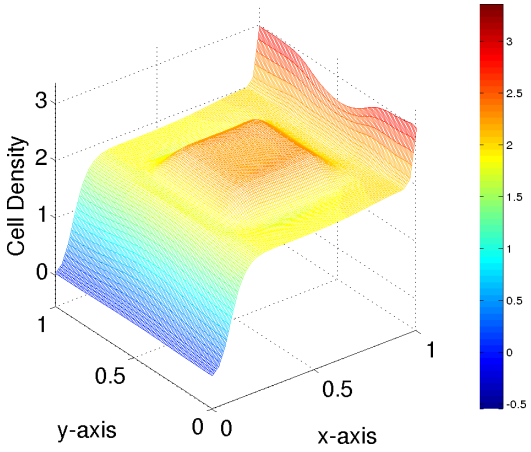

Figure 5.68 Cell density after 480 hours using $\delta/\epsilon = 3\times10^{-2}$ and original $\alpha = 0.001$ parameter values.

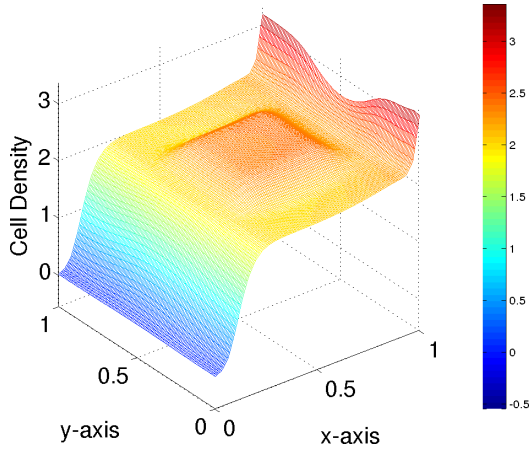

Figure 5.69 Cell density after 600 hours using $\delta/\epsilon = 3\times10^{-2}$ and original $\alpha = 0.001$ parameter values.

magnitude, shows little change relative to the results with the original parameter values; but Figures 5.66-5.69, where δ is increased slightly more than one more order of magnitude, shows significant damage to the cell population. With $\delta/\epsilon = 0.03$ the cell drag velocity is less than two orders of magnitude smaller than the fluid velocity itself, and cellular adhesion becomes very difficult. The cells are not only pulled to the downstream end of the domain, but as Figure 5.71 reveals, there is also a decrease in

the total cell population. This is likely due to a combination of reasons: once dragged along with the flow the cell population is confined to a small area, where there is more competition for the available nutrient. Moreover, the relatively high cell density in that small area indicates a low permeability, with consequent high shear stresses, possibly high enough to be in the damaging regime and slowing growth.

Figures 5.70 and 5.71 show the total cell population over time as the values of α and δ/ϵ (respectively) are changed. We see in Figure 5.70 that early in the simulation there is a slight up-tick in the cell population due to cells moving faster toward the region of growth factor for higher values of α, but by the end of the simulation the populations are all fairly equal. Our simulations at different α values lend credence to the concept of printing growth factor to control the final cell distribution, as Figures 5.54-5.57 and 5.58-5.61 indicate that there is a difference in the cell density distributions obtained depending on the strength of the haptotactic effect, even if the total population is unaffected (figure 5.70). Figure 5.71 confirms the assessment made after examining Figures 5.62-5.65 and 5.66-5.69, indicating that the highest drag velocity leads to a significant decrease in total cell density.

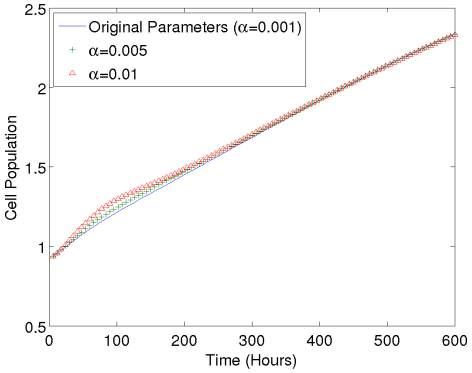

Figure 5.70 Total cell population over time for differing α values with $\delta/\epsilon = 10^{-5}$ unchanged.

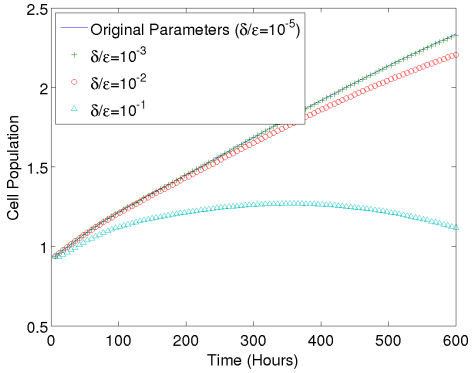

Figure 5.71 Total cell population over time for differing δ/ϵ values with $\alpha = 0.001$ unchanged.

5.5 Discussion

The experimental results of Miller *et al.* [28, 29], and our model results presented here, demonstrate that modifying scaffold properties locally, for example by inclusion of a growth factor that binds to the scaffold, can have a profound effect on the proliferation and final distribution of cells across the scaffold. Our model suggests that treating scaffolds with growth factor can increase the overall cell density distribution in regions of higher growth factor concentration, and can stimulate cell migration up growth factor gradients (haptotaxis). This effect can lead to results that differ significantly from the case where cells migrate under cellular diffusion and advection alone (see Figures 5.24-5.27 and 5.28-5.29). We have also demonstrated the clear potential for using different patterns of initial growth factor to create specific final distributions of cells within a scaffold: this is backed up by firm experimental evidence, e.g., [28, 29]. While only a few representative simulations are given in this chapter, for the purpose of illustration, when properly calibrated our model could in principle be used to predict the outcomes of many different experimental scenarios of initial cell seedings and growth factor distributions (within the limitations of our Darcy flow model and continuum approximation for the cell density). We believe that the results presented here are promising, and suggest that further experimental investigation of the haptotactic effects of growth factor in tissue engineering scaffolds is worthwhile. Work presented in this chapter is to be published in a forthcoming paper [40].

CHAPTER 6

CYCLIC SCAFFOLD COMPRESSION

6.1 Introduction

Modeling and simulation of loading on the tissue engineering construct can potentially provide significant insight into the effects that stress and/or strain plays in chondrocyte proliferation. Some progress has been made in this direction (for example, the finite-element studies of Babalola and Bonassar [2] and Moo *et al.* [30]); but a unified macroscopic model that treats the entire construct under forced perfusion and cyclic loading is lacking. In this chapter, we take a step towards this goal by modifying the original model to account also for cyclic loading of the scaffold. The first modification is to the fluid flow, where we now allow for the possibility of pulsatile pressure boundary conditions. Furthermore, to mimic the cyclic compression the permeability is assumed to vary periodically in time. As noted above, the cyclic loading is known to influence many experimental variables: we focus here on its effect within the constraints of the simple model outlined in this paragraph – that is, its effect via shear fluid stress modification – comparing with the unloaded case. When compared against experimental outcomes, this can provide some indication of the importance of factors omitted from our model, such as up-regulation of genetic markers under cyclic loading [44].

We analyze the model on two different timescales. The cyclic loading and the fluid pressure vary on a short timescale, driving the flow, while cell proliferation occurs on a much longer timescale. While nutrient is transported by advection and diffusion within the fluid, with advection dominating, we will consider the case in which a constant external fresh supply keeps the construct well-nourished. This approximation, justified in more detail in §6.3, enables us to average over an arbitrary

loading cycle to obtain the long-time evolution of the cells in terms of cycle-averaged flow quantities. Thus, we will be able to use a short timescale average of the fluid flow, which removes all short timescale dependence, and see its effects on cell proliferation on the longer timescale.

In this chapter, we present an alternate nondimensionalization of the model, and an asymptotic analysis that reveals the separation of physical effects into the two distinct timescales. This analysis is followed by the short timescale period averaging, to derive a model valid on the long timescale of cell proliferation. We then present some sample numerical results to demonstrate the time-averaged model, and compare it with the original model of Chapter 3.

6.2 Nondimensionalization

We wish to model the effects of a periodic compressive force on the scaffold, which, since it drives flow, necessarily occurs on the same timescale as the fluid velocity. To achieve this, the time, pressure (and by extension the fluid velocity), and permeability nondimensionalizations are slightly changed. Their new nondimensionalizations are as follows:

$$t^* = \frac{\tilde{t}}{\omega^*} = \frac{T}{\lambda^*} \tag{6.1}$$

$$\boldsymbol{u}^* = u_0^* \boldsymbol{u} = L^* \omega^* \boldsymbol{u},\ p^* = \frac{\mu^* L^* u_0^*}{k_s^*} p = \frac{\mu^* {L^*}^2 \omega^*}{k_s^*} p \tag{6.2}$$

$$k^*(c^*, t^*) = k_s^* k(c; \tilde{t}, T) \tag{6.3}$$

where $2\pi/\omega^*$ is the period of cyclic loading, $\tilde{t}$ is the short timescale (on the order of fluid flow), and T is the long timescale (on the order of cell proliferation). We assume (see Table 3.4) that $\epsilon = \lambda^*/\omega^* \equiv L^*\lambda^*/u_0^* \ll 1$.

6.2.1 Nutrient Concentration

Dividing equation (2.4) through by $\omega^* n_0^*$ yields the dimensionless form of the nutrient equation

$$\frac{\partial n}{\partial \tilde{t}} + \boldsymbol{u} \cdot \nabla n = D\nabla^2 n - \theta g(n, c, \tau_s), \tag{6.4}$$

where $D = D^*/(\omega^* L^{*^2})$, and $\theta = (\theta^* c_0^*)/(\omega^* n_0^*)$ with approximate dimensional parameter values defined in Table 3.3.

6.2.2 Cell Density

Similarly to the nutrient equation, we divide the cell density equation (2.7) through by $\omega^* c_0^*$ to obtain the dimensionless form of the cell density equation

$$\frac{\partial c}{\partial \tilde{t}} + \epsilon d \boldsymbol{u}_p \cdot \nabla c = \epsilon D_c \nabla^2 c + \epsilon g(c, n, \tau_s) - \epsilon \nu c, \tag{6.5}$$

where $\epsilon = \lambda^*/\omega^* \ll 1$, $d = \delta/\epsilon$, $D_c = D_c^*/(\lambda^* L^{*^2})$, $\nu = \nu^*/\lambda^*$, and $d, D_c, \nu, g(c, n, \tau_s) \leq \mathcal{O}(1)$ with respect to ϵ (see Table 3.3). The dimensionless pore velocity is related to the Darcy velocity by $\boldsymbol{u}_p = \boldsymbol{u}/\phi$, where ϕ is the scaffold porosity.

6.2.3 Parameters

All of the dimensional parameters from the basic model are used in the cyclic compression model with the exception of n_0^*, where as will be presented shortly, a well nourished domain over the entire scaffold is assumed. We set $\omega^* = 1\text{s}^{-1}$, and so that the results are comparable to the results from the basic model we reduce the pump flow velocity presented in Table 3.3 by a factor of five. As a result of the alternative scalings, the dimensionless parameters are slightly different, and they are presented in Table 6.1. The cell drag velocity coefficient, $d = \delta/\epsilon$, is set equal to 10^{-3} for the cyclic compression simulations to accentuate the effect of loading.

Table 6.1 Dimensionless Parameter Values for the Cyclic Loading Model

Parameter	Formula	Value
D	$D^*/(\omega^* L^{*^2})$	2.6×10^{-6}
θ	$(\theta^* c_0^*)/(\omega^* n_0^*)$	Assumed $\mathcal{O}(\epsilon)$
D_c	$D_c^*/(\lambda^* L^{*2})$	4.32×10^{-4}
ν	ν^*/λ^*	0.1425
ϵ	λ^*/ω^*	4.63×10^{-7}

6.3 Asymptotic Analysis

We seek solutions to equations (3.1), (3.2), and (6.4)-(6.5) as asymptotic expansions in terms of the small parameter ϵ. This is done to exploit the two well-separated timescales to be investigated: the short timescale $t = \tilde{t}$, based on the loading period, and the long timescale $T = \epsilon\tilde{t}$, on which cell proliferation occurs. We assume asymptotic expansions in the form of

$$c(\boldsymbol{x}; t, T) = c_0(\boldsymbol{x}; t, T) + \epsilon c_1(\boldsymbol{x}; t, T) + \cdots, \tag{6.6}$$

(and similarly for other dependent variables) where all c_i are functions of space and both time variables. Note that, since $t = \tilde{t} = T/\epsilon$, we have

$$\frac{\partial}{\partial \tilde{t}} c(\boldsymbol{x}; t, T) = \frac{\partial c}{\partial t} + \epsilon \frac{\partial c}{\partial T}. \tag{6.7}$$

6.3.1 Leading Order Nutrient Concentration: Well-Nourished Limit

The values estimated in Table 6.1 suggest that $D = \mathcal{O}(\epsilon)$ and we assume additionally that nutrient concentration in the culture medium is sufficiently high that $\theta = \mathcal{O}(\epsilon)$. In this case the leading order nutrient concentration equation is just

$$\frac{\partial n_0}{\partial t} + \boldsymbol{u}_0 \cdot \nabla n_0 = 0. \tag{6.8}$$

If we assume further that the external nutrient supply is held constant, even over the long timescale, then the solution to this equation is just $n_0 = \text{constant} = 1$, with our assumed scaling.

6.3.2 Leading Order Cell Density

Inserting the asymptotic expansion for the cell density, equation (6.6), into the leading order cell density equation, (6.5), and using our two-timescale assumption, we obtain at leading order

$$\frac{\partial c_0}{\partial t} = 0. \tag{6.9}$$

Thus we see that the leading order cell density is unchanged on the short timescale, but may vary on the long timescale. At $\mathcal{O}(\epsilon)$ we obtain

$$\frac{\partial c_1}{\partial t} + \frac{\partial c_0}{\partial T} + d\boldsymbol{u}_{p_0} \cdot \nabla c_0 = D_c \nabla^2 c_0 + g(n_0 = 1, c_0, \tau_s) - \nu c_0 \tag{6.10}$$

where the leading order pore velocity $\boldsymbol{u}_{p_0} = \boldsymbol{u}_0/\phi$, with ϕ the scaffold porosity. We now have one equation with two dependent variables, c_0 and c_1. In §6.3.4 we will eliminate c_1 from the equation giving us one equation with one dependent variable.

6.3.3 Leading Order Fluid Flow

The fluid flow (Darcy) velocity is obtained by solving an elliptic PDE for the pressure p, which depends on the scaffold permeability

$$\nabla \cdot (k(c,t)\nabla p) = 0, \quad k(c,t) = (1 + \Delta \cos t)\tilde{k}(c), \tag{6.11}$$

which we solve subject to no-flux conditions at boundaries $y = 0, 1$ and specified flow conditions at $x = 0, 1$. The form of the permeability used in equation (6.11) contains both spatial and (periodic) temporal dependence; the latter models the effects of the cyclic compression. We have seen that cell proliferation occurs only over

the long timescale, so the cell density dependent permeability $\tilde{k}(c)$ is automatically constant over the short time. To simulate the cyclic compression of the scaffold we have included a 2π-periodic variation on the short timescale $t = \tilde{t}$. Here, $\Delta < 1$ is a coefficient measuring the degree of compression of the scaffold; for most of our simulations we take $\Delta = 0.2$. With the appropriate asymptotic expansions for cell density and pressure, the leading order Darcy's Law and incompressibility equations are

$$\boldsymbol{u}_0 = -(1 + \Delta \cos t)\tilde{k}(c_0)\nabla p_0 \tag{6.12}$$

$$\nabla \cdot \boldsymbol{u}_0 = 0 \;\Rightarrow\; \nabla \cdot (\tilde{k}(c_0)\nabla p_0) = 0. \tag{6.13}$$

Since the permeability is 2π-periodic in t, we may assume the leading order velocity $\boldsymbol{u}_0$ and pressure p_0 are also. We consider unidirectional flow driven by a prescribed (dimensionless) flux Q_0. This corresponds to some (unknown) pressure drop Π_0 between $x = 0$ and $x = 1$ across the scaffold. We solve (6.12) and (6.13) by exploiting the linearity: Let $\tilde{p}$ be the specific solution of the elliptic PDE (6.13) satisfying no-flux conditions at $y = 0, 1$ and with a unit pressure drop in x:

$$\tilde{p}(0, y, t) = 1, \quad \tilde{p}(1, y, t) = 0. \tag{6.14}$$

Clearly, p_0 and $\tilde{p}$ are related by $p_0 = \Pi_0 \tilde{p}$. The prescribed flux Q_0 satisfies

$$Q_0 = -\int_0^1 (1 + \Delta \cos t)\tilde{k}(c_0) \left.\frac{\partial p_0}{\partial x}\right|_{x=0} dy = \Pi_0 \tilde{Q}_0 (1 + \Delta \cos t), \tag{6.15}$$

where $\tilde{Q}_0 = -\int_0^1 \tilde{k}(c_0) \left.\frac{\partial \tilde{p}}{\partial x}\right|_{x=0} dy$ can be evaluated from the solution $\tilde{p}$. Hence, $\Pi_0 = Q_0/(\tilde{Q}_0(1 + \Delta \cos t))$ from which we recover

$$p_0 = \frac{Q_0 \tilde{p}}{\tilde{Q}_0(1 + \Delta \cos t)}, \tag{6.16}$$

and thus

$$\boldsymbol{u}_0 = -\frac{Q_0}{\tilde{Q}_0}\tilde{k}(c_0)\nabla\tilde{p}. \tag{6.17}$$

If the imposed dimensionless flux Q_0 is constant we may set it to 1. Alternatively, we may consider an imposed flux Q_0 that is also 2π-periodic,

$$Q_0 = 1 + A\cos t, \tag{6.18}$$

for some prescribed amplitude A.

6.3.4 Period Averaging

We observe that on the short (t) timescale the leading order cell density c_0 is independent of t, as is the nutrient concentration n_0, while the permeability k, porosity ϕ, fluid velocities $\boldsymbol{u}_0$, $\boldsymbol{u}_{p_0}$ and pressure p_0 are 2π-periodic. It follows that the shear stress τ_s within the scaffold is also 2π-periodic. Hence, in equation (6.10), the $\mathcal{O}(\epsilon)$ cell density c_1 must also be 2π-periodic. We may therefore average this equation over an arbitrary loading period,

$$\begin{aligned}\frac{1}{2\pi}\int_{t_0}^{t_0+2\pi}\left(\frac{\partial c_1}{\partial t} \;+\; \frac{\partial c_0}{\partial T} + d\boldsymbol{u}_{p_0}\cdot\nabla c_0\right)dt = \\ = \;\frac{1}{2\pi}\int_{t_0}^{t_0+2\pi}\left(D_c\nabla^2 c_0 + g(n_0=1,c_0,\tau_s) - \nu c_0\right)dt,\end{aligned} \tag{6.19}$$

yielding (using the above observations)

$$\frac{\partial c_0}{\partial T} + d\overline{\boldsymbol{u}_{p_0}}\cdot\nabla c_0 = D_c\nabla^2 c_0 + \overline{g(n_0=1,c_0,\tau_s)} - \nu c_0, \tag{6.20}$$

where the overbars denote the 2π average of the quantity, so

$$\overline{\boldsymbol{u}_{p_0}} = \frac{1}{2\pi}\int_0^{2\pi}\boldsymbol{u}_{p_0}(\boldsymbol{x},t)dt, \quad \overline{g(n_0,c_0,\tau_s)} = \frac{1}{2\pi}\int_0^{2\pi} g(n_0=1,c_0,\tau_s)dt, \tag{6.21}$$

where $\boldsymbol{u}_{p_0} = \boldsymbol{u}_0/\phi$ is calculated using (6.17) with (6.11) and (2.21); and the pressure p calculated using (6.16). We solve this model again subject to a specified initial

seeding density, and no-flux conditions at the four scaffold boundaries. With total dimensionless cell flux defined as

$$\boldsymbol{J}_c = d\boldsymbol{u}_{p_0} c_0 - D_c \nabla c_0 \tag{6.22}$$

we therefore impose $\boldsymbol{J}_c \cdot \hat{\boldsymbol{n}} = 0$ at $x = 0, 1,\ y = 0, 1$, where $\hat{\boldsymbol{n}}$ denotes the outward normal to the scaffold boundary.

6.4 Results

We present sample numerical results from our model for a selection of different initial cell-seedings. For all initial seedings considered, the surface plots of results are qualitatively similar for all loading scenarios, therefore we only show the cell density evolution for a chosen loading scenario, followed by plots comparing total final cell yield for all loading protocols.

6.4.1 Uniformly-Seeded Scaffold

We first consider the case most commonly aspired to in experiments: a uniform initial cell seeding. Figures 6.1 and 6.2 show selected results from a simulation where a uniformly-seeded scaffold is subjected to cyclic loading that induces a time variation in the permeability given by (6.11), with $\Delta = 0.2$, and to an imposed flux with time-dependent oscillatory component given by (6.18), with $A = 0.5$ (we may think of Δ as some measure of scaffold compression). In those figures we see snapshots of the cell density after 240 and 600 hours of perfusion plus loading, respectively; while Figure 6.3 shows the total cell population as a function of time for several different loading scenarios, characterized by changing parameters Δ and A. The case with no cyclic loading, where no cycle-averaging process is required, is simply the original model presented and is referred to as "Regular Darcy Model" in this and subsequent figures.

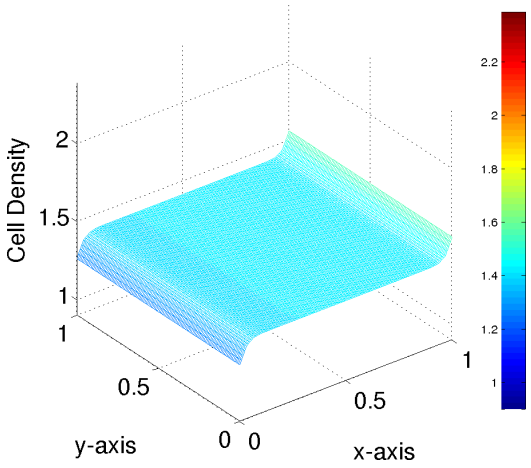

Figure 6.1 Cyclic compression from a uniform initial seeding model with parameter values $\Delta = 0.2$, $A = 0.5$ after 240 hours.

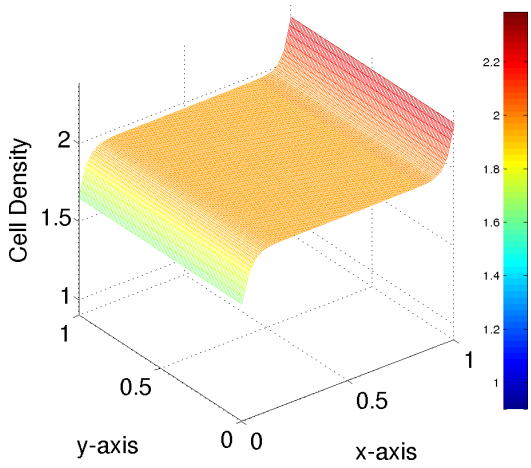

Figure 6.2 Cyclic compression from a uniform initial seeding model with parameter values $\Delta = 0.2$, $A = 0.5$ after 600 hours.

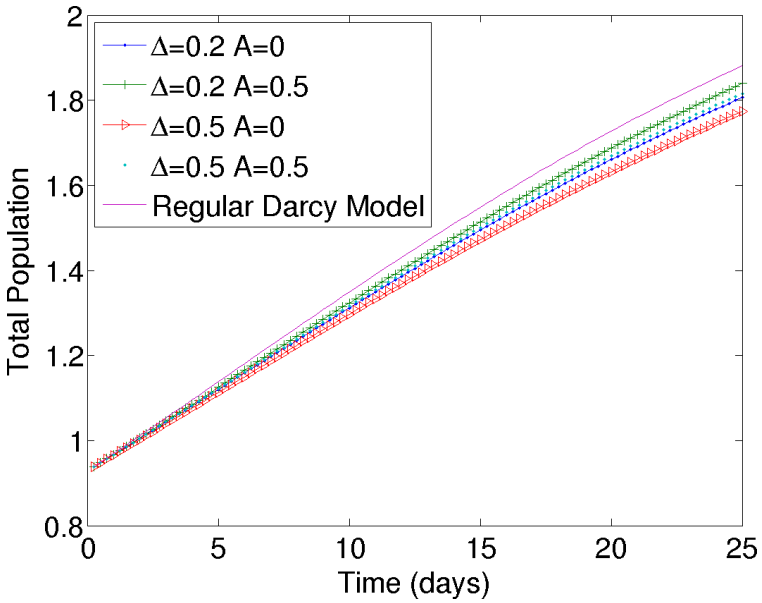

Figure 6.3 Cyclic compression from a uniform initial seeding total cell populations for basic model and varying Δ and A values.

Unsurprisingly, the evolution of the cell density profile in this case is not dramatic. The cell density evolves in a fairly uniform manner, but with lower densities towards the flow inlet ($x = 0$) and higher densities towards the outlet ($x = 1$). These

features are most easily seen in the surface plots shown in Figures 6.4-6.7, where the cell densities at the final time are compared for all loading protocols. These gradients near the inlet and outlet are present in all simulations, including those for the case without cyclic loading; but broadly speaking, the higher the degree of cyclic loading, the more pronounced they are (they are much less pronounced in the unloaded case). They are probably largely attributable to the cellular advective drag, combined with our no flux condition on cells at the edges of the domain. Given the net flow direction this would certainly cause some pile-up of cells at the outlet, and a dwindling of cell numbers near the inlet.

Figure 6.3 shows that the total cell population over all loading scenarios tested is in fact greatest for the unloaded (regular Darcy model) case under the given flow conditions, although the differences are not great. This could be due to a combination of factors: though shear stresses are higher under the compressive part of the cycle (leading if sustained, unless excessively high, to enhanced proliferation rates), they are lower under the "expansion" phase of the cycle, so the net effect may nearly cancel.

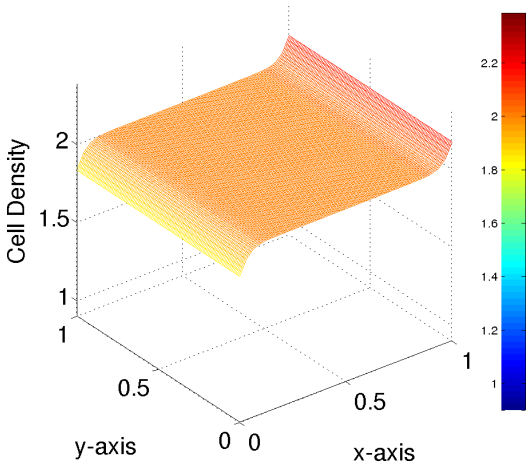

Figure 6.4 Surface plot at $t = 600$ hours for a uniform cell seeding with no load.

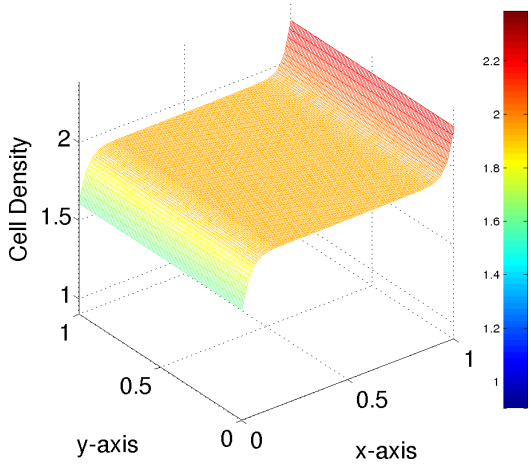

Figure 6.5 Surface plots at $t = 600$ hours for a uniform cell seeding with $\Delta = 0.2$, $A = 0$.

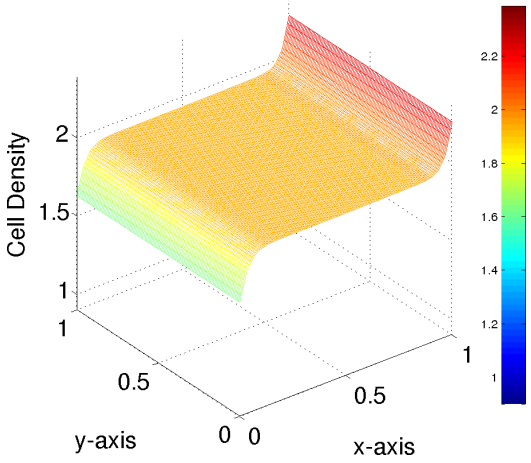

Figure 6.6 Surface plots at $t = 600$ hours for a uniform cell seeding with $\Delta = 0.5$, $A = 0.5$.

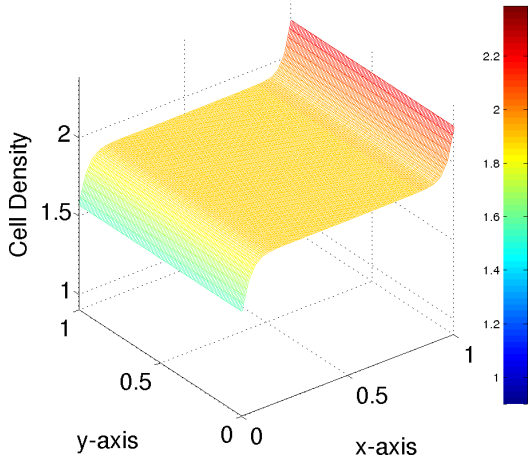

Figure 6.7 Surface plots at $t = 600$ hours for a uniform cell seeding with $\Delta = 0.5$, $A = 0$.

6.4.2 Peripherally-Seeded Scaffold

As previously noted, achieving a uniform seeding right through to the center of the scaffold may be experimentally challenging and it may be easier to seed the scaffold from its periphery, and rely on the migration of cells into the interior to obtain the end result. Figures 6.8-6.9 show a simulation where a linear gradient of cell density (in the direction normal to the wall) is imposed at each of the four scaffold walls

first presented in Figure 4.30 in Chapter 4. The seeded scaffold is subjected to cyclic loading that induces a time-dependent permeability given by (6.11), with $\Delta = 0.2$, and to an imposed flux with time-dependent oscillatory component given by (6.18), with $A = 0.5$.

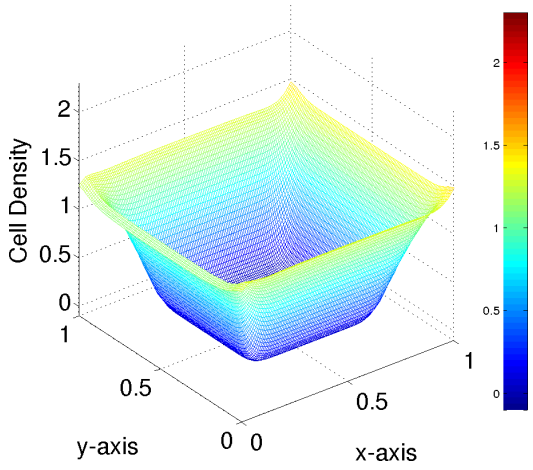

Figure 6.8 Cyclic compression from a peripheral initial seeding model with parameter values $\Delta = 0.2$, $A = 0.5$ after 240 hours.

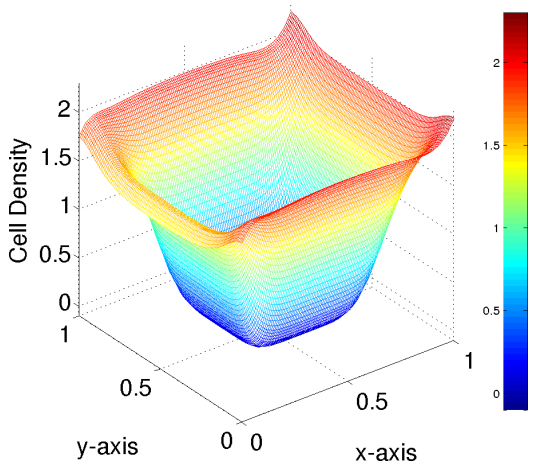

Figure 6.9 Cyclic compression from a peripheral initial seeding model with parameter values $\Delta = 0.2$, $A = 0.5$ after 600 hours.

Figure 6.10 shows a comparison of the results as the model loading parameters Δ and A are varied. The total cell yield as a function of time is plotted for different combinations of Δ and A, including for the unloaded case (Regular Darcy Model). Only fairly modest differences are seen; for this particular seeding scenario the regular Darcy model again gives the best total cell yield.

Figures 6.11-6.14 show the final-time ($t = 600$ hours) cell density profiles for different loading scenarios. The surface plots reveal that the final cell distributions for all loaded cases are very similar; but the unloaded case shows qualitative differences, particularly near the flow outlet.

The following two seeding distributions are less realistic, but serve to give some indication of how changing the initial cell seeding affects the final outcome.

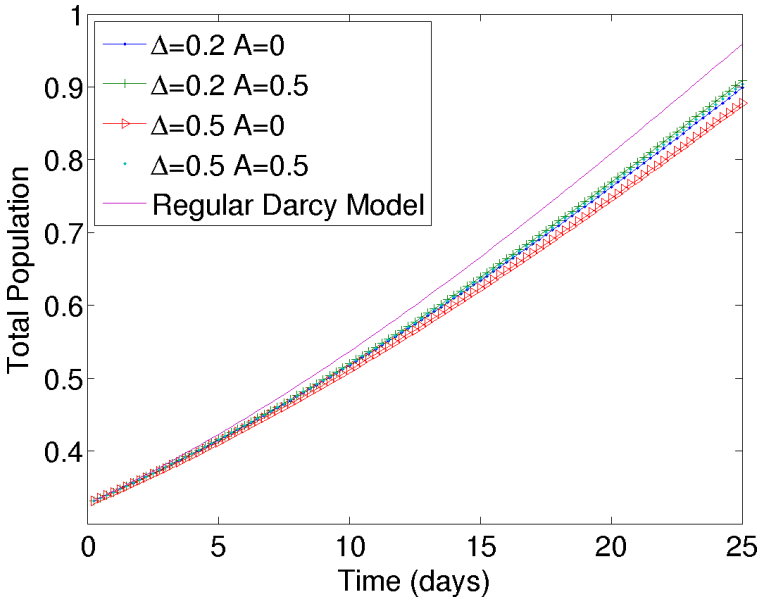

Figure 6.10 Cyclic compression from a peripheral initial seeding total cell populations for basic model and varying Δ and A values.

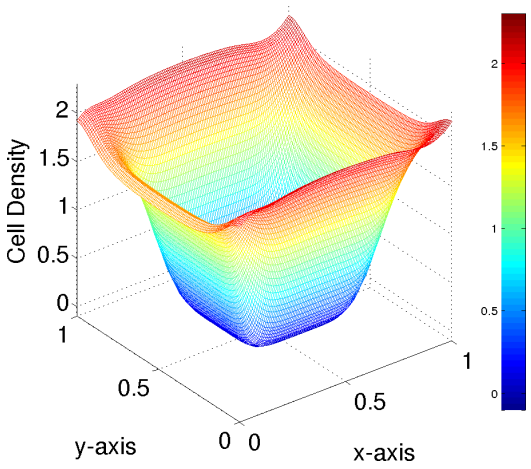

Figure 6.11 Surface plot at $t = 600$ hours for a peripheral cell seeding with no load.

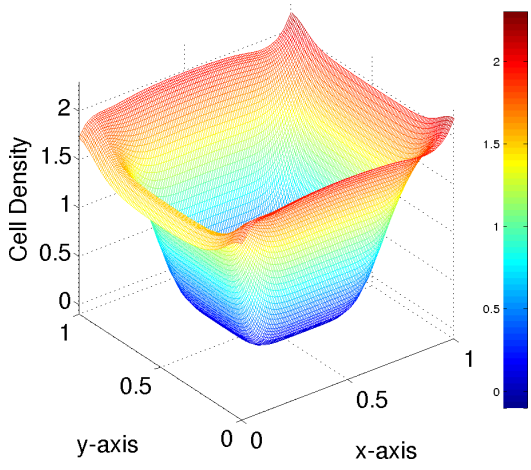

Figure 6.12 Surface plots at $t = 600$ hours for a peripheral cell seeding with $\Delta = 0.2$, $A = 0$.

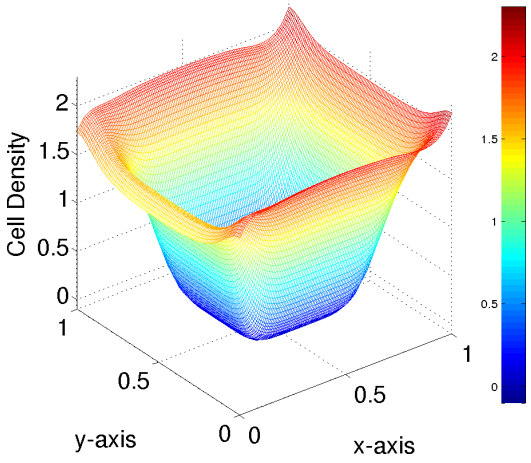

Figure 6.13 Surface plots at $t = 600$ hours for a peripheral cell seeding with $\Delta = 0.5$, $A = 0.5$.

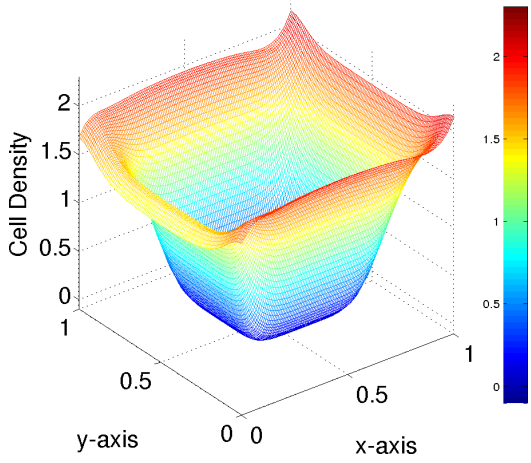

Figure 6.14 Surface plots at $t = 600$ hours for a peripheral cell seeding with $\Delta = 0.5$, $A = 0$.

6.4.3 Centrally-Seeded Scaffold

As a comparison, we next consider a scaffold that is seeded only at its center. Figures 6.15-6.16 show snapshots of the cell density evolution over time for the same parameters as considered previously, together with the comparison plot showing the total cell yield over time (Figure 6.17) for the different loading scenarios. Once more the unloaded model wins out in terms of the final cell yield, all other loading scenarios giving very similar, slightly lower, yields.

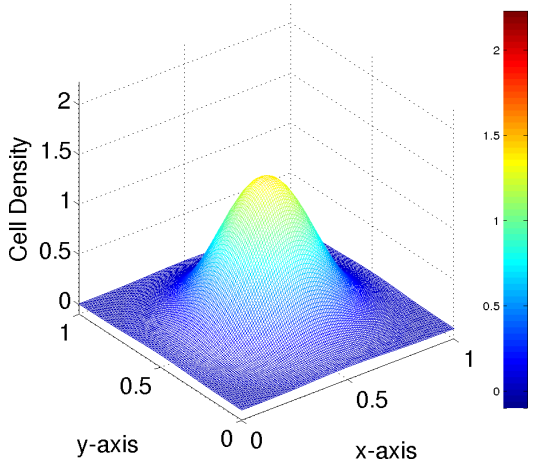

Figure 6.15 Cyclic compression from a central initial seeding model with parameter values $\Delta = 0.2$, $A = 0.5$ after 240 hours.

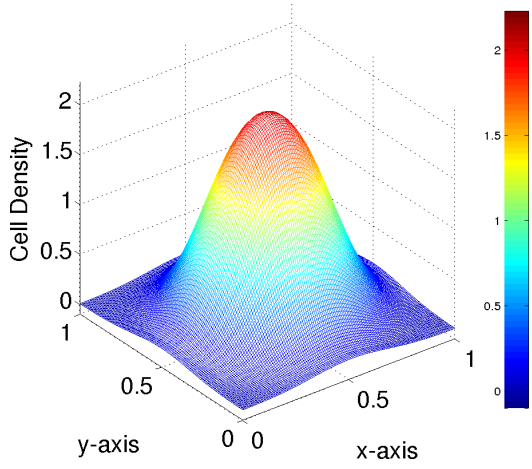

Figure 6.16 Cyclic compression from a central initial seeding model with parameter values $\Delta = 0.2$, $A = 0.5$ after 600 hours.

For this case the final cell density surface plots are all qualitatively very similar: as we saw in the previous examples, the main differences in cell density appear at the edges of the scaffold, and here all cell densities remain relatively low at the edges, even after 600 hours. Hence, we do not show the final surface plots for this initial seeding scenario.

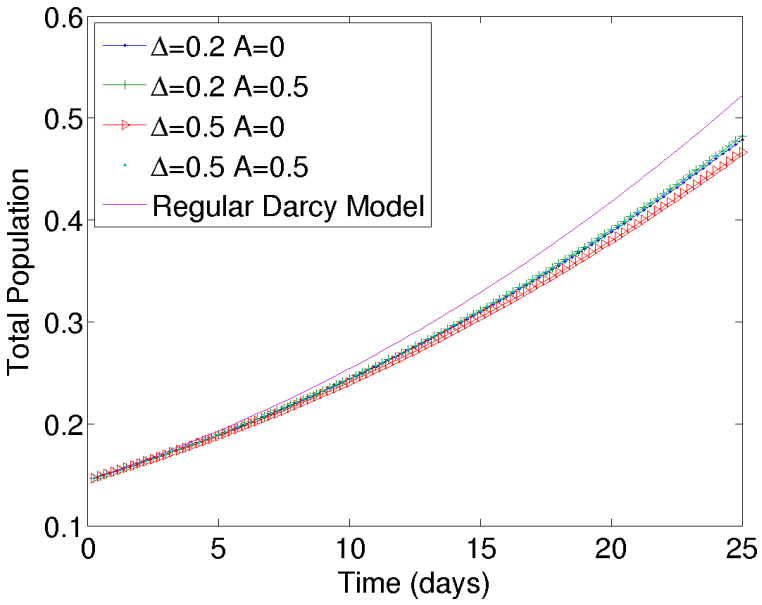

Figure 6.17 Cyclic compression from a central initial seeding total cell populations for basic model and varying Δ and A values.

6.4.4 Sinusoidal Initial Seeding

We next consider a scaffold that is seeded nonuniformly according to

$$c_0(x, y, 0) = 1 + \frac{1}{2}\sin 6x + \frac{1}{2}\cos 6y \tag{6.23}$$

Here the initial nonuniformities in the cell density smooth out gradually in time (though not entirely). Figures 6.18-6.19 show the usual snapshots from the evolution of a case with loading and pulsatile flow, with Figure 6.20 showing the comparison of total cell yield over time for both loaded and unloaded cases. This is the first example in which loading gives rise to a higher total yield (the case illustrated in figures 6.18 and 6.19 actually gives the highest total yield).

Figures 6.21-6.24 show the surface plots of cell density for the final time $t = 600$ hours for the different loading scenarios. Again, the principal difference appears between the unloaded case and the others (all loading scenarios are qualitatively rather similar).

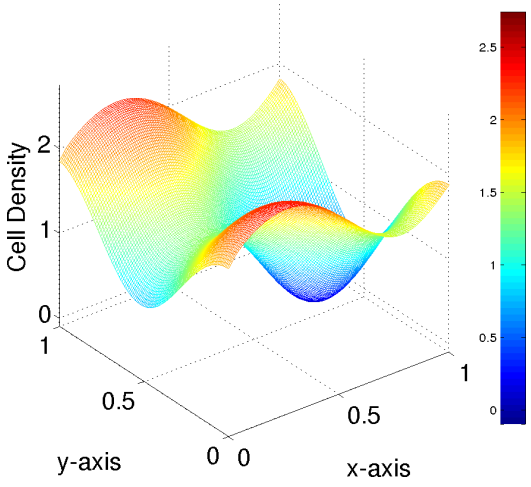

Figure 6.18 Cyclic compression from a sinusoidal initial seeding model with parameter values $\Delta = 0.2$, $A = 0.5$ after 240 hours.

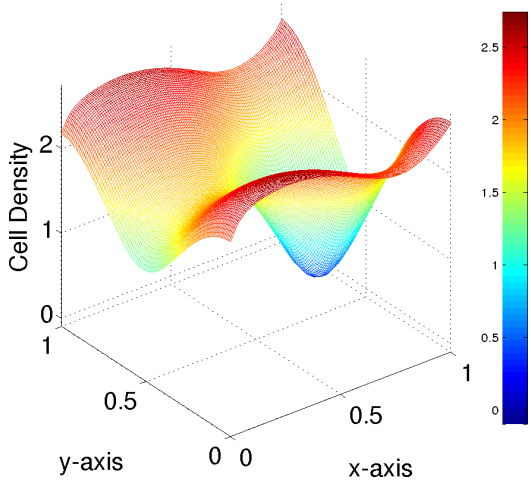

Figure 6.19 Cyclic compression from a sinusoidal initial seeding model with parameter values $\Delta = 0.2$, $A = 0.5$ after 600 hours.

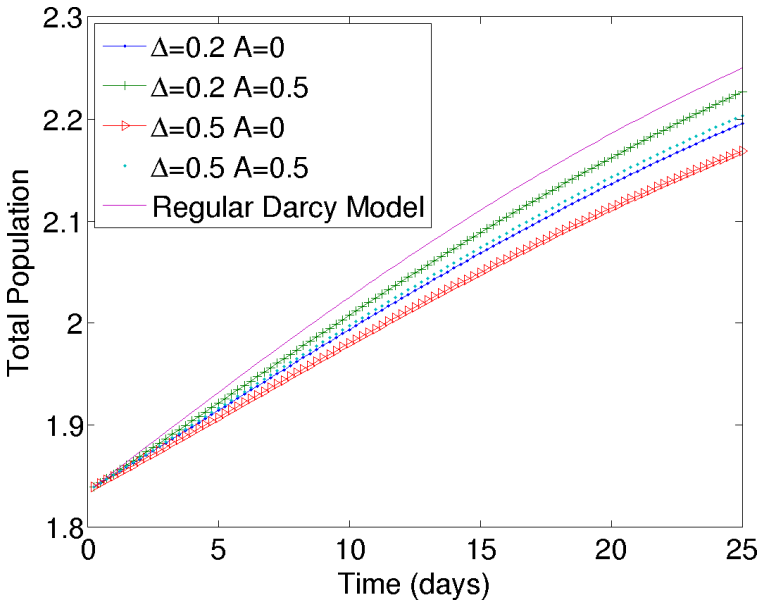

Figure 6.20 Cyclic compression from a sinusoidal initial seeding total cell populations for basic model and varying Δ and A values.

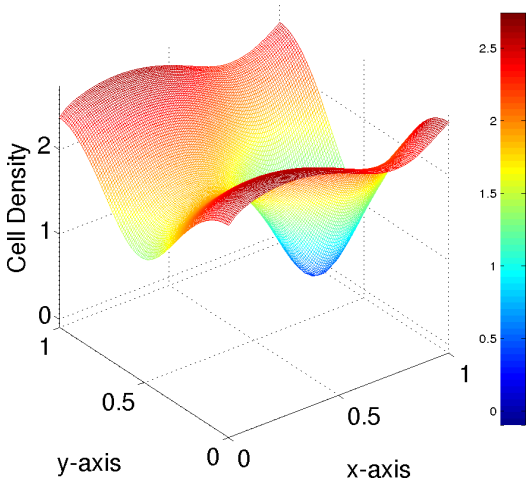

Figure 6.21 Surface plot at $t = 600$ hours for a sinusoidal cell seeding with no load.

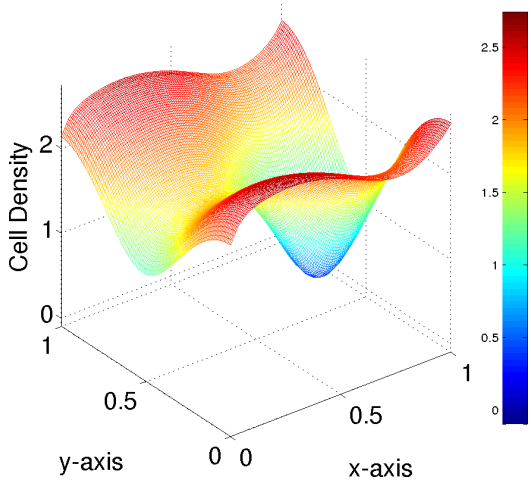

Figure 6.22 Surface plots at $t = 600$ hours for a sinusoidal cell seeding with $\Delta = 0.2$, $A = 0$.

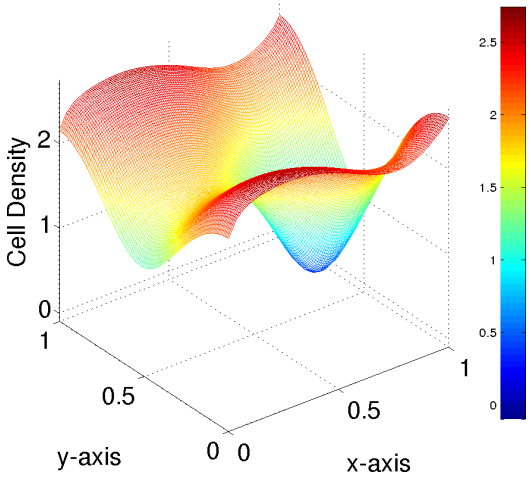

Figure 6.23 Surface plots at $t = 600$ hours for a sinusoidal cell seeding with $\Delta = 0.5$, $A = 0.5$.

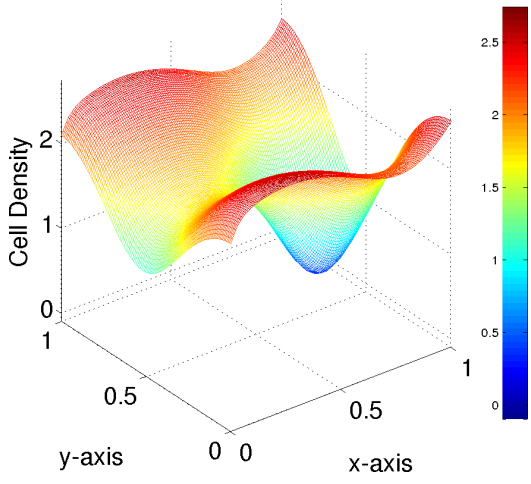

Figure 6.24 Surface plots at $t = 600$ hours for a sinusoidal cell seeding with $\Delta = 0.5$, $A = 0$.

6.5 Discussion

We have presented a minimal model for the proliferation of cells (e.g., chondrocytes) under cyclic loading and periodic pulsatile flow. Since the loading occurs on a timescale very much shorter than that of cellular proliferation, a two-timescale analysis together with period-averaging is exploited to derive a closed-form model for the evolution of cell density over the long timescale of proliferation. The model is very simple in that the effect of the loading is captured only by its effect on the fluid dynamics and the shear stress, which affects the local proliferation rate. No attempt is made to model other mechanotransductive effects due to the loading, such as upregulation of cellular genetic markers, which may impact the long-term proliferation and functionality of the tissue. Our model therefore investigates the hypothesis that differences in final outcomes under loading are due only to the altered fluid dynamics and shear stresses, assuming that these impact proliferation in the same way as in an "unloaded" model.

The model was simulated for several different loading scenarios, and compared to results with no loading, for a selection of different initial cell seedings. Though the final pattern of cells within the scaffold shows qualitative differences in the loaded versus unloaded cases, the final cell yields show only modest differences (our model can say nothing about functionality of the final tissue in different cases). This finding, when considered alongside experimental evidence demonstrating that loading can lead to profound differences in the final outcomes (e.g., Buschmann *et al.* [4]), suggests that in fact the key effects of loading are deeper than this model can capture, and that specific account must be taken of additional cell biology.

That said, there are clear differences between loaded and unloaded cases, which may be seen in Figures 6.4-6.7, 6.11-6.14, and 6.21-6.24. While all loading scenarios lead to very similar final outcomes, the cell distribution in the unloaded case differs noticeably at the flow outlet, $x = 1$, the cell density being consistently lower than

in any comparable loaded case. We attribute this feature primarily to the effects of cellular advection near the boundaries.

CHAPTER 7

OTHER EXTENSIONS TO THE MODEL

7.1 Introduction

We have shown that the model is able to simulate several different modeling scenarios, as presented in Chapters 4 through 6. There is clearly considerable scope for further extending the model in a number of directions to make it more realistic. In this chapter, we briefly outline two possible extensions on which we have carried out preliminary studies: (i) non-constant cellular death rate, reflecting the fact that the cells' local environment can affect this; and (ii) variable-permeability scaffolds, which can serve as another means of controlling the final outcome of an experiment. (In this direction the work of Shakeel et al. [46], which considers the effect of permeability "channels" through the scaffold to enhance nutrient delivery to the center, is relevant.)

7.2 Variable Death Rate

Typically experimentalists and modelers both treat cell death as a constant because determining an appropriate rate on the cellular level can be difficult. It is easier to determine the cell population at two points in time and calculate an average death rate over the course of an experiment or simulation. There are many ways that we can modify the death rate to reflect the local environment; e.g., as a function of the local cell density, a function of time, or a function of the local fluid velocity. In this section, we consider just one of these options: we make the death rate a function of the local fluid velocity, primarily to reflect the fact that cells release toxic by-products, which would normally be flushed away quickly by the fluid flow. In stagnant zones, however, toxins may build up, and lead to a higher death-rate. We, therefore, choose

to model the variable death rate as

$$\upsilon(\boldsymbol{u}) = \nu\left(\frac{\nu_0}{\nu_1 + \nu_2|\boldsymbol{u}|^2} + 1\right), \tag{7.1}$$

where ν_0, ν_1, and ν_2 are constants. This functional form is chosen so that as the fluid flow approaches 0 the death rate is a constant multiple of the prescribed death rate, $\nu(\nu_0/\nu_1 + 1)$, and as $\boldsymbol{u} \to \infty$ the death rate approaches the prescribed death rate, ν. Figure 7.1 shows this relationship with three choices for the constants.

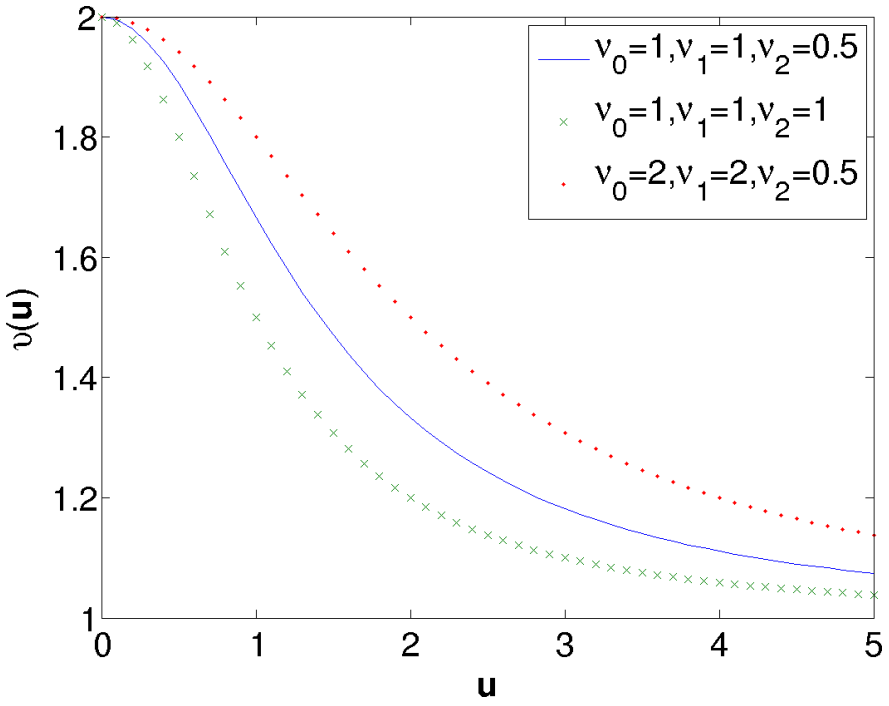

Figure 7.1 Differences in the variable death rate for choices of constants $\{\nu_0 = 1,\ \nu_1 = 1,\ \nu_2 = 0.5\}$, $\{\nu_0 = 1,\ \nu_1 = 1,\ \nu_2 = 1\}$, and $\{\nu_0 = 2,\ \nu_1 = 2,\ \nu_2 = 0.5\}$.

All three possible sets of parameters proposed have the effect of doubling the prescribed death rate when the fluid flow is small, an effect which will play a significant role in the results. We see that choice of constants does not greatly affect the relationship between $\boldsymbol{u}$ and $\upsilon(\boldsymbol{u})$ so we choose $\nu_0 = 1,\ \nu_1 = 1,\ \nu_2 = 0.5$ in equation (7.1). We now present sample results comparing the original Darcy model

with the new variable death rate model for three different initial cell seeding densities. All model parameters used are as in Table 3.4.

7.2.1 Initial Cell Density Varying in x and y

We first present results with initial density varying in x and y, recalling equation (4.14)

$$c(x, y, 0) = 1 + \frac{1}{2}\sin 6x + \frac{1}{2}\cos 6y. \tag{7.2}$$

Figures 7.2 and 7.3 show the resulting cell densities after 240 hours, and Figures 7.4 and 7.5 show the densities after 600 hours. The results show that the initial seeding

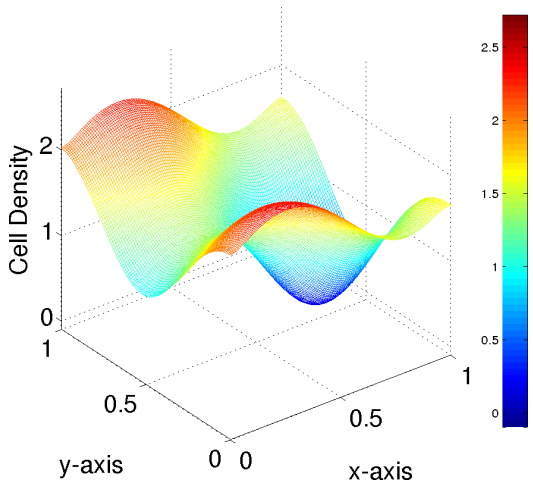

Figure 7.2 Cell density after 240 hours from a sinusoidal initial seeding from equation (4.14) with a constant death rate.

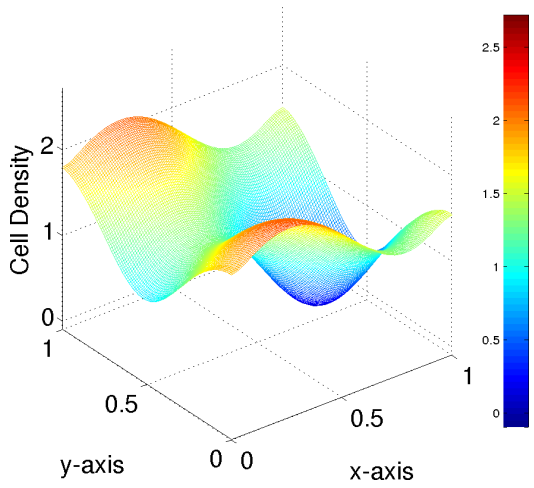

Figure 7.3 Cell density after 240 hours from a sinusoidal initial seeding from equation (4.14) with a variable death rate.

density stays close to the original model although the density everywhere for the variable death rate seems to be lower than in the original model. This result is further seen when examining the total cell population for both simulations, seen in Figure 7.6. This is unsurprising, since the variable death rate as chosen for these preliminary simulations is always greater than or equal to the constant death rate in the comparison simulation.

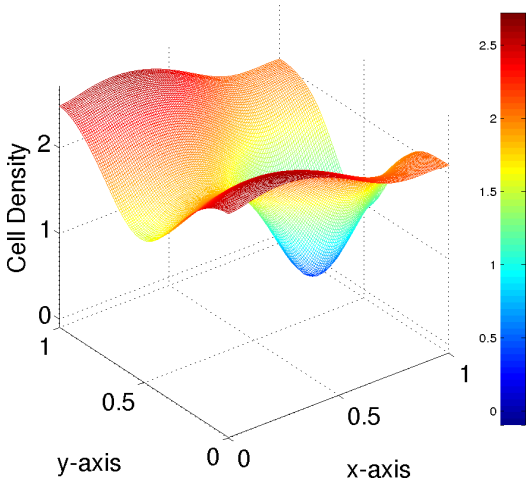

Figure 7.4 Cell density after 600 hours from a sinusoidal initial seeding from equation (4.14) with a constant death rate.

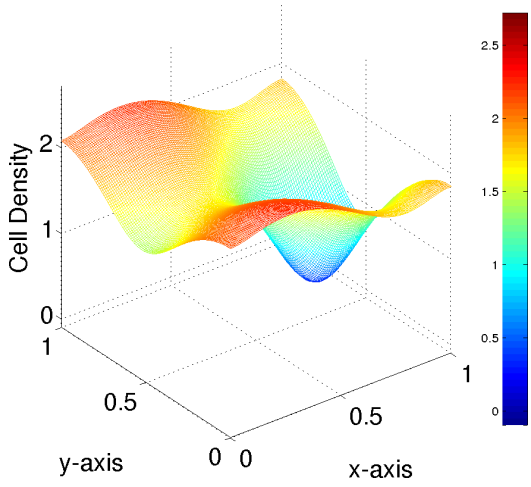

Figure 7.5 Cell density after 600 hours from a sinusoidal initial seeding from equation (4.14) with a variable death rate.

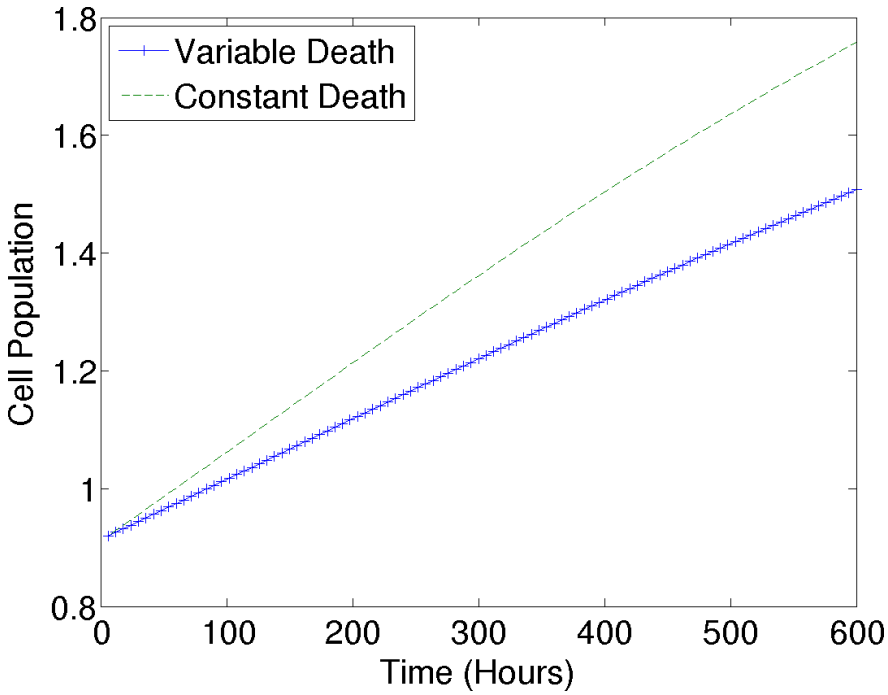

Figure 7.6 Total cell population comparing variable to constant death rates with sinusoidal initial seeding from equation (4.14).

7.2.2 Initial Cell Density Concentrated at Center of Scaffold

In this simulation, we compare the original model to one with a variable death rate when the initial cell seeding is concentrated in the center of the scaffold, originally presented in equation (4.15),

$$c(x, y, 0) = e^{-20\left(\left(x-\frac{1}{2}\right)^2+\left(y-\frac{1}{2}\right)^2\right)}.$$

Figures 7.7 and 7.8 show cell densities after 240 hours and Figures 7.9 and 7.10 show densities after 600 hours. The results similarly indicate little difference in

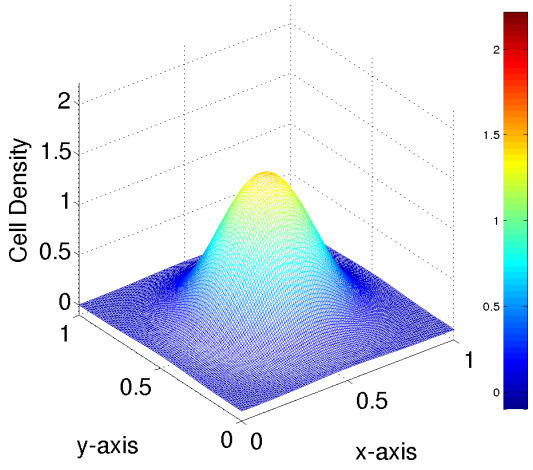

Figure 7.7 Cell density after 240 hours from a central initial seeding from equation (4.15) with a constant death rate.

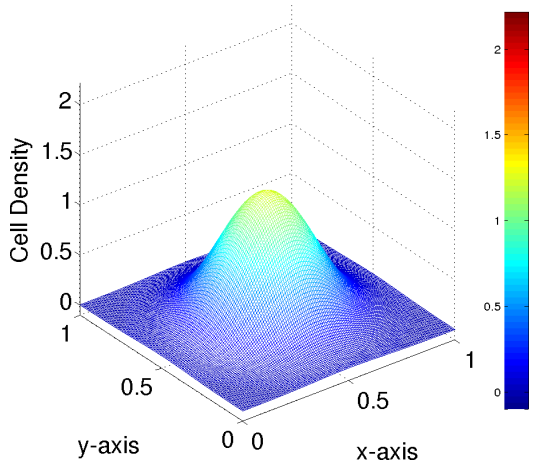

Figure 7.8 Cell density after 240 hours from a central initial seeding from equation (4.15) with a variable death rate.

the spatial form of the two models, but we can clearly see a reduction in the cell densities in the model with variable death when compared to the model with constant death. The area of the central cell density seems to be similar in both models and Figures 7.9 and 7.10 suggest that when variable death is included it decreases the rate of proliferation proliferation, particularly in those areas with the highest cell density. This is in line with our expectations: in these areas of high cell density, permeability is low and flow is slowed, so that the death rate is higher in the modified model.

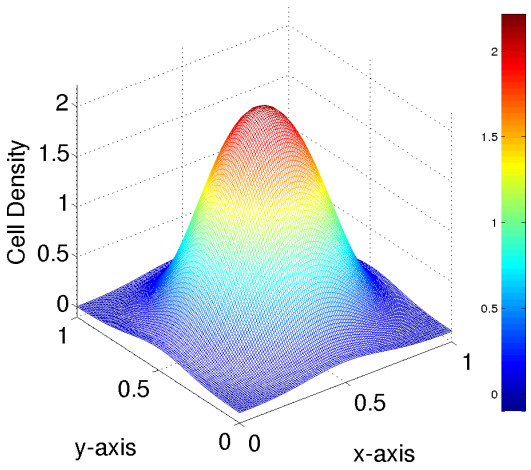

Figure 7.9 Cell density after 600 hours from a central initial seeding from equation (4.15) with a constant death rate.

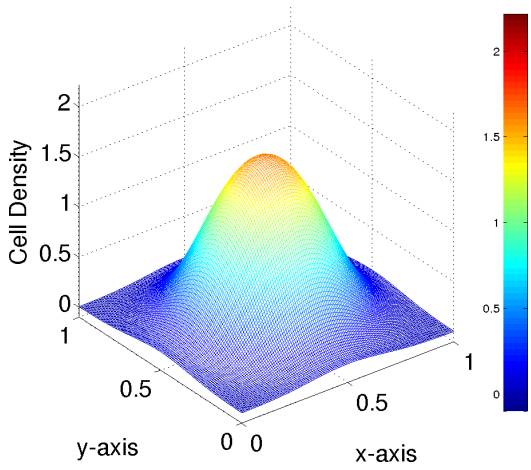

Figure 7.10 Cell density after 600 hours from a central initial seeding from equation (4.15) with a variable death rate.

Figure 7.11 shows the total cell population for this simulation, and it confirms the overall slowing of cell proliferation over time.

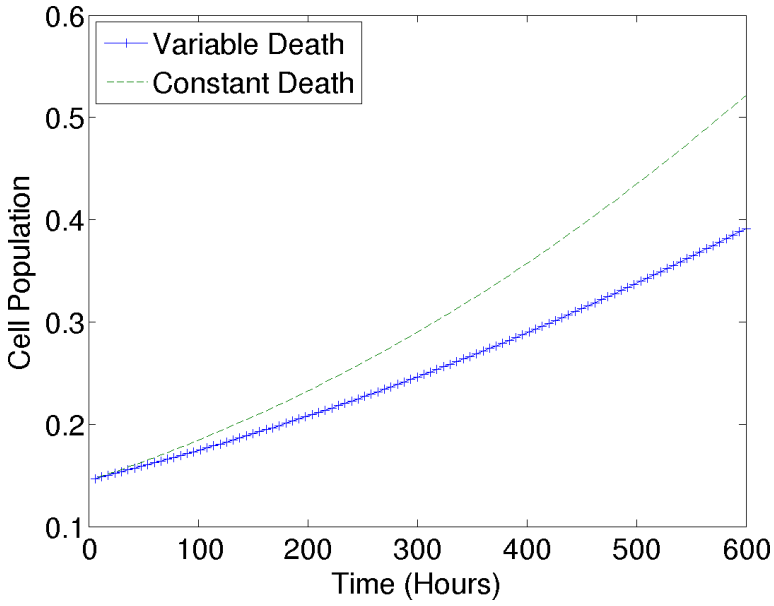

Figure 7.11 Total cell population comparing variable to constant death rates with central initial seeding from equation (4.15).

7.2.3 Initial Cell Density Around Periphery of Scaffold

The final set of simulated results are those where initially cells are seeded around the periphery of the scaffold. Figures 7.12 and 7.13 show cell densities after 240 hours and Figures 7.14 and 7.15 after the full simulation of 600 hours. We see again

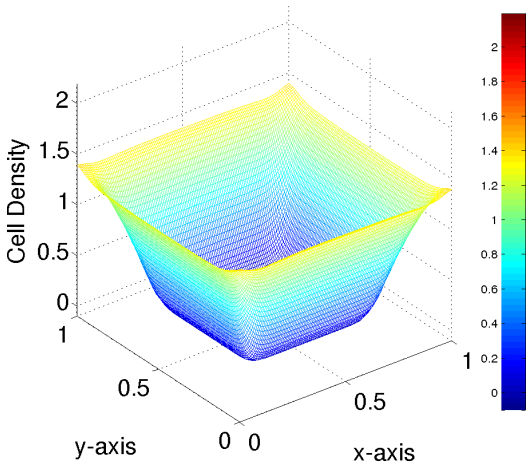

Figure 7.12 Cell density after 240 hours from a peripheral initial seeding with a constant death rate.

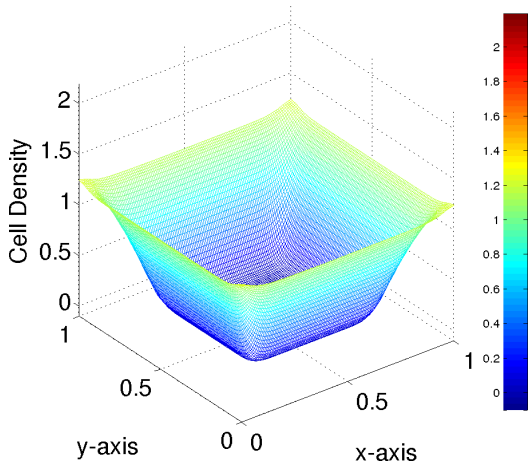

Figure 7.13 Cell density after 240 hours from a peripheral initial seeding with a variable death rate.

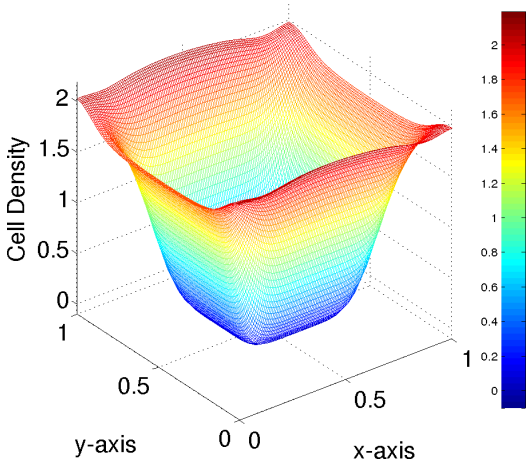

Figure 7.14 Cell density after 600 hours from a peripheral initial seeding with a constant death rate.

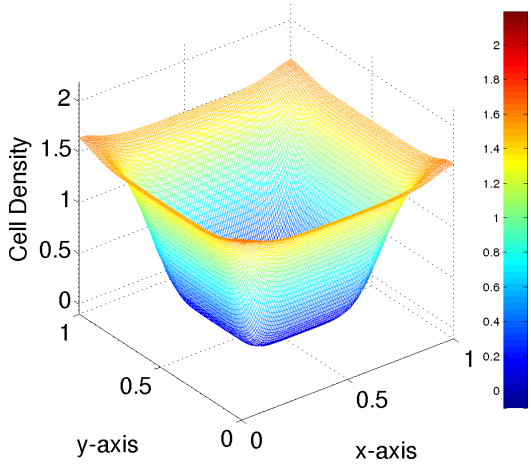

Figure 7.15 Cell density after 600 hours from a peripheral initial seeding with a variable death rate.

that the cell density, as expected, is lower in the variable death model than it is in

the constant death model. We also see, though, that the cell density in the variable death model is more uniform from $x = 0$ to $x = 1$ after 600 hours than it is in the constant death model. With a constant death rate, the cells proliferate faster in the region close to where nutrient is provided to the scaffold ($x = 0$) than further away from the inlet. The effect of damping the proliferation slightly in the variable death model has also brought about an effect of modulating the extreme values seen in the original model. Figure 7.16 shows the total cell population comparing the variable

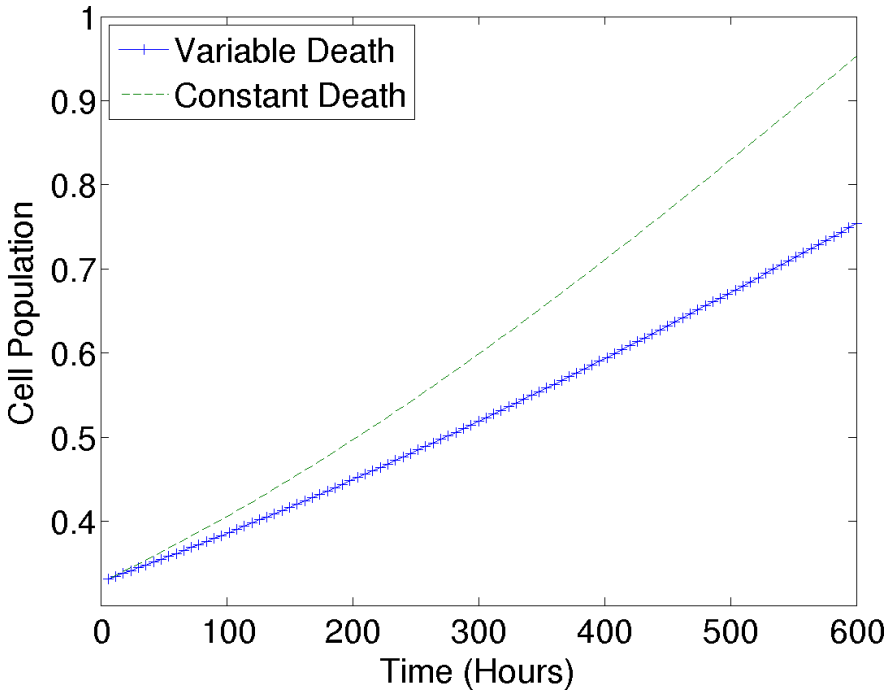

Figure 7.16 Total cell population comparing variable to constant death rates with peripheral initial seeding.

death model to the original model with constant death rate, confirming once more that the total population is always lower with variable death rate. We again see that as the simulation goes on, the total population with when varying the death rate is increasingly lower than when the death rate is held constant.

7.2.4 Discussion

In all three simulations, we saw that while the spatial forms of the results showed good agreement for both models, the total cell population was always significantly lower when variable death was considered. This effect was even stronger in the case of the central and peripheral seedings: in Figures 7.11 and 7.16 we saw that the difference in the rate at which both populations proliferated increased as time went on. The first simulation (Figure 7.6) in contrast saw the gap between the two populations growing at a relatively constant rate.

The reason for the difference in total population is due to the choice for the functional form of the variable death rate. It was chosen so that when the fluid flow was low the effective death rate was actually twice the prescribed death rate, while at high flow rates the "standard" death rate was attained. We showed in §4.4.1 that even increasing the death rate by a factor of 1.5 can have noticeably reductive effects on the cell density distribution. The model presented here should be regarded as a very preliminary investigation of one possible factor that may affect the death rate in a perfusion bioreactor; and the comparisons presented between the models should be taken only as a guide to illustrate the general effect of the model modification in different cases. It is of course possible that our choice of doubling the death rate at low flow rates is too drastic, or that the general functional dependence of death rate on flow speed is not appropriate. In Figure 7.1 we see that the decrease from an effective doubled death rate to the prescribed one is relatively slow. A possible future direction is to examine different functional dependence of the death rate on flow speed (not to mention, of course, examining the many other experimental factors that may lead to a non-constant death rate).

7.3 Variable Scaffold Permeability

Bioprinting growth factor onto the scaffold to direct and enhance cell proliferation, as considered in Chapter 5, is one means by which tissue engineers might better control experimental outcomes. If it is possible to initially seed the scaffold with minimal effort and still obtain a specific desired result, this would represent considerable progress for tissue engineering. Another direction we are exploring is motivated partially by results found by Raimondi *et al.* [43]. In that paper, the authors noted that a perfused flow produced significant increases in cell population when compared to a static culture system. That work, along with one of the model modifications proposed by Shakeel *et al.* [46] directed us to examine the effect of modeling a channel of higher permeability through the middle of the scaffold by which nutrient can be more efficiently delivered to cells on the interior. Tissue engineers use many different types of scaffolds, with different porosities and permeabilities in the unseeded states. If the permeability is too low, it may be difficult to provide nutrients to the interior cells, even under perfusion. We model a central high-permeability channel through our scaffold by modifying our original permeability function (equation (3.9)) to make it spatially nonuniform (with Gaussian profile) in the unseeded state:

$$k(c,x,y) = \left(1 + 15e^{\frac{-(y-0.5)^2}{0.05^2}}\right)\left(\frac{1}{1+c^2}\right), \tag{7.3}$$

and the behavior of the Gaussian component, $k(x,y)$, is shown in Figure 7.17. The numerical values of 15 and 0.05 in equation (7.3) are chosen to accentuate the effect of a narrow, highly-permeable channel for the purposes of modeling, but can easily be changed to better fit with possible experimental values. Using this new permeability we present sample results with a constant initial cell density to illustrate the effect of the central channel. This permeability is then used in simulations with the initial cell density varying in x and y (equation (7.2)) as well as the peripheral initial cell

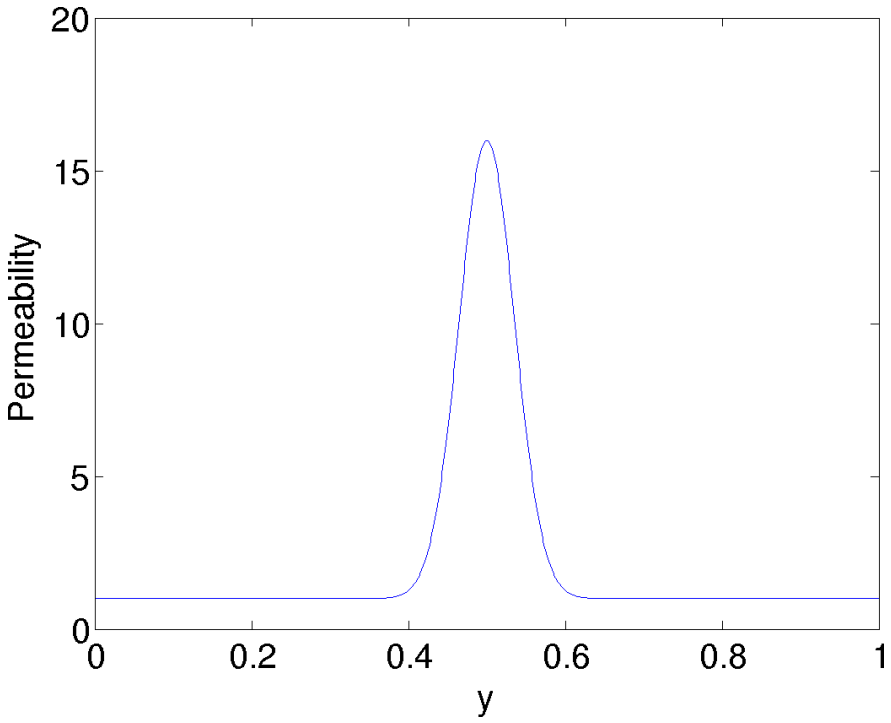

Figure 7.17 Graphical form of the Gaussian component of the variable permeability modification.

seeding. All other parameters and functional forms (including the original constant death rate) are as they were presented for the basic model in Chapter 4.

7.3.1 Constant Initial Cell Density

The assumed effect of creating a channel in the center of the scaffold is better nutrient delivery to the middle of the scaffold, which we expect to be accompanied by increased proliferation near the channel. The most effective way to see specifically what effect a central channel has on the evolution of the cell density is to examine the effects on a constant initial cell density. Figures 7.18 and 7.19 show the results of the simulation after 240 hours, and Figures 7.20 and 7.21 are after 600 hours. We can see that, as

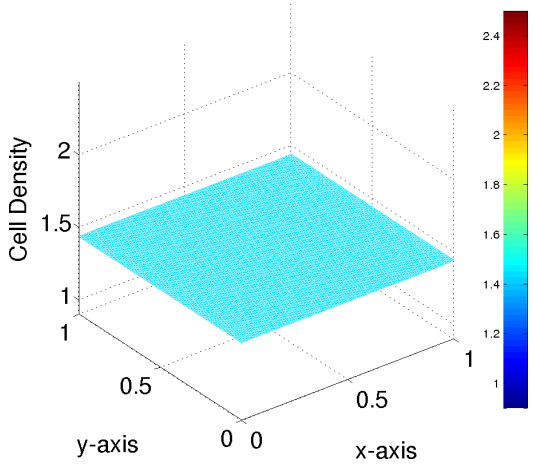

Figure 7.18 Cell density after 240 hours from a uniform initial seeding with the original permeability.

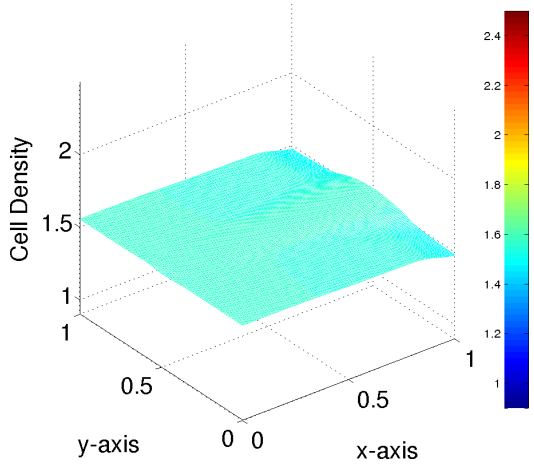

Figure 7.19 Cell density after 240 hours from a uniform initial seeding with a permeability channel.

expected, there is a slight up-tick in cell density density around the central channel, even as early as ten days. Another effect is that, while the cell density near the outlet ($x = 1$) shows a significant uptick at the channel location, this is at the expense of lower cell density elsewhere in this region. This may be explained by the fact that the nutrient uptake rate is fixed, while the flow in the highly permeable channel is much faster than in the rest of the scaffold. Therefore, at the fixed uptake rate, cells near the inlet do not have time to take up much nutrient before it has been carried downstream. Figure 7.22 shows the total cell population over the course of the simulation. The results which qualitatively were evident in the first figures

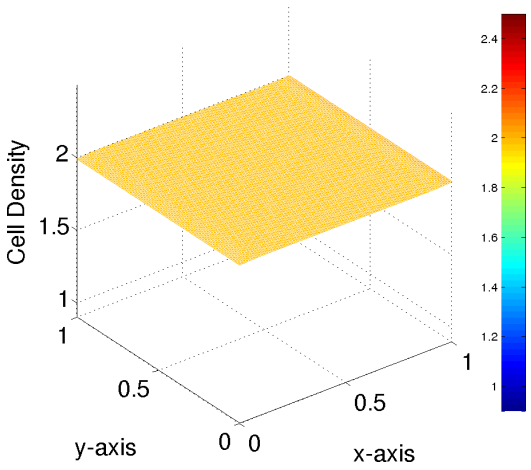

Figure 7.20 Cell density after 600 hours from a uniform initial seeding with the original permeability.

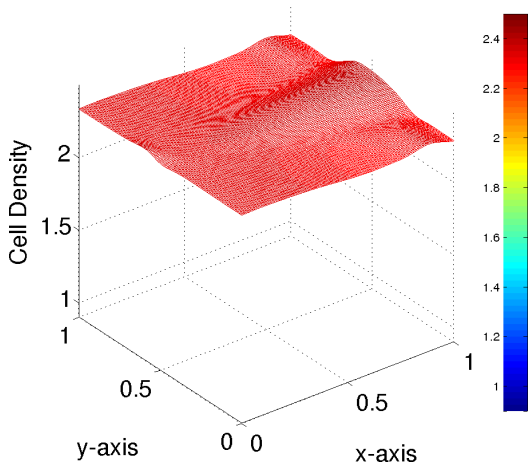

Figure 7.21 Cell density after 600 hours from a uniform initial seeding with a permeability channel.

are quantitatively confirmed as we see that with the central channel the total cell population is higher than when the permeability is left in its original form.

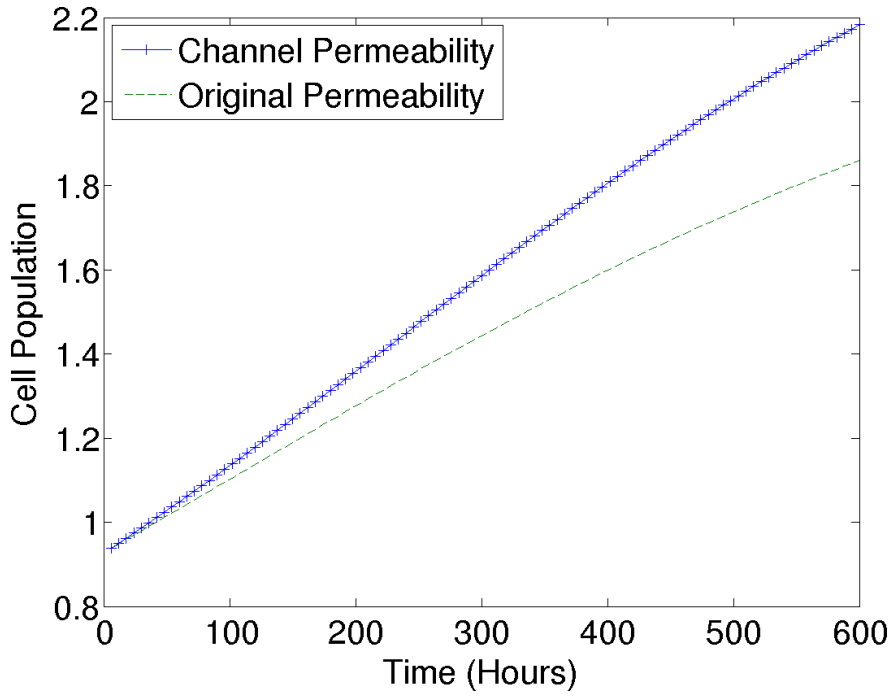

Figure 7.22 Total cell population comparing the original permeability to permeability with a central channel with a uniform initial cell seeding.

7.3.2 Initial Cell Density Varying in x and y

Now that we have seen the effect that a central permeability channel can have on cell density we introduce some more exotic initial cell seedings. The first one that we examine is the initial seeding varying in x and y which was used in the variable death model, among other simulations, and was first presented in equation (4.14). Based on the results of §7.3.1 we expect to see another up-tick in the cell density near the location of the central channel. Figures 7.23 and 7.24 show the results of the simulation after 240 hours, and Figures 7.25 and 7.26 are after 600 hours using the sinusoidal initial cell density. The figures show somewhat unexpected results.

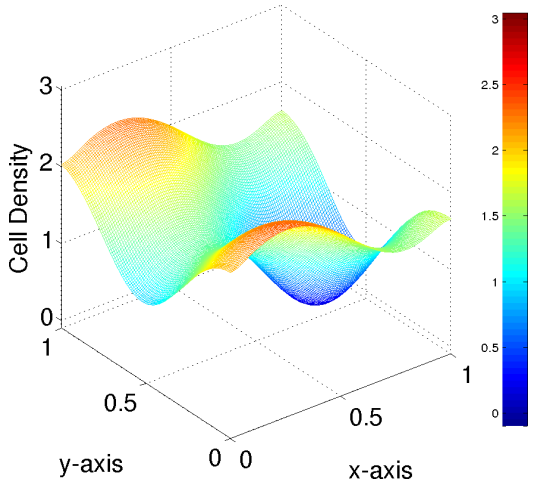

Figure 7.23 Cell density after 240 hours from a sinusoidal initial seeding from equation (4.14) with the original permeability.

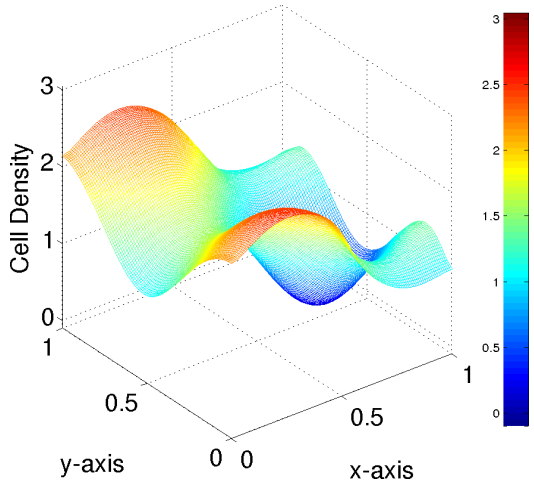

Figure 7.24 Cell density after 240 hours from a sinusoidal initial seeding from equation (4.14) with a permeability channel.

There is not a specific central channel-based up-tick in cell density, but instead we see an increase in the cell density near the inlet in general when compared with the regular permeability function. Not only is there an up-tick in the cell density near the inlet but this up-tick has come at the detriment of the cells near the outlet as the density there is lower than with the spatially-uniform scaffold. This result can be attributed to the initial seeding distribution, with its high density near the inlet at

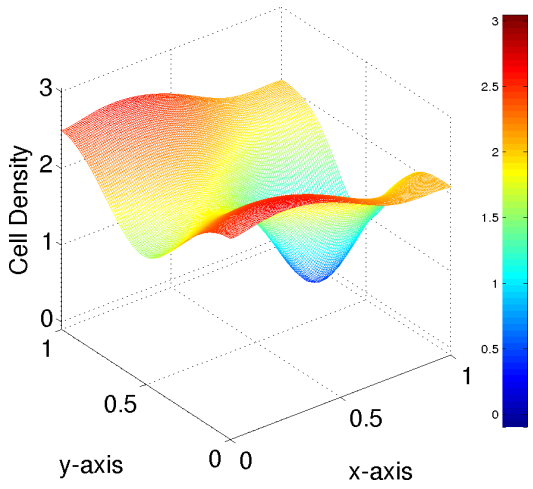

Figure 7.25 Cell density after 600 hours from a sinusoidal initial seeding from equation (4.14) with the original permeability.

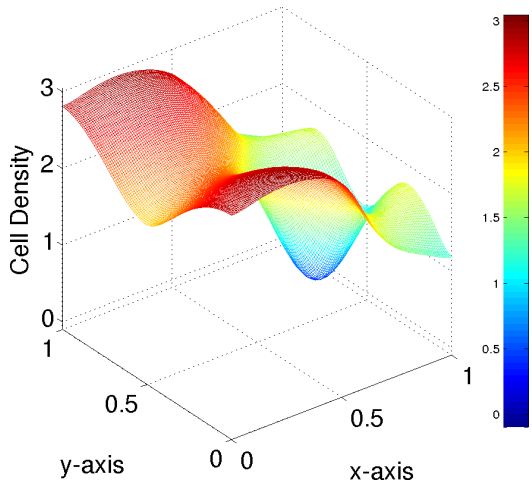

Figure 7.26 Cell density after 600 hours from a sinusoidal initial seeding from equation (4.14) with a permeability channel.

the beginning of the simulation. This offsets (to some extent) the high permeability of the unseeded scaffold, slowing the nutrient flow sufficiently to allow the cells to take up the nutrient and proliferate there. The fact that this effect appears to be more pronounced with the permeability channel suggests that, in the simulation with no channel, permeability is so low near the inlet that shear stresses are unfavorably high, suppressing this proliferation to some extent. Figure 7.27 shows that while there are large differences in the densities in specific regions of the scaffold, the total cell population does not vary as much as it did when considering a uniform initial cell density.

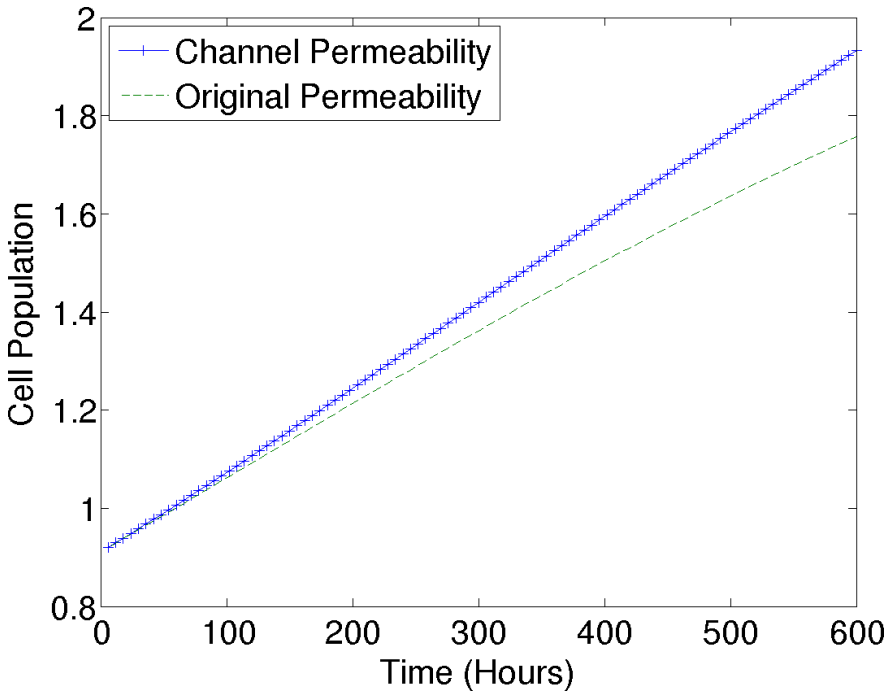

Figure 7.27 Total cell population comparing the original permeability to permeability with a central channel with a sinusoidal initial cell seeding from equation (4.14).

7.3.3 Initial Cell Density Around Periphery of Scaffold

The final set of sample results are those where the cells are initially seeded around the periphery of the scaffold, which we anticipate should be relatively easy to set up experimentally. Results for this simulation are difficult to anticipate because, unlike our earlier simulations, the majority of the region where the permeability channel exists has no cells initially in the vicinity. Figures 7.28 and 7.29 show the results of the simulation after 240 hours, and Figures 7.30 and 7.31 are after 600 hours with cells initially seeded on the periphery of the scaffold. The results from the figures, while not predicted, are easily explained. While the permeability around the channel and near the center of the scaffold is as high as is possible, the effect is difficult to detect, as there are no cells there to consume the extra nutrient available there. The cells which are near the channel, close to $x = 0$ and $x = 1$ are able to take advantage of

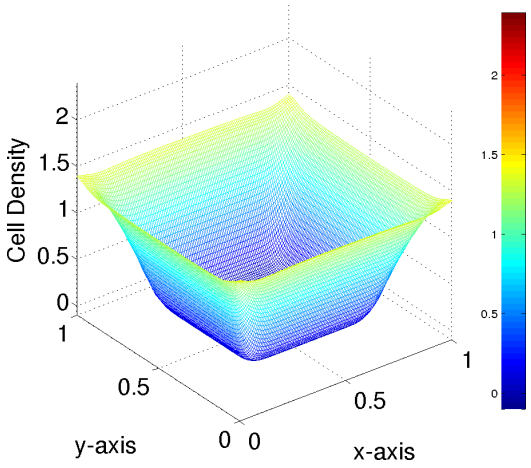

Figure 7.28 Cell density after 240 hours from a peripheral initial seeding with the original permeability.

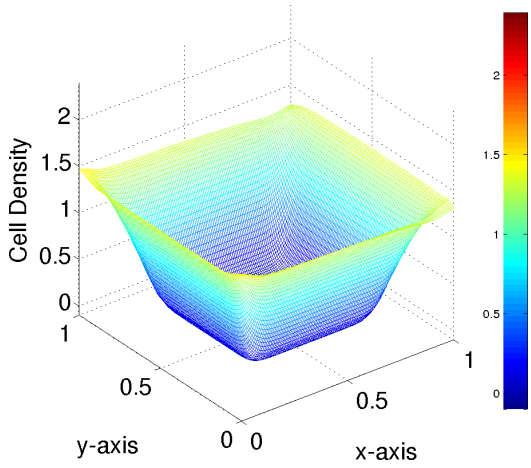

Figure 7.29 Cell density after 240 hours from a peripheral initial seeding with a permeability channel.

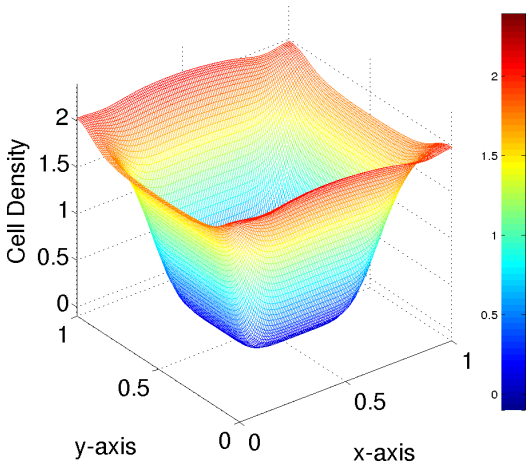

Figure 7.30 Cell density after 600 hours from a peripheral initial seeding with the original permeability.

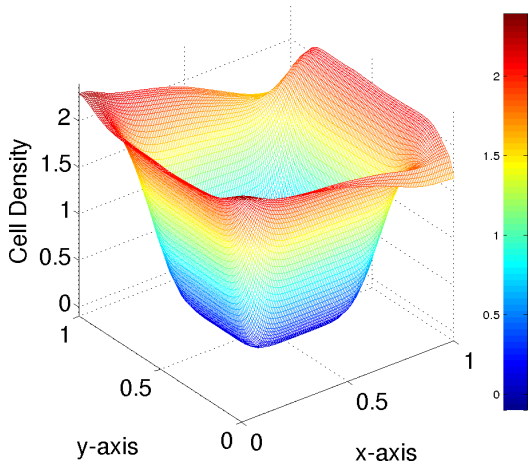

Figure 7.31 Cell density after 600 hours from a peripheral initial seeding with a permeability channel.

the extra nutrient and experienced higher proliferation, as is evident when comparing Figures 7.30 and 7.31. In these figures, the up-ticks noticed in the basic model near the inlet and outlet are accentuated in the channel permeability model as an increased nutrient concentration there means that less nutrient is available for cells near $y = 0$ and $y = 1$. Figure 7.32 shows that this final simulation provided the smallest

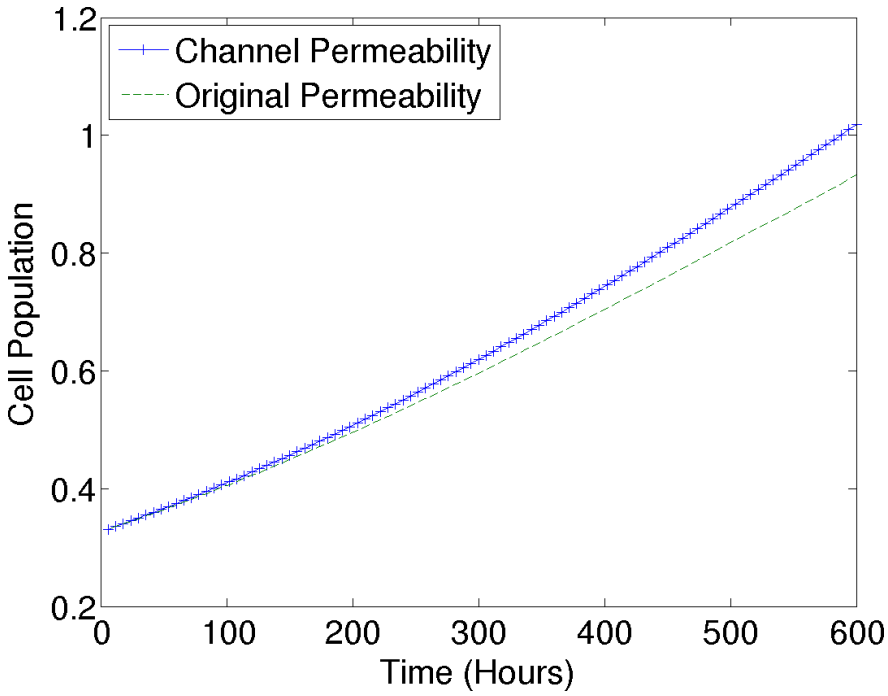

Figure 7.32 Total cell population comparing the original permeability to permeability with a central channel with a peripheral initial cell seeding.

change when comparing the total cell population between the two models. With the peripheral initial seeding the effect of a central permeability channel essentially functions as a means to obtain a different distribution of the cells towards the inlet and outlet.

7.3.4 Discussion

All three simulations presented with a central permeability channel provided very interesting results. We first were able to see that modeling a channel in the running near the center of the scaffold from inlet to outlet provided expected, predictable results when seeding with a uniform cell density. With this constant density we expected the cells to proliferate faster when more nutrient is available. Even this simple simulation, however, revealed two competing effects: on the one hand the nutrient flows preferentially down the high-permeability channel, leading generally

to increased proliferation here. But on the other hand, the high flow rates that are possible in the channel can also lead to nutrient being advected too rapidly for cells to take up, leading to the depressed cell density levels (compared with the standard model) observed near the inlet in Figures 7.19 and 7.21.

When seeding with the sinusoidal cell density in the second simulation, though, we saw that the local cell density plays a significant role. When there are already a relatively large number of cells near the inlet and the nutrient concentration here is somehow increased, a significant increase in proliferation is seen. It was very interesting to see that the inclusion of a central permeability channel has a similar effect to increasing the rate, θ, at which cells consume nutrient (see §4.4.4, Figures 4.67-4.74).

Finally, the results for the peripheral cell seeding, while perhaps not anticipated, are very reasonable with hindsight. The central channel only makes a significant difference in those regions where a cell population is present to consume the excess nutrient.

We note that the simple permeability form proposed in equation (7.3) is easily generalized to model any chosen variable permeability of the underlying scaffold. Therefore, an obvious direction in which to generalize this work is to examine how scaffolds with prescribed permeabilities might be used to influence the final experimental outcome (perhaps even in conjunction with printed growth-factor patterns). Focusing on relatively controllable aspects such as scaffold porosity and permeability, and scaffold surface modifications, appear to offer the best hope for control of experimental outcomes.

CHAPTER 8

CONCLUSIONS AND FUTURE WORK

In this dissertation we have developed a comprehensive and very versatile model to describe a tissue engineering experiment in a perfusion based bioreactor. We used experimental data to simulate growth of chondrocytes when fed by oxygen, which becomes toxic in large amounts.

In Chapter 4 we simulated the experiment starting with a uniform cell seeding, since this is the end result experimentalists wish to attain in many circumstances. We next considered spatially inhomogeneous initial cell seedings, to investigate the effect on the end result. We found that in the basic model the resulting cell density tended to keep the form with which it was seeded initially. The robustness of the basic model was thoroughly demonstrated (via small changes in the form of constituent functions) in §4.3 as was its versatility (the ease with which we were able to model different scenarios) in §4.4.

In Chapter 5 we showed how a small adjustment to the cell density equation (equation (3.4)) in the form of two extra terms (a haptotactic cell flux, and an additional proliferation source term), and the inclusion of one extra governing equation (for growth factor) were able to model the concept of bioprinting growth factor onto the scaffold to direct cell motility. We compared simulated results with experiments run by Miller *et al.* [28] and were able to obtain good qualitative agreement indicating the model was able to capture the effect of growth factor bound to the scaffold. We were also able to reconcile our model, in which haptotaxis plays a role, with the assertion of Miller *et al.* [28] that haptotaxis is negligible (small growth factor gradients almost everywhere in the experimental scenario make the haptotaxis hard to detect; but it can be significant under different experimental conditions).

Multiple growth factor bioprinting patterns were then simulated with varying initial cell density seedings to investigate the hypothesis of directing cell motility and proliferation to obtain a given final cell density. One goal of such investigations is to explore ways to obtain a uniform final cell density from an initial peripheral cell density, as seeding around the periphery is presumably easier experimentally than a uniform seeding.

In Chapter 6 we were able to use the same basic model to analyze the effect of cyclically compressing the scaffold via a multiple scale analysis. We simulated the effect of compression on the time scale of fluid flow, and then averaged the model over an arbitrary loading cycle to derive a model valid over the timescale of cell proliferation. The model considered here does not take account of any additional biology or physiology that the loading may stimulate. Since cyclic loading is known to stimulate several additional biological cellular responses [4, 44], one function of our model is to investigate how important such neglected effects might be. Since our results indicate only modest differences between loaded and unloaded cases (while some experimental data point to significant differences), we conclude that extra biology should be included in a more realistic model of such loading.

Finally, Chapter 7 includes results from two hypothetical situations that have yet to receive much consideration in models or experiments. The cell death rate is typically considered to be a constant value because it is difficult to determine death rates at the cellular level. We were able to successfully implement the effect of a cell death rate which depends on the local fluid flow rate which is a decreasing function of fluid velocity and while the included simulations incorporated an effective death rate which was likely too high at low flow speed, the model sufficiently captured the effects so that with data-driven adjustments in future, the concept of a variable death rate can be further studied. We next considered a modification intended to deliver nutrient more effectively to the center of the scaffold: a high-permeability

channel through the middle of the scaffold. This was modeled as a prescribed spatial variation in the unseeded scaffold permeability. This approach is similar in spirit to the bioprinting of growth factor: both techniques aim to modify the underlying scaffold in order to achieve a desired experimental outcome.

Possible future directions for the model are abundant. The ease with which we were able to include the effect of haptotaxis, a variable death rate, and a central channel lead us to believe that the model can be adapted to many other possible experimental protocols that have not yet been considered. Further simulation can be done to determine a more effective averaged variable death rate, simulation of more than one central channel or more complicated scaffold permeabilities, different initial cell seeding densities, and many other aspects. The cyclic compression model of Chapter 6 did not take into account any cell level biology, such as up-regulation of chondrogenic genetic markers, hence there is much more work to be done here also. As tissue engineering continues to develop, it is our hope that this model is a stepping stone to a more complete description of a full experiment, and that it (or future, improved, iterations of the model) can help quickly determine optimal and detrimental parameter values and experimental protocols to aid in better production of viable replacement tissue.

BIBLIOGRAPHY

[1] D.J. Acheson. *Elementary Fluid Dynamics*. Oxford University Press, New York, 1990.

[2] O.M. Babalola and L.J. Bonassar. Parametric finite element analysis of physical stimuli resulting from mechanical stimulation of tissue engineered cartilage. *Journal of Biomechanical Engineering*, 131(6), 2009.

[3] E. Bueno, G. Laevsky, and G. Barabino. Enhancing cell seeding of scaffolds in tissue engineering through manipulation of hydrodynamic parameters. *Journal of Biotechnology*, 129:516–531, 2007.

[4] M.D. Buschmann, Y.A. Gluzband, A.J. Grodzinsky, and E.B. Hunziker. Mechanical compression modulates matrix biosynthesis in chondrocyte/agarose culture. *Journal of Cell Science*, 108(4):1497–1508, 1995.

[5] F. Bussolino, M. DiRenzo, M. Ziche, E. Bocchietto, L. Olivero, M. Naldini, G. Gaudino, L. Tamagnone, A. Coffer, and P. Comoglio. Hepatocyte growth factor is a potent angiogenic factor which stimulates endothelial cell motility and growth. *Journal of Cell Biology*, 119(3):629–641, 1992.

[6] P. Campbell, E. Miller, G. Fisher, L. Walker, and L. Weiss. Engineered spatial patterns of fgf-2 immobilized on fibrin direct cell organization. *Biomaterials*, 26(33):6762–6770, 2005.

[7] C.J. Catt, W. Schuurman, B.G. Sengers, P.R. van Weeren, W.J.A. Dhert, C.P. Please, and J. Malda. Mathematical modelling of tissue formation in chondrocyte filter cultures. *European Cells and Materials*, 22:377–392, 2011.

[8] C. Chung, C. Chen, C. Chen, and C. Tseng. Enhancement of cell growth in tissue-engineering constructs under direct perfusion: Modeling and simulation. *Biotechnology and Bioengineering*, 97:1603–1616, 2007.

[9] C. Chung, C. Chen, T. Lin, and C. Tseng. A compact computational model for cell construct development in perfusion culture. *Biotechnology and Bioengineering*, 99:1535–1541, 2008.

[10] F. Coletti, S. Macchietto, and N. Elvassore. Mathematical modeling of three-dimensional cell cultures in perfusion bioreactors. *Industrial and Engineering Chemistry Research*, 45:8158–8169, 2006.

[11] D. Contois. Kinetics of bacterial growth: Relationship between population density and specific growth rate of continuous cultures. *Journal of General Microbiology*, 21:40–50, 1959.

[12] G. Cooper, E. Miller, G. Decesare, A. Usas, E. Lensie, M. Bykowski, J. Huard, L. Weiss, J. Losee, and P. Campbell. Inkjet-based biopatterning of bone morphogenetic protein-2 to spatially control calvarial bone formation. *Tissue Engineering - Part A*, 16(5):1749–1759, 2010.

[13] A. Curtis and M. Riehle. Tissue engineering: The biophysical background. *Physics in Medicine and Biology*, 46:47–65, 2001.

[14] A. Fick. Ueber diffusion. *Annalen der Physik*, 170:59–86, 1855.

[15] H. Fountain. A first: Organs tailor-made with bodys own cells. *http://www.nytimes.com/2012/09/16/health/research/scientists-make-progress-in-tailor-made-organs.html*, September 2012.

[16] H. Fountain. Human muscle, regrown on animal scaffolding. *http://www.nytimes.com/2012/09/17/health/research/human-muscle-regenerated-with-animal-help.html*, September 2012.

[17] H. Fountain. One day, growing spare parts inside the body. *http://www.nytimes.com/2012/09/18/health/research/using-the-body-to-incubate-replacement-organs.html*, September 2012.

[18] A. Friedman, B. Aguda, M. Chaplain, M. Kimmel, H. Levine, G. Lolas, A. Matzavinos, M. Nilsen-Hamilton, and A. Swierniak. *Tutorials in Mathematical Biosciences III: Cell Cycle, Proliferation, and Cancer (Lecture Notes in Mathematics / Mathematical Biosciences Subseries)*. Springer, 2010.

[19] C. Galban and B. Locke. Analysis of cell growth kinetics and substrate diffusion in a polymer scaffold. *Biotechnology and Bioengineering*, 65(2):121–132, 1999.

[20] S. Kapur, D. Baylink, and K.-H. Lau. Fluid flow shear stress stimulates human osteoblast proliferation and differentiation through multiple interacting and competing signal transduction pathways. *Bone*, 32(3):241–251, 2003.

[21] E. Ker, A. Nain, L. Weiss, J. Wang, J. Suhan, C. Amon, and P. Campbell. Bioprinting of growth factors onto aligned sub-micron fibrous scaffolds for simultaneous control of cell differentiation and alignment. *Biomaterials*, 32(32):8097–8107, 2011.

[22] M. Lappa. Organic tissues in rotating bioreactors: Fluid-mechanical aspects, dynamic growth models, and morphological evolution. *Biotechnology and Bioengineering*, 84(5):518–532, 2003.

[23] M. Lewis, B. MacArthur, J. Malda, G. Pettet, and C. Please. Heterogeneous proliferation within engineered cartilaginous tissue: the role of oxygen tension. *Biotechnology and Bioengineering*, 91:607–615, 2005.

[24] M. Lutianov, N. Shialesh, S. Roberts, and J-H. Kuiper. A mathematical model of cartilage regeneration after cell therapy. *Journal of Theoretical Biology*, 289:136–150, 2011.

[25] P. Maini. Spatial and spatio-temporal patterns in a cell-haptotaxis model. *Journal of Mathematical Biology*, 27(5):507–522, 1989.

[26] J. Malda, J. Rouwkema, D. Martens, E. Le Comte, F. Kooy, J. Tramper, C. van Blitterswijk, and J. Riesle. Oxygen gradients in tissue-engineered pegt/pbt cartilaginous constructs: Measurement and modelling. *Biotechnology and Bioengineering*, 86(1):9–18, 2004.

[27] R.L. Mauck, M.A. Soltz, C.C.B. Wang, D.D. Wong, P.-H.G. Chao, W.B. Valhmu, C.T. Hung, and G.A. Ateshian. Functional tissue engineering of articular cartilage through dynamic loading of chondrocyte seeded agarose gels. *Journal of Biomechanical Engineering*, 122(3):252–260, 2000.

[28] E. Miller, G. Fisher, L. Weiss, L. Walker, and P. Campbell. Dose-dependent cell growth in response to concentration modulated patterns of fgf-2 printed on fibrin. *Biomaterials*, 27(10):2213–2221, 2006.

[29] E. Miller, K. Li, T. Kanade, L. Weiss, L. Walker, and P. Campbell. Spatially directed guidance of stem cell population migration by immobilized patterns of growth factors. *Biomaterials*, 32(11):2775–2785, 2011.

[30] E.K. Moo, W. Herzog, S.K. Han, N.A. Abu Osman, B. Pingguan-Murphy, and S. Federico. Mechanical behaviour of in-situ chondrocytes subjected to different loading rates: a finite element study. *Biomechanics and Modeling in Mechanobiology*, in press:1–11, 2012.

[31] J.D. Murray. *Mathematical Biology*. Springer-Verlag, New York, 1989.

[32] B. Obradovic, J.H. Meldon, L.E. Freed, and G. Vunjak-Novakovic. Glycosaminoglycan deposition in engineered cartilage: Experiments and mathematical model. *AIChE Journal*, 46:1860–1871, 2000.

[33] F. O'Brien, B. Harley, M. Waller, I. Yannas, L. Gibson, and P. Prendergast. The effect of pore size on permeability and cell attachment in collagen scaffolds for tissue engineering. *Technology and Health Care*, 15(1):3–17, 2007.

[34] R. O'Dea, S. Waters, and H. Byrne. A two-fluid model for tissue growth within a dynamic flow environment. *European Journal of Applied Mathematics*, 19(6):607–634, 2008.

[35] R. O'Dea, S. Waters, and H. Byrne. A multiphase model for tissue construct growth in a perfusion bioreactor. *Mathematical Medicine and Biology*, 27(2):95–127, 2009.

[36] M. Orme and M. Chaplain. A mathematical model of the first steps of tumour-related angiogenesis: Capillary sprout formation and secondary branching. *Mathematical Medicine and Biology*, 13(2):73–98, 1996.

[37] J. Osborne, R. O'Dea, J. Whiteley, H. Byrne, and S. Waters. The influence of bioreactor geometry and the mechanical environment on engineered tissues. *Journal of Biomechanical Engineering*, 132(5), 2010.

[38] G. Oster, J. Murray, and A. Harris. Mechanical aspects of mesenchymal morphogenesis. *Journal of Embryology and Experimental Morphology*, 78:83–125, 1983.

[39] A. Perelson, P. Maini, and J. Murray. Nonlinear pattern selection in a mechanical model for morphogenesis. *Journal of Mathematical Biology*, 24(5):525–541, 1986.

[40] J. Pohlmeyer, S. Waters, and L. Cummings. Mathematical model of a growth factor driven haptotaxis and proliferation in a tissue engineering scaffold. *Bulletin of Mathematical Biology, In Preparation*, 2012.

[41] B. Porter, R. Zauel, H. Stockman, R. Guldberg, and D. Fyhrie. 3-D computational modelling of media flow through scaffolds in a perfusion bioreactor. *Journal of Biomechanical Engineering*, 38(3):543–549, 2005.

[42] R. Probstein. *Physicochemical Hydrodynamics, An Introduction (Second Edition).* John Wiley & Sons, New York, 1994.

[43] M. Raimondi, F. Boschetti, L. Falcone, F. Migliavacca, A. Remuzzi, and G. Dubini. The effect of media perfusion on three-dimensional cultures of human chondrocytes: Integration of experimental and computational approaches. *Biorheology*, 41(3):401–410, 2004.

[44] O. Schätti, S. Grad, J. Goldhahn, G. Salzmann, Z. Li, M. Alini, and M.J. Stoddart. A combination of shear and dynamic compression leads to mechanically induced chondrogenesis of human mesenchymal stem cells. *European Cells and Materials*, 22:214–225, 2011.

[45] B. Sengers, M. Taylor, C. Please, and R. Oreffo. Computational modelling of cell spreading and tissue regeneration in porous scaffolds. *Biomaterials*, 28:1926–1940, 2007.

[46] M. Shakeel, P. Matthews, S. Waters, and R. Graham. A continuum model of cell proliferation and nutrient transport in a perfusion bioreactor. *To appear in: Mathematics in Medicine and Biology*, 2012.

[47] Y. Tao. Global existence for a haptotaxis model of cancer invasion with tissue remodeling. *Nonlinear Analysis: Real World Applications*, 12(1):418–435, 2011.

[48] A. Yeatts and J. Fisher. Bone tissue engineering bioreactors: Dynamic culture and the influence of shear stress. *Bone*, 48(2):171–181, 2011.

[49] M. Zelzer, D. Albutt, M. Alexander, and N. Russell. The role of albumin and fibronectin in the adhesion of fibroblasts to plasma polymer surfaces. *Plasma Processes and Polymers*, 9(2):149–156, 2012.